2011

Characterization of photon counting CZT detectors for medical x-ray imaging and spectroscopy

Shannon Fritz
Louisiana State University and Agricultural and Mechanical College, shannon.fritz@gmail.com

Recommended Citation

Fritz, Shannon, "Characterization of photon counting CZT detectors for medical x-ray imaging and spectroscopy" (2011). *LSU Doctoral Dissertations*. 3005.
https://digitalcommons.lsu.edu/gradschool_dissertations/3005

CHARACTERIZATION OF PHOTON COUNTING CZT DETECTORS FOR MEDICAL X-RAY IMAGING AND SPECTROSCOPY

A Dissertation

Submitted to the Graduate Faculty of the
Louisiana State University and
Agricultural and Mechanical College
in partial fulfillment of the
requirements for the degree of
Doctor of Philosophy

in

The Department of Physics and Astronomy

by

Shannon Fritz
B.A., Texas Lutheran University, 2001
M.S., Texas State University – San Marcos, 2003
M.S., University of Nebraska – Lincoln, 2006
May 2011

This work is dedicated to Mark, my true favorite.

ACKNOWLEDGEMENTS

First I thank my advisor Dr. Polad Shikhaliev. I am grateful for his understanding as I tried to juggle classes with research. It has been such a pleasure to work with someone so enthusiastic and knowledgeable in the field. I thank Louisiana State University College of Basic Sciences for funding this project through start up funds. I also thank the LSU Graduate School for the generous Enhancement Award that I received during my studies.

I also thank my committee members Dr. Jeff Blackmon, Dr. Kip Matthews, and Dr. Kenneth Hogstrom. Dr. Matthews is always available for questions and feedback, and I appreciate not only all his time and effort, but the genuine care he has for the well-being of the students. I particularly thank Dr. Hogstrom for his help in my transition to the PhD program.

I thank the other professors in the medical physics program for their obvious desire to see the students succeed, particularly Dr. Gibbons and Dr. Wang for their support. I must also thank the medical physics secretary, Ms. Yvonne Thomas, not only for all her help with every form, fax, and phone call, but also the warmth and kind words offered daily…not to mention all the chocolate.

Thank you to all the wonderful friends I've made in Baton Rouge, particularly my friends in the medical physics program. I would like to give special thanks to my former officemate Peter Petrek for keeping me sane and to Catie Talbert-Haveman for keeping me smiling. Your support has been tremendous; my family away from home.

I also thank my amazing family. Thank you Naw-Nee and Auntie for being beside me every step of the way, even though you would rather I had stayed in Texas. Thanks to my sisters for encouraging me and keeping me filled in on everything going on at home. You made the homesickness easier to take. Thanks mostly to my incredible parents. I know it's supposed to be the other way around, but I am so proud of both of you.

Finally, many, many thanks to my wonderful husband, Mark. Thank you for following me from the flatlands to the swamplands. Someday we'll make it to those mountains.

TABLE OF CONTENTS

ACKNOWLEDGEMENTS .... **iii**

LIST OF TABLES .... **vi**

LIST OF FIGURES .... **vii**

ABSTRACT .... **xiv**

1 INTRODUCTION **1**
- 1.1 PRINCIPLES OF MEDICAL X-RAY IMAGING 2
  - 1.1.1 X-rays 2
  - 1.1.2 Role of Energy in X-ray Imaging 5
  - 1.1.3 Image Quality 6
- 1.2 DETECTORS FOR X-RAY IMAGING 8
  - 1.2.1 Indirect Detection 9
  - 1.2.2 Direct Detection 10
- 1.3 APPLICATIONS FOR PHOTON COUNTING, ENERGY-RESOLVING DETECTORS 11
  - 1.3.1 Breast CT 11
  - 1.3.2 Dual Energy Subtraction 12
  - 1.3.3 X-ray Spectroscopy 13
- 1.4 MOTIVATION TO CHARACTERIZE CZT DETECTORS 13

2 EFFECT OF IRRADIATION GEOMETRY ON ENERGY RESOLUTION **14**
- 2.1 SIGNAL GENERATION 16
- 2.2 HOLE TRAPPING 17
  - 2.2.1 Hecht Formalism 18
- 2.3 INVESTIGATIONS TO REDUCE SPECTRAL TAILING 19
  - 2.3.1 Simulating CZT Detector Response 20
  - 2.3.2 Measuring CZT Detector Response 23
  - 2.3.3 Results of Simulations and Measurements 25
- 2.4 CONCLUSIONS AND CONSIDERATIONS FOR TILTED ANGLE GEOMETRY 28
  - 2.4.1 Reduced Charged Diffusion in a Thin Detector 30
  - 2.4.2 Count Rate in Tilted Angle Geometry 31
  - 2.4.3 Increased Characteristic X-ray Escape 31

3 INVESTIGATION OF CHARACTERISTIC X-RAY ESCAPE **33**
- 3.1 CHARGE SHARING IN CZT AND OTHER MATERIALS 33
- 3.2 SIMULATING ENERGY ESCAPE FROM A CZT DETECTOR PIXEL 34
  - 3.2.1 X-ray Interaction in CZT Detectors 35
  - 3.2.2 Simulation Study 39
  - 3.2.3 Experimental Study 46
- 3.3 RESULTS OF SIMULATIONS 46

3.3.1 Depth Attenuation Profiles for Normal and Tilted Angle 46
3.3.2 Back and Side Escape Fractions 47
3.3.3 Building X-ray Spectra Considering Escape 49
3.3.4 X-ray Spectra with Full Absorption Only 50
3.3.5 Final X-ray Spectrum 51
3.3.6 2-D Mapping of K x-ray Reabsorption 52
3.3.7 Spatial Resolution 53
3.3.8 Experimental Results with Square Pixel Compared to Simulation 54
3.4 CONCLUSIONS AND ADVANTAGES OF TILTED ANGLE IRRADIATION OF STRIP PIXELS 55

4 IMAGING CZT DETECTOR 56
4.1 DESCRIPTION OF THE NEXIS DETECTOR 56
4.2 IMPORTANCE OF ENERGY RESOLUTION 57
4.3 ISOTOPE MEASUREMENTS WITH THE NEXIS DETECTOR 60
4.4 IMAGING EXPERIMENTS WITH NEXIS DETECTOR 61
4.5 CONCLUSIONS AND MODIFICATION OF IMAGING CZT DETECTOR 63

5 X-RAY SPECTROSCOPY WITH A CZT DETECTOR 65
5.1 EVALUATING A CZT DETECTOR FOR X-RAY SPECTROSCOPY 66
5.1.1 Modifying Interaction Depth and Electric Field 66
5.1.2 Measurements with Planar and Capacitive Grid Detectors 67
5.1.3 Correcting for K x-ray Escape 70
5.1.4 Evaluating Corrected Spectra 73
5.2 RESULTS OF MEASUREMENTS AND CORRECTIONS 74
5.3 CONCLUSIONS AND ADVANTAGES OF TILTED ANGLE IRRADIATION WITH A CAPACITIVE GRID DETECTOR 78

LITERATURE CITED……………………………………………………………...80

APPENDIX A SIMULATING CZT DETECTOR USING THE HECHT FORMALISM 84

APPENDIX B MONTE CARLO SIMULATIONS OF K X-RAY ESCAPE FRACTIONS 89

APPENDIX C K BACK ESCAPE FRACTIONS AND CORRECTION OF X-RAY SPECTRUM 95

VITA 101

LIST OF TABLES

TABLE 2.1 PROPERTIES OF EV PRODUCTS CZT 16

TABLE 2.2 PEAK-TOTAL RATIOS (%): SIMULATIONS 30

TABLE 2.3 PEAK-TO-TOTAL RATIOS (%): EXPERIMENT VS THEORY 30

TABLE 3.1 CHARACTERISTIC X-RAY ESCAPE FRACTIONS FOR SQUARE PIXELS 48

TABLE 3.2 CHARACTERISTIC X-RAY ESCAPE FRACTIONS FOR STRIP PIXELS, 90^o IRRADIATION 48

TABLE 3.3 CHARACTERISTIC X-RAY ESCAPE FRACTIONS FOR STRIP PIXELS, 10^o TILTED ANGLE 49

TABLE 5.1 PROPERTIES OF DETECTORS FOR X-RAY SPECTROSCOPY 65

TABLE 5.2 PEAK-TO-TOTAL RATIOS FOR ISOTOPE MEASUREMENTS (%) 75

TABLE 5.3 INTEGRAL DEVIATION OF X-RAY SPECTRA (%) 79

LIST OF FIGURES

Figure 1.1 Electromagnetic spectrum; x-rays used for diagnostic purposes typically fall between 20 and 140 keV.. 3

Figure 1.2 Typical x-ray spectrum for a 120 kVp beam with tungsten target, filtered with 10 cm acrylic. The sharp peaks are a result of characteristic x-rays from tungsten at 59 and 67 keV.. 3

Figure 1.3 Schematic of the basic principles of an x-ray imaging system. X-rays incident on an object composed of different materials (heterogeneous) will interact differently based on the attenuation coefficient, μ, of the material. The resulting image is essentially the shadow cast by the object being illuminated by x-rays.. 4

Figure 1.4 Attenuation of photons with respect to energy for fat and glandular breast tissue and for breast tumors. Values for μ are taken from [9]................... 5

Figure 1.5 Relationship between 15-year survival rates and tumor size. Curve was generating using the equation SF = [exp(-QD)]^{z}, where SF is surviving fraction, D is tumor size, and Q and z are constants [11, 12]. 6

Figure 1.6 Charge-integrating detectors record total charge for all interactions. Signal is received by the digitization electronics and the sum of all charge is recorded. Photon counting detectors resolve individual interactions and allow for energy-resolving capability... 9

Figure 1.7 Schematic of indirect detection with a scintillation detector. The incoming photon interacts in the scintillation material to produce light. The light photons are then incident on the photodetector and electric charge is created.. 10

Figure 1.8 Schematic of semiconductor detector which uses direct detection. An electric field is applied to the semiconductor material. The incoming photon generates charge in the form of electron-hole pairs (e-h) and signal is generated as the charge moves to the electrodes.. 10

Figure 1.9 (a) Schematic of detected breast CT system with patient lying prone on a table that houses the x-ray source and detector. (b) Schematic of the imaging system from above. The source and detector are rotated in tandem around the breast. 12

Figure 2.1 Example of ideal spectrum (dashed line) and spectrum with low energy tailing (solid line) for a monoenergetic 120 keV source... 14

FIGURE 2.2 SCHEMATIC OF SCANNING SLIT IMAGE ACQUISITION. DETECTOR MAY BE POSITIONED IN EITHER EDGE-ON OR TILTED ANGLE GEOMETRY AND MOVED ALONG THE SCANNING AXIS IN SMALL INCREMENTS. THE STEP SIZE OF THE DETECTOR DETERMINES THE SPATIAL RESOLUTION IN THAT DIRECTION. 15

FIGURE 2.3 SCHEMATIC OF SIGNAL GENERATION IN A PLANAR CZT DETECTOR FOR RADIATION INCIDENT AT AN ANGLE A BETWEEN THE BEAM AND DETECTOR SURFACE. 16

FIGURE 2.4 (A) SIGNAL AMPLITUDE WITH RESPECT TO DEPTH OF INTERACTION FOR AN IDEAL DETECTOR AND (B) A DETECTOR WITH HOLE TRAPPING. 19

FIGURE 2.5 THREE IRRADIATION GEOMETRIES USED FOR TAILING EXPERIMENTS. THE LINES TO THE RIGHT OF EACH FIGURE ILLUSTRATE THE EXPECTED DISTRIBUTION OF INTERACTION DEPTHS FOR EACH GEOMETRY 20

FIGURE 2.6 CZT DETECTOR SETUP; (A) PHOTO OF CZT CRYSTAL IN BRASS CASING CONNECTED TO PREAMPLIFIER AND (B) SCHEMATIC OF CZT CRYSTAL WITH ELECTRODES AND BRASS ENCASEMENT. 23

FIGURE 2.7 (A) SCHEMATIC OF EDGE-SCAN SETUP. THE EDGE-SCAN METHOD MEASURES THE DEPENDENCE OF SIGNAL AMPLITUDE ON INTERACTION DEPTH. (B) SCHEMATIC OF SETUP USED TO TEST ELECTRIC FIELD AT DETECTOR EDGE. 24

FIGURE 2.8 (A) ENERGY SPECTRUM RESULTS OF EDGE SCANNING WITH 0.3 MM STEPS OF THE 122 KEV RADIATION BEAM WITH 0.3 MM THICKNESS AND (B) RESULTS OF SIMULATIONS WITH MATCHED PARAMETERS. 25

FIGURE 2.9 (A) SIGNAL INTENSITY PROFILE OF EDGE-SCAN WITH 122 KEV BEAM OF 0.3 MM COLLIMATION. (B) PEAK ENERGY WITH RESPECT TO BEAM POSITION ALONG WITH HECHT CURVE FIT ASSUMING ELECTRON AND HOLE MEAN FREE PATH LENGTHS OF 25 MM AND 0.33 MM, RESPECTIVELY. 26

FIGURE 2.10 RESULTS OF EDGE TEST EXPERIMENT. TWO CZTS ARE STACKED (SEE FIGURE 2.7) TO INVESTIGATE WHETHER DEAD REGIONS EXIST ALONG THE EDGE OF THE CZT CRYSTAL. 27

FIGURE 2.11 (A) EXPERIMENTAL AND THEORETICAL ENERGY SPECTRA WITH EDGE-ON IRRADIATION OF 122 KEV BEAM WITH 3 MM THICKNESS. (B) SIMULATED ENERGY SPECTRA WITH 122 KEV BEAMS FOR THICKNESSES OF 0.375 – 3 MM INCIDENT ON THE EDGE OF THE CZT; BROADENING DUE TO STATISTICAL FLUCTUATIONS OF THE CHARGE CARRIERS WAS INCORPORATED. 27

FIGURE 2.12 SIMULATED ENERGY SPECTRA OF 20-120 KEV ENERGIES FOR (A) SURFACE-ON AND TILTED ANGLE INCIDENCE WITH (B) 15° AND(C) 10° TILT ANGLES. THE TOTAL NUMBER OF THE PHOTONS WAS KEPT CONSTANT IN EACH CASE. 28

FIGURE 2.13 ENERGY SPECTRA OF THE 59 KEV (LEFT) AND 122 KEV (RIGHT) RADIATION BEAMS WITH (A) SURFACE-ON INCIDENCE AND WITH TILTED ANGLE INCIDENCE AT (B) 15° AND (C) 10° TILT ANGLES. BOTH EXPERIMENTAL AND SIMULATED SPECTRA ARE PRESENTED. 29

FIGURE 2.14 FOR TILTED ANGLE IRRADIATION THE THICKNESS OF THE CZT CRYSTAL MAY BE DECREASED WITHOUT SACRIFICING DETECTION EFFICIENCY. 30

FIGURE 3.1 COMPARISON OF LIKELIHOOD OF K X-RAY ESCAPE FOR DIFFERENT IRRADIATION GEOMETRIES, WITH PHOTON INTERACTION PROFILES SHOWN TO THE RIGHT OF EACH GEOMETRY. FOR (A) SURFACE-ON IRRADIATION PHOTON ATTENUATION OCCURS THROUGHOUT THE THICKNESS OF THE DETECTOR WHILE FOR (B) TILTED ANGLE IRRADIATION INTERACTIONS ARE MORE LIKELY NEAR THE DETECTOR SURFACE, INCREASING K X-RAY ESCAPE. 33

FIGURE 3.2 REPRESENTATIVE ENERGY SPECTRUM WITH PROMINENT CHARACTERISTIC X-RAY ESCAPE PEAKS. FOR CZT, THESE PEAKS ARE DUE MAINLY TO K ESCAPE FROM CD AND TE ATOMS. 34

FIGURE 3.3 (A) PHOTOELECTRIC EFFECT, RAYLEIGH AND COMPTON SCATTER FRACTIONS OF X-RAYS IN CZT. RAYLEIGH AND COMPTON SCATTER COMPONENTS ARE 7 % AND 10 % , RESPECTIVELY, AT THE HIGHEST ENERGY OF 120 KEV. AT AN AVERAGE ENERGY OF 60 KEV THESE COMPONENTS ARE DECREASED TO 4 % AND 2 %, RESPECTIVELY. (B) LINEAR ATTENUATION COEFFICIENT OF X-RAYS IN CZT MATERIAL.
DATA VALUES TAKEN FROM [41]. 36

FIGURE 3.4 CONTINUOUS SLOWING DOWN APPROXIMATION (CSDA) AND PROJECTED RANGE OF ELECTRONS IN CZT WITH RESPECT TO ENERGY. PHOTOELECTRIC INTERACTIONS WITH THE K SHELL OF CD AND TE ATOMS CAN EMIT PHOTOELECTRONS WITH ENERGY IN THE RANGE OF 0 TO 93 KEV. THEIR PROJECTED RANGE IS SMALL COMPARED TO THE ATTENUATION LENGTHS OF THE K X-RAYS EMITTED. 37

FIGURE 3.5 (A) PROCESSES INVOLVED IN X-RAY INTERACTIONS WITH DETECTOR MATERIAL: 1 – COMPLETE ABSORPTION OF THE PHOTOELECTRON AND K X-RAY, 2,3 – BACK AND FORWARD ESCAPES OF CHARACTERISTIC RADIATION, 4,5 – SIDE ESCAPES, 6 – SIDE ESCAPE OUTSIDE OF THE PIXELS. SCHEMATICS OF CHARACTERISTIC X-RAY CROSSTALK FOR (B) PIXEL, IN WHICH ALL ESCAPE CORRESPONDS TO TYPE-4 INTERACTION AND (C) STRIP DETECTORS, IN WHICH REABSORPTION WITHIN THE STRIP CORRESPONDS TO TYPE-1 BEHAVIOR. 38

FIGURE 3.6 SCHEMATIC OF THE CZT DETECTOR MODEL AND BEAM ORIENTATION. RELATIVE GEOMETRY OF SQUARE AND STRIP PIXELS ARE SHOWN; THE TILTED ANGLE X-RAY BEAM WAS DONE ONLY FOR STRIP PIXELS. 39

FIGURE 3.7 GEOMETRY OF PRIMARY PHOTON (E0) AND K X-RAYS FROM TE (D1) AND CD (D2) TRACKING SIMULATION. 40

FIGURE 3.8 FLOW CHART OF THE MONTE CARLO SIMULATIONS FOR TRACKING CHARACTERISTIC X-RAYS IN CZT DETECTOR. 41

FIGURE 3.9 GENERATION OF DEPTH OF INTERACTION VALUES, Z, USING A RANDOM NUMBER BETWEEN 0 AND 1 AND THE EXPONENTIAL RELATIONSHIP BETWEEN DEPTH AND attenuation. Solving for z will give, $z = -\tau(E) \times \ln(R)$, where t(E) is the attenuation length of photons with energy E and $R = I/I0$. 42

Figure 3.10 Geometry of the method used to determine K x-ray reabsorption position in the x,y-plane. (a) The side view is shown to demonstrate the value of r as determined from θ and d; (b) the view of the x,y-plane is shown to demonstrate determining the x- and y-coordinates of the K x-ray reabsorption position. 43

Figure 3.11 Schematic of mapping the primary photon to the center of the detector and then randomly spreading over the pixel area MxN. The distance of the reabsorption of the K x-ray from the origin was (u,v) which was then shifted randomly by dx and dy... 44

Figure 3.12 Depth attenuation profiles of K x-rays for primary photons with different energies, for (a) 90° and (b) 10° irradiations of CZT. 46

Figure 3.13 Fractions of the side escaped and back escaped characteristic x-rays versus x-ray energy for (a) square pixels and strip pixels with (b) 10 degree and (c) 90 degree tilt angles; (d) total escape fractions versus pixel size for 120 keV spectrum.. 47

Figure 3.14 Energy spectrum of primary x-rays (input spectrum), final x-ray spectrum deteriorated due to characteristic x-ray escapes, and components of the final spectrum resulting from different processes. Examples are shown for square pixels with (a) 0.1 mm and (b) 1 mm sizes, and for strip pixels with 0.1 mm width and (c) 90° and (d) 10° tilt angles.. 49

Figure 3.15 Full absorption spectra of primary x-rays compared to input spectrum for all pixel sizes and configurations: (a) square pixels, (b) strip pixels with normal irradiation, and (c) strip pixels with 10° tilted angle irradiation. 50

Figure 3.16 X-ray spectra deteriorated due to K x-ray escape with (a) square pixels, (b) strip pixels with normal irradiation, and (c) strip pixels with 10° tilted angle irradiation.. 51

Figure 3.17 2D maps of characteristic x-ray absorption and central profiles. The primary x-ray beam was shaped to a square beam normally incident on the CZT surface. The dotted rectangles indicate size and intensity of the primary x-ray beam. 52

Figure 3.18 2D maps of K x-ray absorption are shown. A large beam irradiated the CZT surface except for the square pixel areas at the center. The image profiles show contamination of the unexposed pixel by characteristic x-rays from surrounding areas. Pixel sizes were in the 0.1-1 mm range...................................... 53

Figure 3.19 Loss of spatial resolution due to K x-ray escape for (a) a 2D array of square pixels and (b) scanning slit imaging with a 1D array of strip pixels. Counts versus pixel positions are plotted. Spatial resolution is compared in (b) for four cases including square pixels, strip pixels at two irradiation angles, and a strip pixel in the scanning slit direction determined by slit width (chosen same as strip width). 54

Figure 3.20 Measured x-ray spectrum as compared to simulated and input spectra. The experimental spectrum was deteriorated more than predicted due to K x-ray escape. Other factors affecting the spectrum might be due to hole trapping, and charge sharing due to charge diffusion. 54

Figure 4.1 Pixel configuration of the CZT detector used for experiments. 57

Figure 4.2 (a) Readout electronics for each pixel are able to separate measurements in to energy bins. (b) X-ray energy spectrum of 120 kVp tube voltage split into 5 energy bins. Simulations were performed for the average energies in these energy bins. 58

Figure 4.3 Background object with embedded contrast object. The attenuation coefficients of each material for incoming photons, N_0, with energy E are $\mu_B(E)$ and $\mu_C(E)$, respectively. The number of photons transmitted through the background without and with contrast are given by N_B and N_C, respectively. 58

Figure 4.4 (a) Basic process of material decomposition by dual-energy subtraction. (b) Difference in attenuation coefficients between breast tissue and calcifications that might indicate breast cancer. 59

Figure 4.5 (a) Example of ideal energy spectrum compared to a practical detector and an available pixel detector. (b) Blurring across the borders of the energy bins for a polychromatic x-ray spectrum decreases energy-resolving advantages of the detector. 60

Figure 4.6 Measured spectra for several adjacent pixels for (a) ^{241}Am and (b) ^{57}Co. 60

Figure 4.7 Schematic of phantom including aluminum wires and $CaCO_3$ contrast. 61

Figure 4.8 (a-e) Spectral CT images of resolution phantom acquired in 5 energy bins and (f) the final CT image composed from 5 bin data. 62

Figure 4.9 Overlapping at the border between low and high energy bins for dual-energy subtraction limits the effectiveness of this technique. 62

Figure 4.10 Material decomposition with Spectral CT: (a) image of the resolution phantom, (b) tissue-cancelled image, and (c) $CaCO_3$ cancelled image. 63

Figure 5.1 Schematics of electric field lines and x-ray incidence in (a) a planar detector and (b) a capacitive grid detector. The interaction depth of the primary photon is given by z and the angle of incidence between the beam and the detector surface is given by a. 67

FIGURE 5.2 SCHEMATIC OF (A) PLANAR DETECTOR AND (B) CAPACITIVE GRID DETECTOR WITH HOUSING AND ELECTRODES. 68

FIGURE 5.3 PLANAR DETECTOR (TOP) AND CAPACITIVE GRID DETECTOR (BOTTOM). THE SMALL SIZE AND ABILITY TO OPERATE AT ROOM TEMPERATURE MAKE CZT DETECTORS IDEAL FOR CLINICAL USE. 68

FIGURE 5.4 SCHEMATIC OF THE X-RAY SYSTEM WITH ACRYLIC FILTER AND LEAD COLLIMATORS USED FOR X-RAY SPECTROSCOPY. 69

FIGURE 5.5 FLOWCHART OF THE MONTE CARLO SIMULATIONS FOR TRACKING BACK ESCAPE OF K X-RAYS FROM THE FRONT SURFACE OF THE CZT DETECTOR. 71

FIGURE 5.6 SPECTRA MEASURED WITH PLANAR AND CAPACITIVE GRID DETECTORS FOR ^{57}CO (122 KEV) AT INCIDENT ANGLES OF (A) 90° AND (B) 30°. AT 90° INCIDENCE HEAVY TAILING IS OBSERVED, ESPECIALLY FOR THE PLANAR DETECTOR. AT 30° ANGLE TAILING IS REDUCED FOR THE PLANAR DETECTOR AND NEARLY ELIMINATED FOR THE CAPACITIVE GRID DETECTOR. 74

FIGURE 5.7 SPECTRA WITH PLANAR AND CAPACITIVE GRID DETECTORS FOR ^{241}AM (59.5 KEV) AT INCIDENT ANGLES OF (A) 90° AND (B) 30°. AT 90° INCIDENCE SOME TAILING IS OBSERVED FOR THE PLANAR DETECTOR WHILE MINIMAL TAILING IS SEEN FOR THE CAPACITIVE GRID DETECTOR. AT 30° TILT ANGLE TAILING IS REDUCED FOR THE PLANAR DETECTOR AND ELIMINATED FOR THE CAPACITIVE GRID DETECTOR. 75

FIGURE 5.8 MEASURED, CORRECTED, AND SIMULATED 120 KVP SPECTRA. RESULTS WITH (A, B) PLANAR AND (C, D) CAPACITIVE GRID CZT DETECTORS ARE PRESENTED FOR (A, C) 90° AND (B, D) 30° IRRADIATION ANGLES. 76

FIGURE 5.9 MEASURED, CORRECTED, AND SIMULATED 80KVP SPECTRA. RESULTS WITH (A, B) PLANAR AND (C, D) CAPACITIVE GRID CZT DETECTORS ARE PRESENTED FOR (A, C) 90° AND (B, D) 30° IRRADIATION ANGLES. 77

FIGURE 5.10 MEASURED, CORRECTED, AND SIMULATED 60 KVP SPECTRA. RESULTS WITH (A, B) PLANAR AND (C, D) CAPACITIVE GRID CZT DETECTORS ARE PRESENTED FOR (A, C) 90° AND (B, D) 30° IRRADIATION ANGLES. 78

FIGURE 5.11 DIFFERENTIAL DEVIATIONS BETWEEN MEASURED SPECTRA AFTER K ESCAPE CORRECTIONS AND SIMULATED SPECTRA AT (A) 60 KVP, (B) 80 KVP, AND (C) 120 KVP TUBE VOLTAGES. 79

FIGURE A.1 SCHEMATIC OF ELECTRON-HOLE PAIR GENERATION DUE TO PHOTON INCIDENT AT ANGLE A WITH RESPECT TO CZT SURFACE. THE THICKNESS OF THE CZT IS *L* AND HOLES AND ELECTRONS TRAVEL A DISTANCE OF *Z* AND *L-Z*, RESPECTIVELY, AS THEY DRIFT TOWARD THEIR RESPECTIVE ELECTRODES. 84

FIGURE A.2 PLOT OF THE HECHT RELATION E(Z) AND ITS INVERSE Z(E), LEFT. IT WAS NECESSARY TO SPLIT Z(E) INTO TWO SEPARATE CURVES, LABELED A AND B, SINCE IT IS A MULTI-VALUED EXPRESSION, RIGHT. 85

Figure A.3 Screen shot of the differentiation of a curve in Origin 7, left, and the result of differentiating curves A and B. 86

Figure A.4 Plot of the product of dz/dE and dN/dz for each curve, A and B, left. Result of summing curves A and B at each value of E/E_0, right. 86

Figure A.5 Representative curve of the convolution kernel used in simulations. To convolve in origin the response curve must be symmetrical with an odd number of data points. The number of points must be less than half that of the signal dataset and it is recommended that the total counts be normalized to one to maintain total counts of the signal dataset. 87

Figure A.6 Screen shot of convolution using Origin software. The signal dataset is to the left of the response dataset in the worksheet and both are highlighted when the 'Convolute' option is chosen 88

Figure A.7 The final result of the theoretical spectrum convolved for noise, with the energy scaled to simulate the appropriate value of E0, in this case 120 keV........ 88

Figure B.1 Depth attenuation profiles for initial interaction of incident photon (G), top, and final interaction depth of characteristic x-ray (K), bottom. Note that due to back escape, counts at shallow depth in profile K are decreased compared to G. 93

Figure B.2 Image of intensity of final characteristic x-ray absorption position when beam is uniform over a square pixel. 94

ABSTRACT

Purpose: The purpose of this research was to characterize a photon counting cadmium zinc telluride (CZT) detector for medical x-ray imaging and spectroscopy purposes. The overall aim was to characterize CZT detector properties and to develop modifications and correction methods to address the limiting factors, making the detector clinically viable.

Methods: Hole trapping issues were investigated through simulation and experiments with a large area single pixel CZT detector under three different irradiation geometries: edge-on, surface-on, and tilted angle irradiation. Characteristic x-ray escape was simulated using Monte Carlo methods and compared to measurements with a small pixel CZT imaging detector. Monoenergetic sources were measured with the small pixel CZT imaging detector to investigate energy blurring. Spectroscopy measurements were made both with and without hole trapping and characteristic escape corrections, and compared.

Results: Tilted angle geometry improved the energy resolution compared to surface-on irradiation; peak-to-total ratios increased from 38% to 83% at 10° tilt for 122 keV. An increase was also seen for 59 keV, from 73% to 97% at 10°; simulation confirmed that tailing is a minor concern below 60 keV, even for surface-on irradiation. Characteristic x-ray escape simulations showed that side escape was less for strip pixels compared to square pixels (47% vs. 66% at 110 keV for 0.1 mm pixel width). Back escape increased from 27% for surface-on irradiation to 51% for 10° irradiation at 30 keV. For spectroscopy, modifications in detector geometry and electric field, as well as escape corrections, reduced the integral deviation between measured and true 120 kVp spectrum to 19% compared to 47% for operation without modification or correction.

Conclusions: We showed that a CZT detector for diagnostic x-ray spectroscopy is clinically feasible, requiring simple modifications to current technology. However, the energy resolution of small pixel CZT imaging detectors requires substantial improvement to achieve clinical utility; several avenues of development are available to drive a CZT imaging detector towards its desired performance level. With these developments, advanced imaging systems using tilted-angle strip geometry, e.g., for photon-counting breast imaging, are likely to become feasible for routine clinical use.

1 INTRODUCTION

Medical imaging with x-rays is one of the most common methods of diagnosing and monitoring disease. It has existed since the first x-ray of a human hand was made by Roentgen in 1895 [1]. Much is known about x-rays, and imaging methods have been optimized to produce high quality imaging systems that create useful images for all sorts of conditions, including heart disorders, cancer, and broken bones.

With the advances in computing and electronic devices available today, even more can be done to efficiently use all information available in an x-ray imaging system. The detector investigated in this study, cadmium zinc telluride (CZT), has the ability to count each x-ray photon separately as well as to measure the energy of each photon. The photon counting, energy-resolving capability of the CZT detector makes more efficient use of available information. It can lead to lower patient dose and shorter scan times for images that exhibit more quantitative information and equal or better quality than is currently available [2, 3].

Although CZT detectors are the current state of the art for room temperature photon counting x-ray detectors [4] there are several factors that weaken the performance of these detectors. These factors include hole trapping, characteristic x-ray escape, and charge diffusion. This research investigated methods to reduce the effects of hole trapping and characteristic x-ray escape. These corrections were then applied to a single pixel CZT detector used for x-ray spectroscopy in the diagnostic energy range to test their effectiveness. With the methods used in this study a clinically applicable CZT detector is feasible in the near future with superior image quality capability compared to conventional detectors. Even more immediate is the availability of a CZT detector for accurate and reliable x-ray spectroscopy that can be performed in the clinic with a compact, room temperature device.

This thesis is divided into five chapters. Chapter 1 gives a brief overview of the principles of medical x-ray and CT (computed tomography) imaging. It describes current clinical detection systems and the need for improvement in these systems. The photon counting CZT detector is presented along with an explanation of why it is potentially superior to conventional detectors.

The next two chapters describe limitations of the CZT detector and efforts in the present research to account for and correct these limitations. In particular, Chapter 2 describes hole trapping in the detector, and simulations and experiments done in an effort to reduce its effect by manipulation of irradiation geometry. Chapter 3 considers characteristic x-ray escape in the detector and its effect on energy and spatial resolution. Correction methods for characteristic x-ray escape were developed to apply to measured x-ray spectra.

Chapter 4 describes an experimental imaging system with a multi-pixel CZT detector. Sample images are shown that indicate the possibilities of photon counting spectral CT imaging with a room temperature CZT detector. The limitations of the detector are reviewed, and the need for future research to make the CZT detector clinically applicable is discussed.

Finally, Chapter 5 describes spectroscopy of diagnostic x-rays done with a CZT detector. Corrections for hole trapping and characteristic x-ray escape were done and the corrected spectra were compared to spectra simulated with a program called SpekCalc [5].

1.1 Principles of Medical X-ray Imaging

The most basic structure of a medical imaging system consists of an energy source, an object (patient) that interacts with the output of the source, and a detector that records the results of that interaction [1, 6-8]. Energy sources vary depending on the imaging modality. Non-ionizing radiation systems include magnetic resonance imaging (MRI), which uses RF frequency in a magnetic field, and ultrasound imaging, which uses sound waves. Many other imaging modalities use ionizing radiation as the energy source. These include positron emission tomography (PET) and single photon emission tomography (SPECT), both of which utilize gamma-rays from radioactive isotopes. X-rays are used as the energy source for projection radiography and computed tomography (CT). This work studies CZT detectors used for x-ray and CT imaging systems and henceforth uses the terms radiation, x-rays, and photons interchangeably.

1.1.1 X-rays

X-rays are part of the electromagnetic spectrum, as shown in Figure 1.1. The energy has an electric field component and a magnetic field component. The electromagnetic spectrum ranges from low energy waves, such as radio waves and microwaves, to high energy waves like x-rays and gamma rays. X-rays span the spectrum from approximately 100 eV and higher (10 nm and smaller).

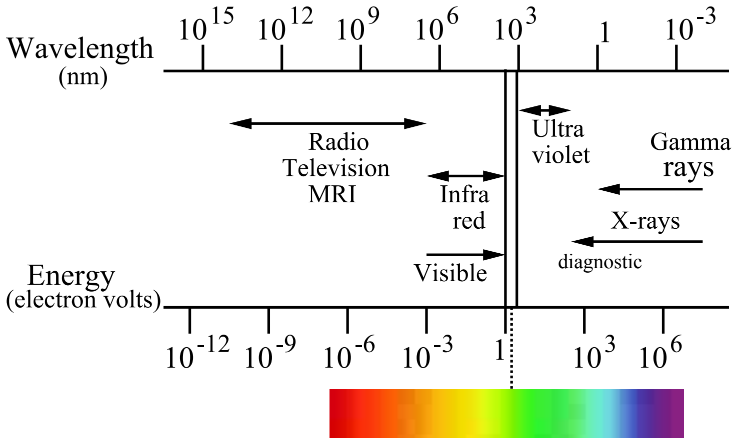

Figure 1.1 Electromagnetic spectrum; x-rays used for diagnostic purposes typically fall between 20 and 140 keV.

X-rays used for clinical imaging are usually generated in an x-ray tube, typically a tungsten rotating anode tube. High energy electrons strike a target and lose energy as they interact with the atoms in the target. These interactions cause the electrons to slow down. As they slow down the electrons radiate energy in the form of bremsstrahlung (braking radiation) x-rays. The outgoing x-ray beam has a continuous range of energies, and is characterized by the maximum or peak kilovoltage (kVp). Thus a 120 kVp x-ray beam has a maximum energy of 120 kiloelectronvolts (keV) and may include energies as low as 20 keV, depending on filtration of the low energy part of the beam. The x-ray spectrum from a tungsten target typically looks like that shown in Figure 1.2. The sharp peaks are characteristic of the target material, in this case tungsten which has prominent peaks at 59 and 67 keV.

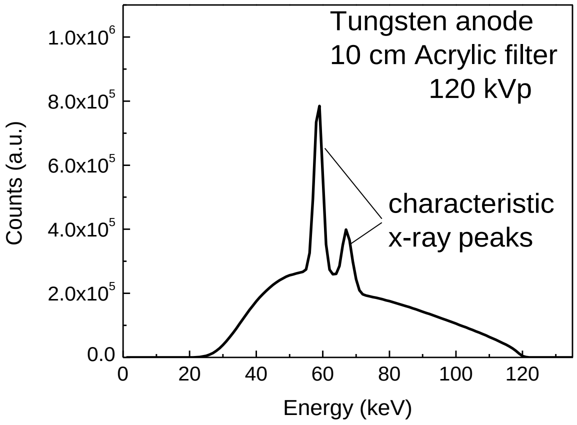

Figure 1.2 Typical x-ray spectrum for a 120 kVp beam with tungsten target, filtered with 10 cm acrylic. The sharp peaks are a result of characteristic x-rays from tungsten at 59 and 67 keV.

X-rays interact with electrons in the object being imaged and deposit energy. They may be completely absorbed or scattered, changing direction and losing energy. X-rays with different energies interact differently in a given material. The probability of interaction changes with x-ray energy as well as the atomic number, atomic mass, and density of the material. Thus, for a particular imaging task, the optimal peak x-ray energy is chosen based on the desired characteristics of the final image.

Images are created by detecting x-rays transmitted through the patient. The basic process of image acquisition is shown in Figure 1.3. Information about the probability of interaction of x-rays of a certain energy is contained in the attenuation coefficient, μ, of the material. X-rays that do not interact are transmitted through the object and interact with the detector where a signal is recorded. The image is therefore the shadow cast by the object and its internal structure. Biological damage may occur if x-ray interactions deposit too much energy in the object.

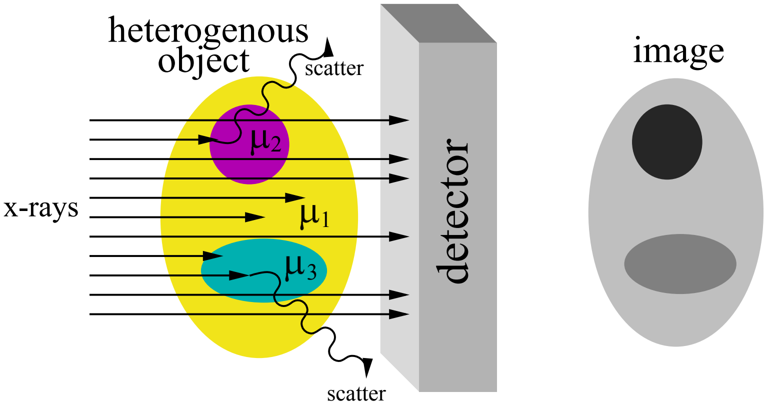

Figure 1.3 Schematic of the basic principles of an x-ray imaging system. X-rays incident on an object composed of different materials (heterogeneous) will interact differently based on the attenuation coefficient, μ, of the material. The resulting image is essentially the shadow cast by the object being illuminated by x-rays.

Two common types of x-ray imaging modalities were mentioned previously: projection radiography and CT. The detector described in this work may be used for either type. In general, x-ray imaging will refer to projection radiography. Projection radiography projects a three-dimensional object onto a two-dimensional plane. The process results in overlap of the internal structure of the object. This type of imaging is commonly used to image the chest, breast, and broken bones and accounts for more than half of all diagnostic images produced [1]. One specific type of projection radiography, mammography, is optimized to image features internal to the breast. CT is similar to projection radiography except that the x-ray source and detector are rotated around the patient, generating many projection radiographs (typically 400-800) [1]. These projections are then used to reconstruct a 3D volume image of the distributions of the μ in the object. CT imaging eliminates overlap and thus creates a more accurate image of internal structure.

1.1.2 Role of Energy in X-ray Imaging

The differences in the way materials interact with x-rays are what create contrast in an image. That is, materials with a higher attenuation coefficient for a given photon energy will not transmit as much of the x-ray beam as those materials with a lower attenuation coefficient. For example, bone is a dense material and will not transmit as many x-rays as soft tissue. The detector records higher intensity in areas of soft tissue than in bone because more photons are transmitted through soft tissue and reach the detector.

Some materials of interest may have very similar attenuation coefficients, in which case it is difficult to obtain sufficient contrast to distinguish them. Figure 1.4 shows attenuation coefficients in breast tissue for fat and glandular tissue.

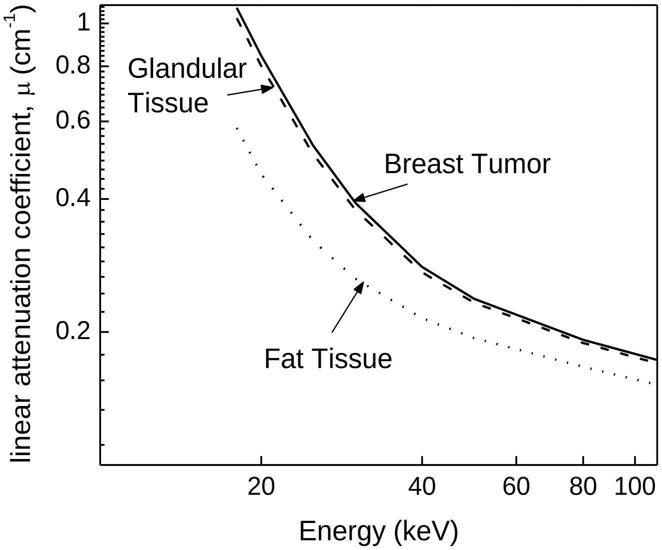

Figure 1.4 Attenuation of photons with respect to energy for fat and glandular breast tissue and for breast tumors. Values for μ are taken from [9].

When examining images for breast tumors, it is easy to distinguish fat from tumor tissue but difficult to see contrast between glandular and tumor tissue. The differences in attenuation coefficients increase for lower energies, therefore mammography generally uses x-ray energies on the order of ~30 kVp. Higher energy x-rays however are better able to penetrate thick objects. Thus, x-ray energies are optimized for each imaging task separately. X-ray tube voltages used in mammography, projection radiography, and CT are in the ranges of 25 – 40 kVp, 60 – 120 kVp, and 80 – 140 kVp, respectively, to achieve the desired balance of contrast and penetration.

1.1.3 Image Quality

The success of a medical imaging system depends on the usefulness of the image to lead to a correct diagnosis. Thus, a high quality image is one that is able to do this, generally with high contrast between tissue components and the ability to distinguish small objects, especially for diagnosing cancer. With x-ray imaging there is a trade-off between image quality and patient radiation dose. Increasing the intensity of x-rays improves image quality because it reduces inherent statistical noise of the x-ray photons passed through the object. This increases radiation dose and thus risk to the patient. To keep patient dose to an acceptable level it is important to have a detector that will efficiently absorb x-rays and reveal sufficient information.

- **Early detection of breast cancer**

In 2007 it was estimated that more than 40,000 women would die from breast cancer in that year alone [10]. In addition more than 200,000 new cases were expected. The benefit of high quality imaging can be seen when considering the survival rates of breast cancer patients when the cancer is detected early. Figure 1.5 shows the relationship between 15-year survival rates for patients with breast tumors and tumor size.

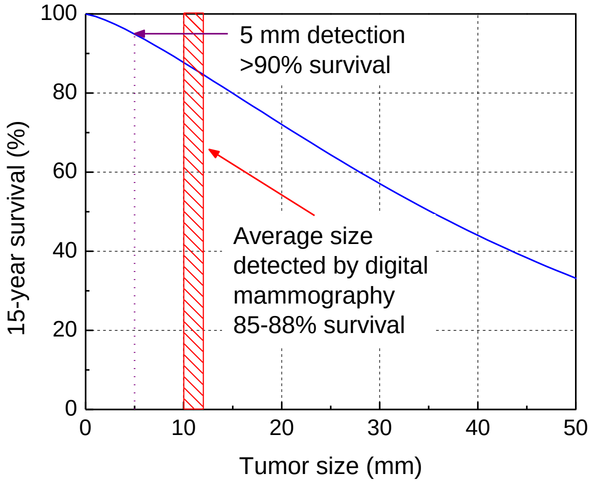

Figure 1.5 Relationship between 15-year survival rates and tumor size. Curve was generating using the equation SF = $[\exp(-QD)]^z$, where SF is surviving fraction, D is tumor size, and Q and z are constants [11, 12].

On average, mammography is able to detect tumors with 10-12 mm size. This corresponds to 85-88 % survival rates and is the reason why women are encouraged by the American Cancer Society to be screened annually after age 40 for breast cancer. (This recommendation is currently a topic of debate, as the US Preventative Task Force now recommends annual screenings after 50 years of age. Both agency recommendations can be found in [13].) If cancer could be detected when it is even smaller, 5 mm for instance, survival rates would be expected to increase to over 90 %. This is an example of the importance of improving image quality.

Improvements in x-ray imaging technology are needed to better diagnose breast cancer and monitor patient treatment without increasing patient dose. For several reasons, the initial implementation of the photon counting CZT detector will likely be for breast imaging. This is due to the fact that breast imaging imposes relatively lower demands to photon counting detectors compared to body imaging. The breast has smaller size, lower x-ray attenuation, and uniform tissue content (that is, the breast lacks bone and air, both of which make chest imaging difficult) which facilitate application of this new technology.

- **Factors that influence image quality**

Detectors can be classified by how they extract information from the x-rays transmitted through the object. It may be said that the more information a detector is able to extract, the more superior the quality of the image created using that detector. Image quality can be deteriorated by the presence of noise. It is desirable to have the image signal much higher than the noise. The ratio of signal to noise (SNR) is one of the major criteria used to evaluate image quality. The parameter that is most often used to describe the quality of an imaging system is the detective quantum efficiency (DQE). The DQE, given by equation (1.1), is determined as the square of the ratio of the output SNR to the input SNR.

$$\mathrm{DQE} = \frac{\mathrm{SNR}_{\mathrm{out}}^2}{\mathrm{SNR}_{\mathrm{in}}^2} \tag{1.1}$$

Since x-ray counting statistics obey the Poisson distribution, increasing the number of interactions decreases the relative noise in an image [1, 14]. The relative noise is given by the inverse of the square root of the number of counts, N. Since the SNR is inversely proportional to the relative noise, it increases when the number of counts increases according to

$$SNR \propto (relative\ noise)^{-1}$$
$$SNR \propto \sqrt{N} \tag{1.2}$$

The relationship between SNR and the number of counts detected means that to double SNR, patient dose must increase by a factor of four. Therefore the quality of an x-ray image is limited because patient dose must be kept to an acceptable level. As a result it is important to extract as much information as possible from the x-rays that are detected.

The DQE parameter quantifies only the ability of the detector to absorb incident x-rays and not its ability to resolve individual x-rays or measure the energy of these x-rays [15]. Until recently detectors have not had the ability to resolve individual x-ray photons and measure their energy. However, extracting energy information in x-ray and CT imaging can be a useful tool to provide more quantitative image data, improve image quality and even reduce the amount of radiation needed to create a useful image.

1.2 Detectors for X-ray Imaging

The first detectors used for x-ray imaging were photographic plates. These detectors were replaced by film. Recently digital detectors have begun to replace film. CT uses digital detectors to reconstruct three-dimensional images using computer software that requires digital data. Though in general the spatial resolution of digital systems is lower than that of film due to pixel size constraints, there are many advantages to digital images [1]. Digital images can be acquired quickly, electronically transmitted and duplicated. Storage of digital images is also easier because less space is needed. One of the biggest advantages is the ability to adjust contrast in a digital image.

As advancements are made in computing and electronic capabilities, digital detectors are being optimized to increase image quality and reduce patient dose. A digital detector generally consists of a matrix of pixels. Radiation interacts in the detector pixel and creates charge. The signal extracted from a pixel depends on the amount of charge generated in that pixel by an x-ray photon. Therefore the resulting image is a map of energy fluence with respect to position.

Two main types of detection systems for x-ray imaging are “charge-integrating” (or “energy-integrating”) and “photon counting” [16]. Schematics of the detection process for each are shown in Figure 1.6. Charge-integrating detectors are so-called because they record the total charge generated by many x-ray photons during image acquisition. Charge is collected by the electronics and the output is the sum of all charge generated. The charge generated by a photon interaction depends on the energy of the photon so that the resulting signal is proportional to photon energy. In this way, photons with higher energy are weighted more in the resulting image than lower energy photons. However, greater attenuation differences are usually found at lower energies so this can be a disadvantage for image contrast.

Detectors that count photons individually are known as photon counting detectors. Charge generated by each photon in a detector pixel is sent to readout electronics which separate, or bin, the photon counts according to charge generated [17]. Again, the charge generated is dependent on the photon energy. Therefore, photon counting detectors have the ability to resolve photon energy and make use of a technique known as “energy-weighting”. The following sections describe the types of detectors used for charge-integrating and photon counting and the advantages of photon counting, energy-weighting detectors.

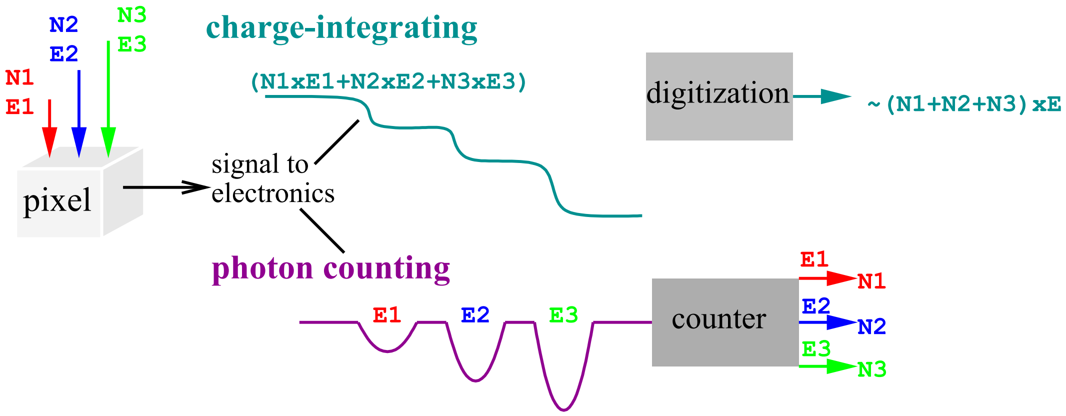

Figure 1.6 Charge-integrating detectors record total charge for all interactions. Signal is received by the digitization electronics and the sum of all charge is recorded. Photon counting detectors resolve individual interactions and allow for energy-resolving capability.

1.2.1 Indirect Detection

Indirect detectors convert x-ray energy into charge indirectly. For example, instead of detecting charge directly from a photon interaction, the photon interacts in a scintillation material and produces light, as shown in Figure 1.7. The light is then incident on a photodetector (photodiode or photocathode) where electric charge is created. To achieve high signal to noise ratios it is desirable to convert x-ray energy to charge directly avoiding intermediate steps.

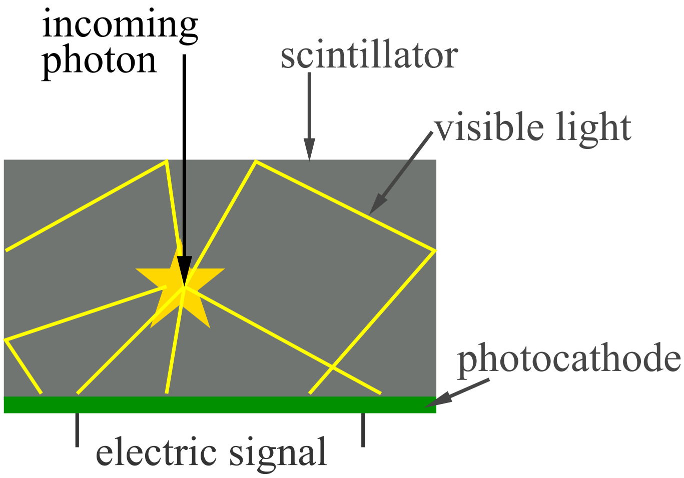

Figure 1.7 Schematic of indirect detection with a scintillation detector. The incoming photon interacts in the scintillation material to produce light. The light photons are then incident on the photodetector and electric charge is created.

1.2.2 Direct Detection

Direct detection of photons can be done using semiconductor material in place of scintillation material, as shown in Figure 1.8. Semiconductors directly convert photons to charge in the form of electron-hole pairs, without the light conversion step inherent in scintillation detectors. An electric field is applied to the semiconductor material and signal is generated as charge moves to the electrodes. Since a significant amount of noise is eliminated, semiconductor detectors are able to resolve individual photons and are thus able to use the photon counting electronics mentioned previously.

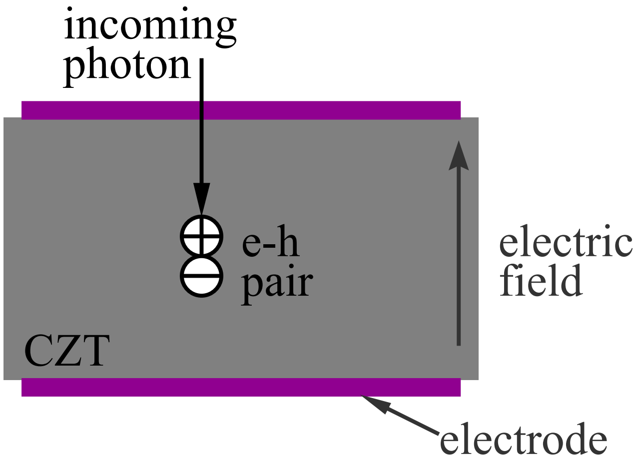

Figure 1.8 Schematic of semiconductor detector which uses direct detection. An electric field is applied to the semiconductor material. The incoming photon generates charge in the form of electron-hole pairs (e-h) and signal is generated as the charge moves to the electrodes.

- **Energy-resolving**

As stated previously, contrast in an image is created based on differences in the attenuation coefficients in the imaged object. The attenuation coefficient depends not only on the object but also the energy of the photon. Differences in attenuation coefficients (μ) for patient tissue are generally greater for lower energy photons. Energy-weighting exploits these differences through the use of a weighting factor that optimizes the SNR of the image [15]. It has been shown that energy-weighting can greatly improve SNR and contrast in an image at or below radiation dose levels found in conventional imaging systems [2, 3, 17]. Recent advances in computing technology and semiconductor detector materials have made photon counting, energy-resolving detection systems feasible for some clinical applications, however, these detectors remain suboptimal for most clinical applications.

1.3 Applications for Photon Counting, Energy-resolving Detectors

The most promising semiconductor candidate for photon counting, energy-resolving detectors is cadmium zinc telluride (CZT) [4]. CZT has a relatively high density and atomic number that make it efficient for detecting x-ray photons in diagnostic energy range. It can also be operated at room temperature, unlike some semiconductors which must be cooled to operate effectively. Room temperature operation reduces both cost and size of the detector, as cooling can be expensive and there is not the need for a bulky cooling apparatus. Another advantage of CZT is that large-area crystals can be grown more easily at a reasonable cost than with Si or Ge. Also, in CZT the energy required to generate electron-hole pairs is relatively small so that even low energy photons create a sufficient amount of charge. This increases statistics and decreases noise.

1.3.1 Breast CT

The most likely clinical application for photon counting CZT detectors is with a dedicated breast CT, shown in Figure 1.9. Breast imaging is one of the areas that would benefit most from improvements in image quality. The recommendation for yearly mammograms raises concerns about the amount of radiation received by those screened. However, the benefit of early detection of small tumors illustrates the utility of yearly screening. Therefore, image quality must be increased while radiation dose levels are maintained or, preferably, decreased. It has been shown that dose reduction is feasible with a photon counting detector [18].

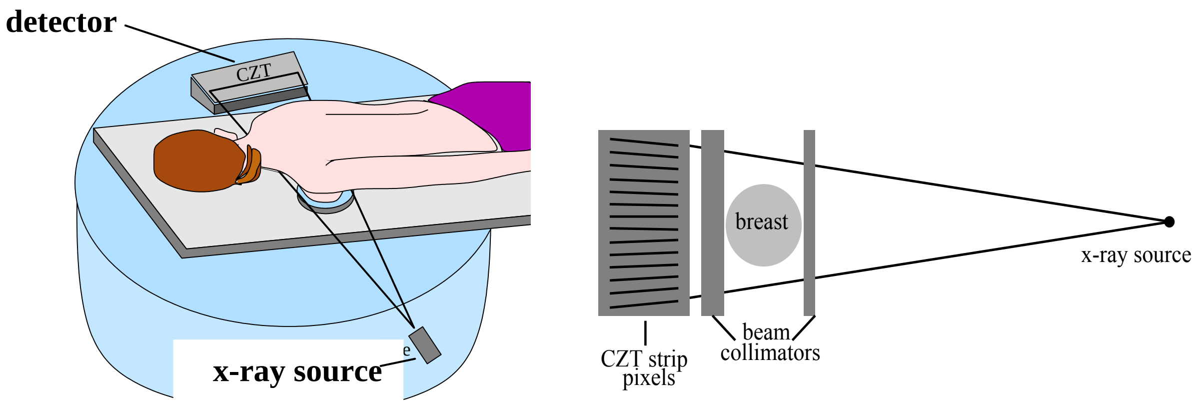

(a) (b)

Figure 1.9 (a) Schematic of detected breast CT system with patient lying prone on a table that houses the x-ray source and detector. (b) Schematic of the imaging system from above. The source and detector are rotated in tandem around the breast.

In addition, the small size and relatively uniform composition of the breast make it an ideal candidate for the application of this new technology.

1.3.2 Dual Energy Subtraction

The differences in attenuation coefficients of different materials can be accentuated using a technique called dual energy subtraction [1]. To use this technique with a charge-integrating system, two images must be acquired at different values of kVp, one at low kVp and another at high kVp. The two images are then processed and subtracted to cancel out one of the materials present in the image. These materials are usually highly attenuating material such as bone and a less attenuating material such as soft tissue, or highly attenuating contrast agent such as iodine and less attenuating soft tissue. Because two images at low kVp and high kVp are acquired within some time interval, the resulting subtracted image may suffer from spatial blurring if there is any patient motion between the two acquisitions. In addition, the patient receives greater radiation dose than with a single image. An energy-resolving detector has the ability to separate a single image acquired at a single kVp into two images with high and low energy. This is possible because a photon counting detector can resolve x-ray energies and split the x-ray spectrum into low energy and high energy parts. Thus, dual energy subtraction can be performed with a single image acquisition, improving spatial resolution and reducing patient dose.

1.3.3 X-ray Spectroscopy

Many areas involved with diagnostic x-rays require accurate characterization of the energy spectrum of the x-ray beam generated by the x-ray tube. Radiation protection and dosimetry calculations depend on complete knowledge of the energy spectrum of the x-ray beam. Also, to determine the detection efficiency of an imaging detector, the input spectrum must be known. Spectral CT and x-ray imaging also require accurate x-ray spectroscopy. Currently there is no easy method for routine x-ray spectroscopy that can be done in the clinic. Photon counting CZT detectors offer a method for x-ray spectroscopy that can be done with a compact, room temperature device.

1.4 Motivation to Characterize CZT Detectors

Although there are many advantages to using CZT for photon counting detectors, there are currently limitations in the detector that must be addressed. These include hole trapping, charge sharing, and count rate limits. Hole trapping affects charge collection efficiency and severely distorts the energy resolution capabilities of the detector. The effect depends on many variables, including density and location of crystal defects. Therefore, hole trapping must be addressed by physical manipulation of detector properties. Charge sharing between pixels also decreases energy resolution and, in addition, causes spatial blurring. Charge sharing occurs due to two major phenomena: characteristic x-ray escape and charge diffusion. Characteristic x-ray escape is predictable and can be simulated to correct spectra deteriorated due to this effect. The effect of charge diffusion can potentially be reduced by using coincidence circuits between neighboring pixels. Count rate limits can also be addressed through the use of improved CZT detectors with lower hole trapping and faster readout electronics.

The overall aim of this project was to characterize CZT detector properties and develop modifications and correction methods to address the limiting factors and make the detector clinically viable. The specific aims of the project were: 1) address hole trapping issues, 2) address characteristic x-ray escape, 3) investigate energy resolution in a CZT imaging detector, and 4) implement results of aims 1 and 2 for x-ray spectroscopy with a CZT detector.

2 EFFECT OF IRRADIATION GEOMETRY ON ENERGY RESOLUTION

For an ideal energy resolving detector, the same signal amplitude is generated for all interactions of photons with a given incident energy. The reality for CZT detectors is that the signal depends on two main factors: 1) the energy of the incident photon and 2) the depth in the detector that the interaction takes place. This depth dependence is due to a phenomenon known as hole trapping and results in tailing of the energy spectrum toward low energies, distorting the energy resolution [14, 19]. The effect of tailing on a monoenergetic spectrum is illustrated in Figure 2.1. Hole trapping depends on many variables including crystal purity, which may vary among detectors. Therefore, low energy tailing of the spectrum may not be easily corrected. A small pixel detector suffers less from spectral tailing due to hole trapping because of what is known as the small-pixel effect [19, 20]. Calculations of this effect are done using the Shockley-Ramo Theorem [14, 21, 22]. The study of the small-pixel effect is not in the scope of this research and could be a separate project in itself because of its complexity. Instead, we consider manipulating detector geometry as a physical means to reduce hole trapping effects.

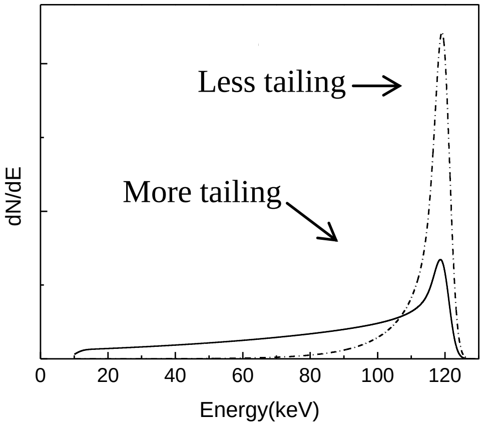

Figure 2.1 Example of ideal spectrum (dashed line) and spectrum with low energy tailing (solid line) for a monoenergetic 120 keV source.

Several possibilities of detector geometry for digital x-ray imaging exist, each with its own advantages and disadvantages. Modalities such as chest x-ray and mammography typically use a two-dimensional array of square pixels [1]. The x-ray beam is incident simultaneously on all pixels, at a 90º angle with respect to the central portion of the detector. This geometry allows for a large area to be imaged in a short amount of time, which decreases image blurring due to patient motion.

A disadvantage is the difficulty in rejecting x-rays scattered in the patient which reduces image contrast. Anti-scatter grids may be used to reduce scatter, however, these grids absorb a certain amount of primary radiation and thus decrease detection efficiency. The use of scanning slit geometry allows for efficient scatter rejection because it uses a fan shaped beam and fewer or even single rows of detector pixels. In this geometry, shown in Figure 2.2, a pre-collimator is positioned in front of the object and a post-collimator, with small slit size, is positioned between the object and the detector [23]. This geometry with an edge-on detector has been applied to digital mammography using Si detectors [24], and has been proposed for x-ray imaging with a microchannel plate detector [25] and for CT imaging with a CdTe detector [23]. Tilted angle irradiation has been proposed for CT imaging with a CZT detector [17]. The use of scanning slit geometry allows for the option of irradiating the edge of the detector or the surface of the detector at a low tilt angle, as opposed to normal to the surface of the detector. This is a more complicated geometry mechanically and acquisition time is longer since the irradiated area of the detector within a given time is smaller than for full field acquisition. However, in addition to scatter rejection, edge-on and tilted angle geometry can also reduce the effects of hole trapping and improve energy resolution. This chapter describes simulations and experiments with different detector geometries aimed to reduce hole trapping and its effect on the energy spectrum.

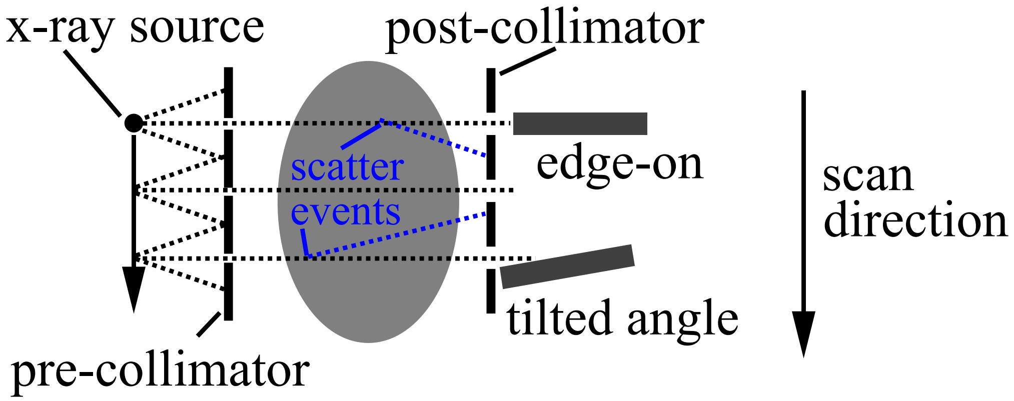

Figure 2.2 Schematic of scanning slit image acquisition. Detector may be positioned in either edge-on or tilted angle geometry and moved along the scanning axis in small increments. The step size of the detector determines the spatial resolution in that direction.

2.1 Signal Generation

To understand how the energy signal is distorted in a CZT detector we must first know how signal is generated. The signal depends greatly on the properties of the CZT crystal, which can be found in Table 2.1.

Table 2.1 Properties of eV Products CZT

$Cd_{0.9}Zn_{0.1}Te$	
Atomic Numbers	48, 30, 52
Average atomic number	49.1
Density (g/cm^3)	5.78
Band Gap (eV)	1.572
Dielectric constant	10.9
Pair creation energy (eV)	4.64
Resistivity (Ω·cm)	3×10^{10}
Electron mobility μ_e(cm^2/Vs)	1000
Electron lifetime τ_e(s)	3×10^{-6}
Hole mobility μ_h(cm^2/Vs)	50-80
Hole lifetime τ_h(s)	10^{-6}

Usually the geometry of the detector is configured in what is known as planar geometry, a rectangular slab of CZT crystal with a thin metal electrode on either side, shown in Figure 2.3.

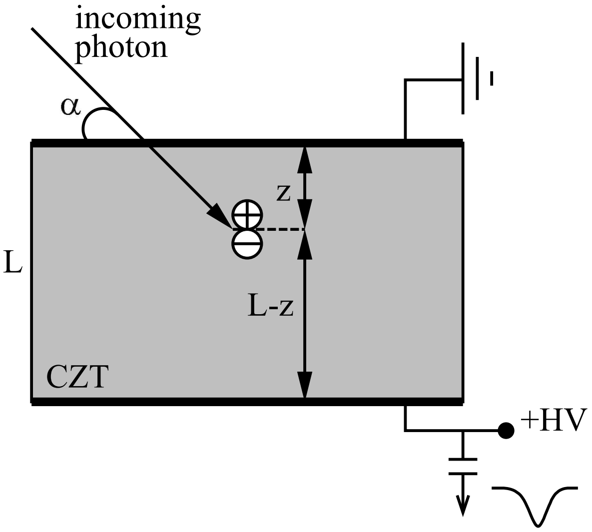

Figure 2.3 Schematic of signal generation in a planar CZT detector for radiation incident at an angle α between the beam and detector surface.

The photon beam is typically incident at an angle of 90º, or normal with respect to the detector surface. The thickness of the CZT is on the order of several millimeters. Typically, a negative voltage is applied to the electrode on which the photons are incident and the other electrode is grounded, so that a uniform electric field is applied within the crystal. Photons in the diagnostic energy range, 20–120 keV, interact primarily through the photoelectric effect [26] and create electron-hole pairs. The number of pairs created is directly proportional to the energy of the incident photon. For CZT, the energy required to create one pair of charge carriers is 4.64 eV [27].

Created charge moves to the electrodes due to the applied electric field. Holes move to the negative electrode while electrons move toward the opposite electrode. As the holes and electrons move in the CZT volume, a current is induced at the outer circuit connected to the CZT surface. This current is collected in the capacitor and the corresponding charge of the capacitor represents a photon signal. The recorded signal is the total induced charge created by the induced current within the collection time. When charge stops moving through the detector it no longer contributes to the signal. This occurs when either: (a) the charge reaches its electrode, or (b) the charge is trapped in the CZT crystal. Consider the ideal case with no charge trapping. For any position of interaction along the depth of the detector, the total distance traveled by an electron-hole pair is equal to the thickness of the detector, L. Therefore the resulting signal does not vary with the depth of interaction, because the total distance traveled by the pair is constant. The recorded signal thus depends only on the number of charge carriers created, which is determined by the energy of the incident photon. In reality, the holes frequently become trapped in the detector, a phenomenon known as hole trapping, which results in depth dependent signal amplitude, one of the major problems with current CZT technology.

2.2 Hole Trapping

The mobility of a charge indicates how fast it is able to move through the crystal to the electrode in a given electric field. Holes become trapped in CZT because they have relatively small mobility and cannot reach their electrode within the collection time. Hole mobility in CZT is about 20 times smaller than that of electrons, as shown in Table 2.1. This means that nearly all the signal is due to electron motion. The distance traveled by the electron depends on the depth at which the incident photon interacts. Thus the signal becomes depth dependent due to hole trapping.

The probability of interaction is high at the incident surface of the detector and decreases exponentially with depth. The number of incident photons N_0 with energy E expected to be absorbed within a depth *z* of a material with linear attenuation coefficient μ is given by N(z) and is highest when z is small, that is, at the detector surface, as is demonstrated by

$$N(z) = 1 - N_0 e^{-\mu(E)z} \tag{2.1}$$

The value of μ generally decreases with increasing photon energy and interactions may take place deep in the detector where electrons need travel only a short distance before reaching the electrode. In this case the recorded signal is small because current is induced for a short amount of time. Thus, photons with the same energy can generate different signal amplitudes depending on the depth of interaction, meaning energy resolution is degraded.

2.2.1 Hecht Formalism

The depth-dependence of the recorded energy is given by the Hecht equation [28, 29]

$$E(z) = \frac{E_0}{L}\left\{\lambda_e(\varepsilon)\left[1 - \exp\left(-\frac{(L-z)}{\lambda_e(\varepsilon)}\right)\right] + \lambda_h(\varepsilon)\left[1 - \exp\left(-\frac{z}{\lambda_h(\varepsilon)}\right)\right]\right\} \tag{2.2}$$

where E_0 is the energy of the incident photon, L is the thickness of the detector, z is the distance from the incident surface where the interaction takes place (see Figure 2.3), and $\lambda_e(\varepsilon)$, $\lambda_h(\varepsilon)$ are the mean free drift lengths of electrons and holes, respectively, which are dependent on electric field, ε.

The mean free drift length of electrons or holes is given as $\lambda_x(\varepsilon) = (\mu\tau)_x\varepsilon$, where μ is the charge mobility (not to be confused with the symbol for linear attenuation coefficient which is also μ), τ is the lifetime of the charge, ε is the applied electric field, and x is electrons (e) or holes (h). For planar geometry, the electric field is constant through the detector volume. The product $(\mu\tau)_x$ is specific to the detector material and is different for each charge carrier. It is difficult to measure and varies significantly with defects in the material. Therefore, corrections of deteriorated spectra are difficult to apply broadly because $(\mu\tau)_h$ may vary significantly in a single detector.

The Hecht equation (2.2) shows that if the mean free drift lengths of both electrons, λ_e, and holes, λ_h, are large, the exponential terms approach zero and signal does not depend on depth, z. This is shown graphically in Figure 2.4 (a). The normalized amplitude E/E_0, where E is the recorded energy and E_0 is the energy of the incident photon, is constant with respect to z. In reality holes have a much smaller mean free drift length than electrons, ~100 times smaller, and as interaction depth increases the signal amplitude is severely suppressed. The result is shown in Figure 2.4 (b) where electron and hole free drift lengths are assumed to be 30 and 0.24 mm, respectively, as found in literature [19] at a typical applied electric field of 100 V/mm. The low amplitude signal is interpreted by the detection system as a low energy interaction and results in incorrect low energy tailing of the spectrum. A more detailed treatment of the derivation of the Hecht formula can be found in [14, 28, 30].

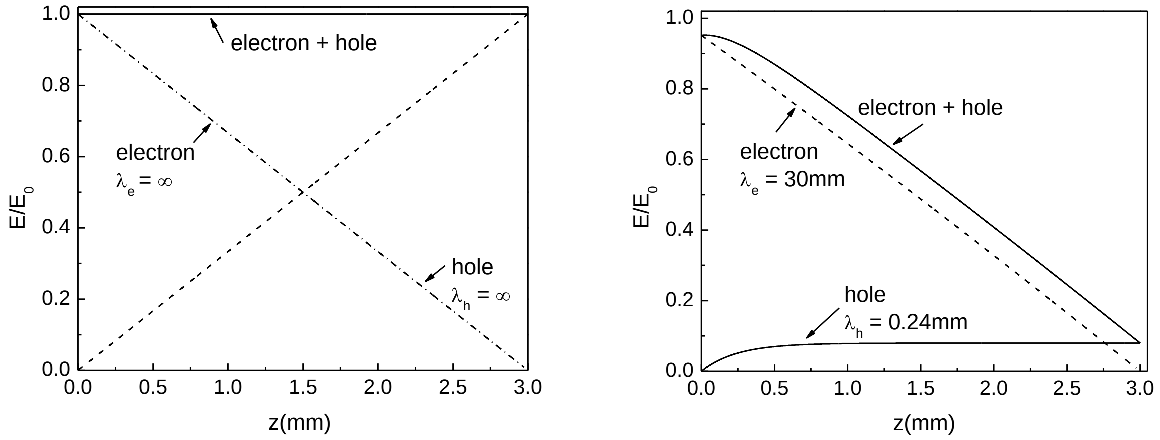

(a) (b)

Figure 2.4 (a) Signal amplitude with respect to depth of interaction for an ideal detector and (b) a detector with hole trapping.

2.3 Investigations to Reduce Spectral Tailing

To exploit the energy-resolving capability of the CZT detector and make it clinically useful for spectral x-ray and CT imaging, as well as for x-ray spectroscopy, issues with low energy tailing must be resolved. One solution is modification of the interaction depth of the incident photons so that most interactions take place near the detector surface [7]. In this case, the distance traveled by electrons during signal generation is more uniform. In [30], we investigated low energy tailing of monoenergetic radiation from isotope sources for various irradiation geometries of the incident photon beam with respect to the detector. The different geometries are shown in Figure 2.5 . Edge-on and titled angle geometries were compared to conventional surface-on geometry to determine improvement in energy resolution. It was shown that edge-on irradiation with a narrow beam (diameter 0.3 mm) and titled angle irradiation with a wide beam (diameter 1.0 mm) greatly reduced the amount of low-energy tailing of monoenergetic spectra. This section gives an overview of the simulations and experiments. The results quantify the degree to which energy resolution can be improved by modifying the interaction depth of the incident photons [17].

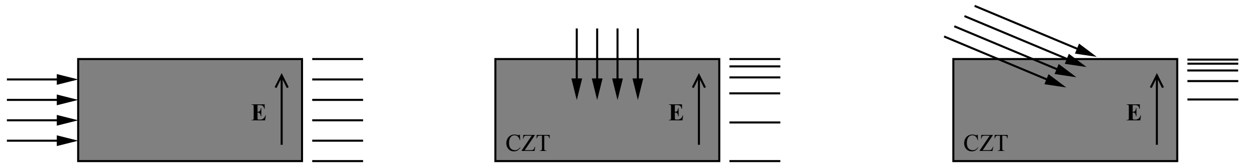

edge-on surface-on tilted angle

Figure 2.5 Three irradiation geometries used for tailing experiments. The lines to the right of each figure illustrate the expected distribution of interaction depths for each geometry.

2.3.1 Simulating CZT Detector Response

- **Simulation theory**

To characterize low energy tailing in the CZT detector we measured monoenergetic isotope sources and compared the results to simulations. We considered the differential pulse height distribution where each photon interaction results in a pulse. The differential number of pulses, dN, is recorded within an energy increment, dE, determined by the amplitude of the pulse. To simulate the energy spectrum, the number of photons that interacted in small increments in the detector depth, dz, and the amplitude of the signal that these interactions created was determined. Equation (2.3) shows how the differential pulse height dN/dE was determined from the product of dN/dz and dz/dE.

$$\frac{dN}{dE} = \frac{dN}{dz}\frac{dz}{dE} \tag{2.3}$$

The term dz/dE was found by solving for the inverse of equation (2.2) and differentiating z(E). This was done numerically using Origin 7.0 graphing software because E(z) is a multi-valued expression; the process can be found in Appendix A. The function N(z) depends on the geometry of the incident photon beam with respect to the detector. Three different geometries were investigated, as mentioned above; edge-on, surface-on, and tilted angle. For edge-on irradiation the number of interactions within a given thickness of the detector is a linear function of detector depth, z, since we assume that the planar length of the detector is sufficiently long to absorb all photons. In this case, $N(z) = N_0 z/L$, where N_0 is the total number of incident photons at the edge of the detector and L is the thickness of the detector. For surface-on irradiation, the exponential relationship given by equation 2.4 describes the number of photons that interact within a given depth. Similarly, for tilted angle irradiation the same expression can be used with the addition of a sin(α) term to account for the angle, α, between the photon beam and the detector surface; that is, the path traveled by incident photons through the detector is $z/\sin(\alpha)$, as shown in Figure 2.3. The differential of the photon attenuation density expression for each geometry is given by

$$\frac{dN}{dz} = \begin{cases} N_0/L, & \text{edge-on} \\ \mu N_0 e^{-\mu z}, & \text{surface-on} \\ \mu N_0 e^{-\mu z/\sin\alpha}, & \text{tilted angle} \end{cases} \tag{2.4}$$

Once the product of dN/dz and dz/dE was determined, the resulting spectrum was convolved with a Gaussian kernel to represent statistical fluctuations in the number of charge carriers as well as electronic noise. The spectrum due to broadening, $\left(\frac{dN}{dE}\right)_b$, was calculated from the theoretical spectrum, $\left(\frac{dN}{dE}\right)_t$, according to

$$\left(\frac{dN}{dE}\right)_b = \int_0^\infty \left(\frac{dN}{dE}\right)_t e^{-(E-t)^2/2\sigma^2}\, dt \tag{2.5}$$

The total standard deviation, σ, was found from the standard deviations due to statistical noise, σ_s, and electronic noise, σ_e, and given by $\sigma = \sqrt{\sigma_s^2 + \sigma_e^2}$. The statistical fluctuation in the number of charge carriers was calculated directly as $\sigma_s = \sqrt{E/w}$, where w is the carrier creation energy. Statistical broadening was inherent to the measurement. Electronic noise resulted from many factors such as output capacitance of the detector and inherent noise in the preamplifier. The electronic noise was determined from the full-width at half maximum due to electronic noise, FWHM_e, and was calculated as $\sigma_e = \mathrm{FWHM}_e/2.35$. The value for FWHM_e was found experimentally by replacing the detector with a pulser with well-defined pulse amplitude.

- **Simulation set-up to compare to experiment**

Parameters in the simulation were set to match experimental parameters. The CZT thickness, L, was 3 mm. The mean free path lengths of charge carriers were 30 and 0.24 mm for electrons and holes, respectively. These values are based on an applied electric field of 100 V/mm, a typical value for CZT detectors and the size of electric field used in our experiments.

Surface-on and tilted angle irradiation were simulated for 20, 40, 60, 80, 100, and 120 keV energies. Tilted angle simulations were done for values of α equal to 15° and 10°. The resulting spectra were compared to surface-on simulations by evaluating peak-to-total ratios of the simulated spectra. The peak energy window was arbitrarily chosen as 10 % of the peak maximum. Higher peak-to-total ratios indicate that more of the measured spectrum was in the full energy peak and less in the low energy tail.

Simulations with the beam incident on the edge of the detector were done to determine the relationship between energy resolution and (a) beam thickness, as well as (b) beam location along the detector edge. Edge-on irradiation was simulated with a 122 keV beam to correspond to experimental measurements done with a ^{57}Co source, which emits gamma rays of 122 keV. A beam was simulated which covered the thickness of the detector, 3 mm. In addition, three more values of beam thickness, 0.375, 0.75, and 1.5 mm, were simulated to determine the relationship between beam thickness and energy resolution. The incident beam was simulated nearest the edge of the cathode electrode for beam width smaller than the detector thickness. A 0.3 mm beam was also simulated as incident along different detector depths to determine the relationship between beam depth and energy resolution. In practice, this means that the value of z in the Hecht formula, equation (2.2), was varied from 0 to 3 mm in increments of 0.3 mm. This was compared to experiments with the same parameters.

2.3.2 Measuring CZT Detector Response

- **Detection system**

Experimental measurements were done using an ORTEC 4001C NIM Bin, ORTEC 660 Dual Bias Supply, ORTEC 926 MCB, ORTEC 590A amplifier, and eV-550 preamplifier. The amplified signal was digitized with an 8000 channel ORTEC TRUMP 8000 Multichannel Analyzer.

A monolithic CZT crystal was purchased from eV-Products and had dimensions of 10x10 mm^2 and 3 mm thickness. Electrodes were fabricated from a thin copper sheet and soldered to a signal wire. They were then positioned on the top and bottom of the CZT surface, shown in Figure 2.6. The electrodes had openings to allow for irradiation of the detector surface without attenuation through the electrodes. The CZT and electrodes were then enclosed in a brass casing to allow transport of the detector in a robust unit. The brass casing had openings that allowed for surface-on, tilted angle and edge-on irradiation of the CZT crystal. The entire setup was duplicated so that two detectors could be used simultaneously to test the integrity of the electric field at the edge of the detector, the exception being that the CZT crystal in the second setup was only 2 mm thick.

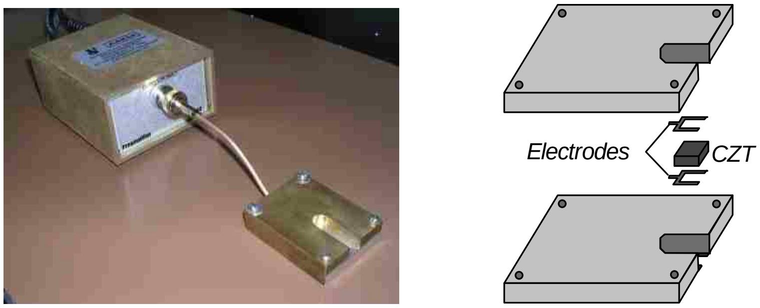

(a) **(b)**

Figure 2.6 CZT detector setup; (a) photo of CZT crystal in brass casing connected to preamplifier and (b) schematic of CZT crystal with electrodes and brass encasement.

- **Radioisotope sources**

Radiation sources ^{241}Am (59 keV) and ^{57}Co (122 keV) were used for irradiation. For edge-on irradiation two different beam diameters were chosen for the ^{57}Co beam. A 3 mm collimated beam was measured to cover the edge of the detector as well as a 0.3 mm collimated beam to scan along the edge of the detector. Surface-on and tilted angle measurements were all done with 1 mm collimated beams. A slab of acrylic with a screw drilled through one end was used to increment sources up or down with respect to the detector. Each quarter turn of the screw corresponded to 0.15 mm displacement of the acrylic slab.

- **Edge-on irradiation**

As stated above, two collimation widths were chosen to perform edge-on measurements of the detector. A 0.3 mm collimated beam was used to scan across the edge of the detector at varying depths and a 3 mm collimated beam was used to cover the thickness of the detector.

- **Edge scanning**

The 0.3 mm collimated ^{57}Co source was scanned along the edge of the detector for several reasons: 1) to measure detector response for a narrow beam at different positions along the edge and compare to simulation, 2) to compare experimental measurements to the Hecht formalism in equation (2.2) to determine mean free path length of holes and electrons and compare to accepted values in literature, and 3) to check for integrity of measured response at the edge of detector (electric field uniformity).

The 0.3 mm beam was positioned so that the full beam was incident at the cathode edge of the detector, meaning the center of the beam is positioned at 0.15 mm below the surface, as shown in Figure 2.7 (a). A measurement was taken here and then the beam was stepped down by an increment of 0.3 mm by turning the screw in the acrylic slab half a turn. The measurement was repeated to span the entire thickness of the CZT crystal. The response of the detector at each beam position was compared to simulation. For each measurement the total number of counts under the energy peak was found and plot with respect to depth. The amplitude of the signal was also plotted according to depth and compared to equation (2.2) to evaluate mean free path lengths of electrons and holes used for simulations.

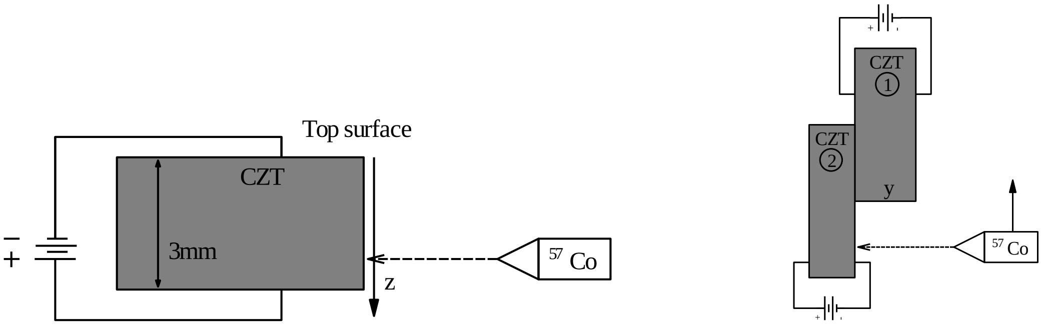

(a) (b)

Figure 2.7 (a) Schematic of edge-scan setup. The edge-scan method measures the dependence of signal amplitude on interaction depth. (b) Schematic of setup used to test electric field at detector edge.

The edge of the detector may experience non-uniform electric field that would affect the results of the experiments just mentioned. To test this, the 0.3 mm beam was scanned across the surface of the detector at the detector edge in steps of 0.15 mm, shown in Figure 2.7 (b) as CZT-1. The second CZT detector, labeled CZT-2, was positioned behind the first to determine where the edge of CZT-1 was located. The total number of counts at each position was recorded and plotted with respect to position. We expected to see an immediate increase in counts from CZT-2 when there was a corresponding decrease in counts in CZT-1 if there was no dead region in CZT-1.

- **Edge broad beam**

The ^{57}Co source was used with 3 mm collimation and covered the thickness of the detector. The result was compared to simulation to measure low energy tailing with the detector edge completely illuminated.

- **Surface-on and Tilted angle irradiation**

Surface-on and tilted angle measurements were done using a 1 mm collimated beam. Tilt angles used were 15º and 10º. Both ^{241}Am and ^{57}Co sources were measured. The results were compared to simulations and peak-to-total ratios were determined in each case.

2.3.3 Results of Simulations and Measurements

- **Edge-on results**

Figure 2.8 (a) shows experimental results of narrow beam scanning along the edge of the detector. The measurement near the cathode (top) surface shows a relatively narrow full

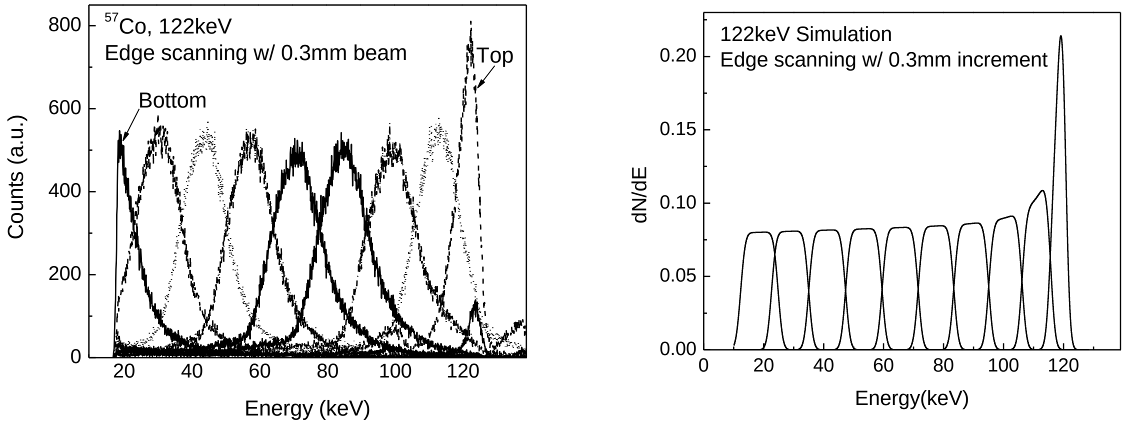

(a) **(b)**

Figure 2.8 (a) Energy spectrum results of edge scanning with 0.3 mm steps of the 122 keV radiation beam with 0.3 mm thickness and (b) results of simulations with matched parameters.

energy peak with the correct signal amplitude, 122 keV for the ^{57}Co source. As the beam was moved toward the anode the response broadened and shifted to lower amplitudes. Simulation done with the same parameters as the experiment is shown in Figure 2.8 (b).

The signal intensity profile for the measurements shown in Figure 2.8 (a) is shown in Figure 2.9 (a). The peak energy versus depth is plotted in Figure 2.9 (b) and compared to equation (2.2) using mean free path lengths for electrons and holes of 25 mm and 0.33 mm, respectively.

The two detector intensity profiles measured to determine the integrity of the CZT edge are shown together in Figure 2.10. As the beam approached the edge of CZT-1 the number of counts detected increased synchronously with the decrease in total counts measured by CZT-2.

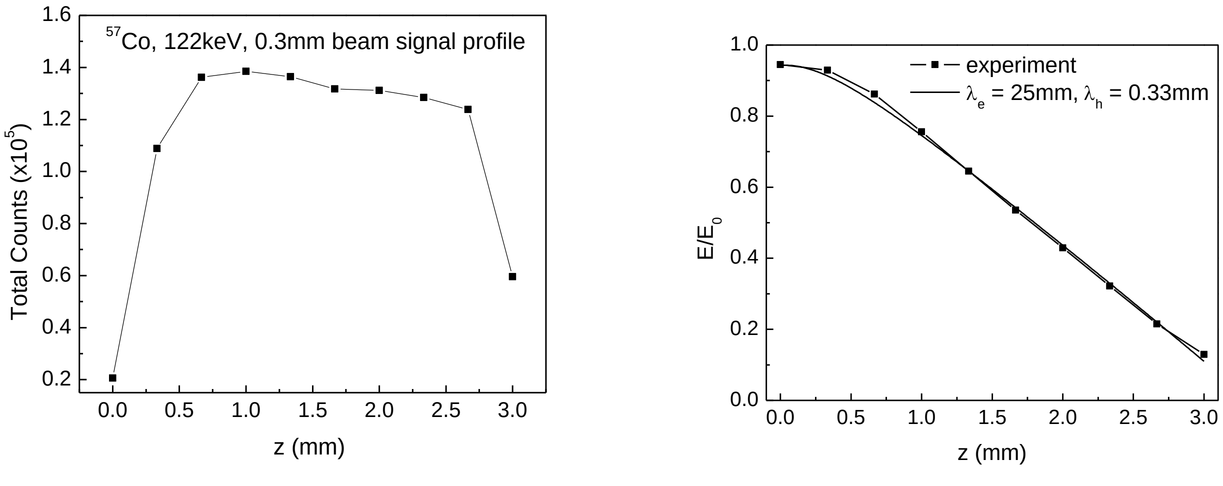

(a) (b)

Figure 2.9 (a) Signal intensity profile of edge-scan with 122 keV beam of 0.3 mm collimation. (b) Peak energy with respect to beam position along with Hecht curve fit assuming electron and hole mean free path lengths of 25 mm and 0.33 mm, respectively.

This indicated that any dead region at the edge of CZT-1 was very small, at least smaller than the 0.3 mm thickness of the beam. If this were not the case, counts measured by CZT-2 would have decreased as the beam was attenuated by CZT-1, but counts measured by CZT-1 would not have increased right away.

The result of edge-on irradiation of the detector with a wide beam covering the detector thickness is shown in Figure 2.11 (a) along with simulation with the same parameters. It was evident that a significant amount of tailing resulted from irradiation of the detector over its entire thickness. Simulation of varying beam widths is shown in Figure 2.11 (b). The results showed that a FWHM of less than 10 keV can be obtained for a beam width less than 0.375 mm, which should be sufficient for energy-resolved x-ray and CT imaging using a polychromatic x-ray beam [2, 3, 17].

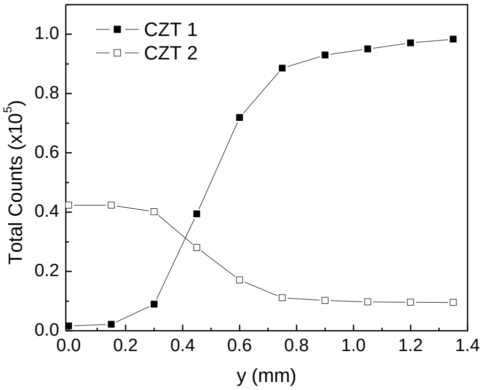

Figure 2.10 Results of edge test experiment. Two CZTs are stacked (see Figure 2.7) to investigate whether dead regions exist along the edge of the CZT crystal.

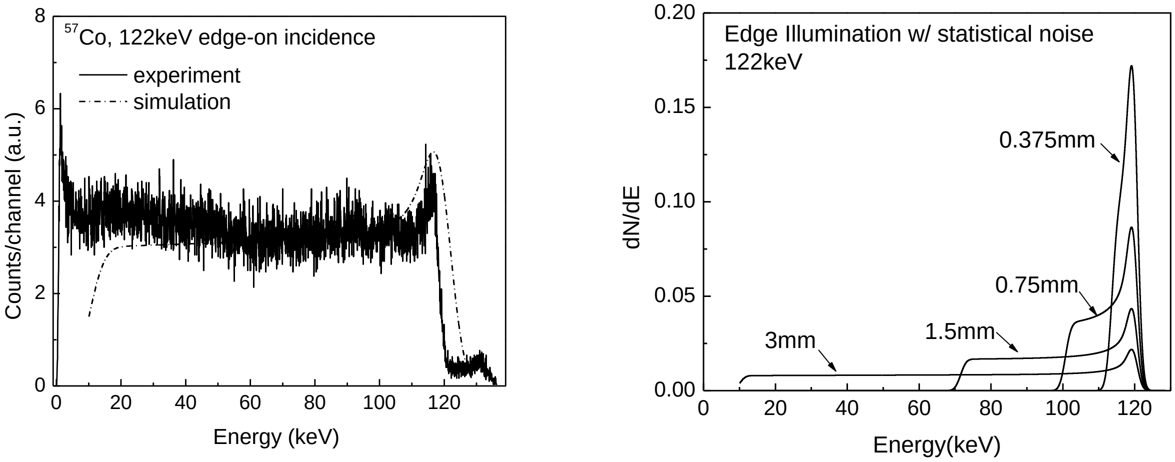

(a) **(b)**

Figure 2.11 (a) Experimental and theoretical energy spectra with edge-on irradiation of 122 keV beam with 3 mm thickness. (b) Simulated energy spectra with 122 keV beams for thicknesses of 0.375 – 3 mm incident on the edge of the CZT; broadening due to statistical fluctuations of the charge carriers was incorporated.

- **Surface-on and tilted angle results**

Figure 2.12 shows simulated spectra for surface-on and tilted angle irradiation for six different energies ranging from 20 – 120 keV with 20 keV step size. The results showed the gradual increase in tailing as energy increased and as tilt angle increased. Tailing was relatively small for energies below 60 keV for all tilt angles. For surface-on tailing was severe for energies above 60 keV but was reduced for small tilt angles of 15° and 10°. Peak-to-total ratios were determined for each energy and tilt angle (Table 2.2).

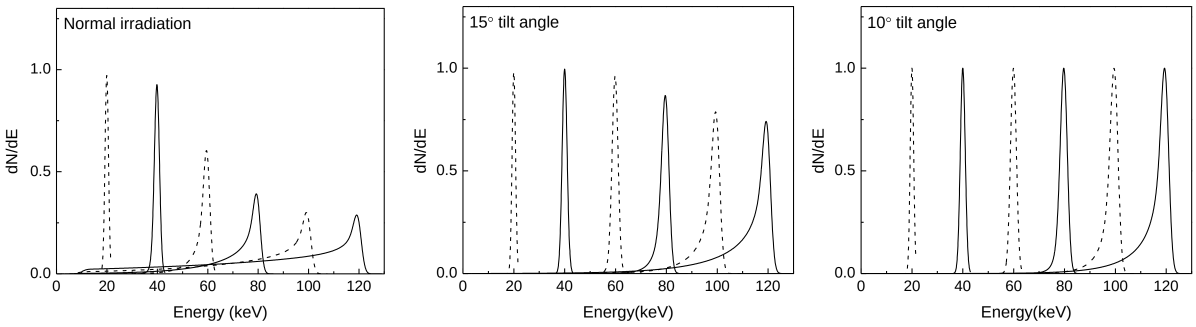

(a) **(b)** **(c)**

Figure 2.12 Simulated energy spectra of 20-120 keV energies for (a) surface-on and tilted angle incidence with (b) 15° and(c) 10° tilt angles. The total number of the photons was kept constant in each case.

Figure 2.13 shows results of simulation compared with experiment for ^{241}Am and ^{57}Co under (a) normal, (b) 15°, and (c) 10° incidence. Experimental measurements were for the beam collimated to 1 mm. Both simulation and experiment showed a decrease in tailing for low tilting angles. Peak-to-total ratios are given for all data sets in Table 2.3**.** The improvement in peak-to-total ratio for tilted angle compared to surface-on irradiation was clear in both experiment and theory for each isotope studied. However, notice in the tilted angle measurements (Figure 2.13 (b) and (c)) the pronounced escape peaks located 23.5 and 27.5 keV below the full energy peak. These escape peaks were due to the escape of characteristic K x-rays from Cd and Te atoms, respectively, in the CZT. The effect of K x-ray escape when using tilted angle configuration will be discussed in the next chapter.

2.4 Conclusions and Considerations for Tilted Angle Geometry

Both edge-on irradiation with a narrow beam and tilted angle irradiation with a narrow beam exhibited good energy resolution compared to surface-on irradiation. However, with edge-on irradiation with a narrow beam, charge build-up can occur because charge is being generated in a small region of the detector. There are several benefits to tilted angle geometry including (1) increased energy resolution, as discussed above, (2) potentially thinner detector to decrease charge diffusion, and (3) smearing of charge throughout detector volume to prevent charge build-up. Titled angle irradiation is done with a linear array of strip pixels, as opposed to the two-dimensional array of square pixels traditionally used in x-ray and CT imaging. It was noted previously that a linear array of strip pixels can be used in scanning slit image acquisition geometry which allows for efficient scatter rejection.

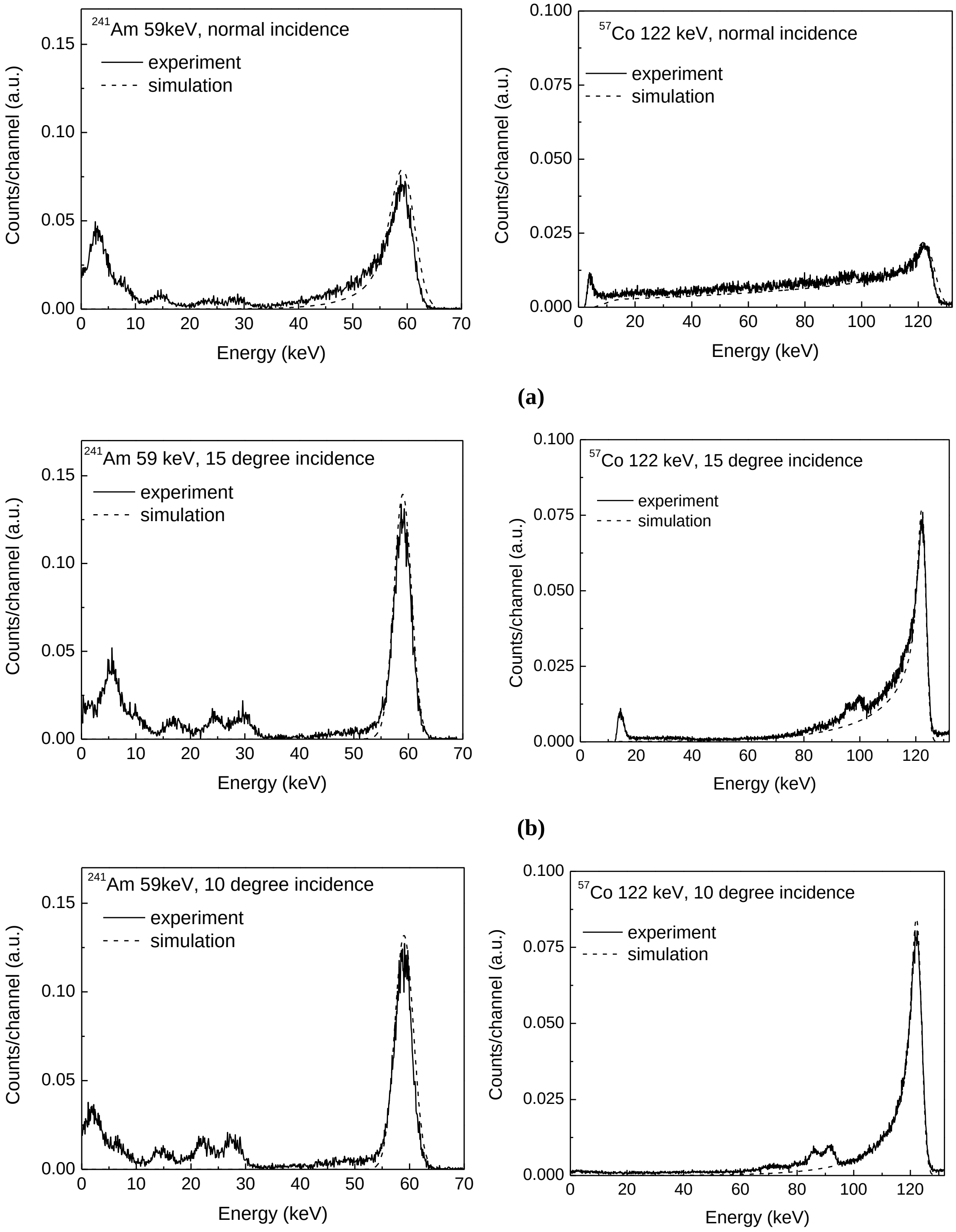

(a)

(b)

(c)

Figure 2.13 Energy spectra of the 59 keV (left) and 122 keV (right) radiation beams with (a) surface-on incidence and with tilted angle incidence at (b) 15° and (c) 10° tilt angles. Both experimental and simulated spectra are presented.

Table 2.2 Peak-total ratios (%): simulations

Tilt angle	90°	15°	10°
Energy (keV)			
20	96	96	98
40	93	96	98
60	65	95	98
80	57	87	94
100	35	77	88
120	34	71	84

Table 2.3 Peak-to-total ratios (%): experiment vs theory

Tilt angle	90°	15°	10°
122 keV Theory	38	75	83
122 keV Experiment	29	67	69
59 keV Theory	73	96	97
59 keV Experiment	60	85	85

2.4.1 Reduced Charged Diffusion in a Thin Detector

The thickness of CZT detectors is typically several millimeters to ensure total attenuation of photons of energies used in diagnostic applications, up to 140 keV. For tilted angle configuration this thickness may be decreased without suffering transmission of higher energy photons, as seen in Figure 2.14. A thinner crystal results in less lateral diffusion of charge as it moves through the detector. For a multi-pixel detector this improves spatial resolution, since charge is less likely to be shared between pixels for a single interaction. Energy resolution is also improved for the same reason.

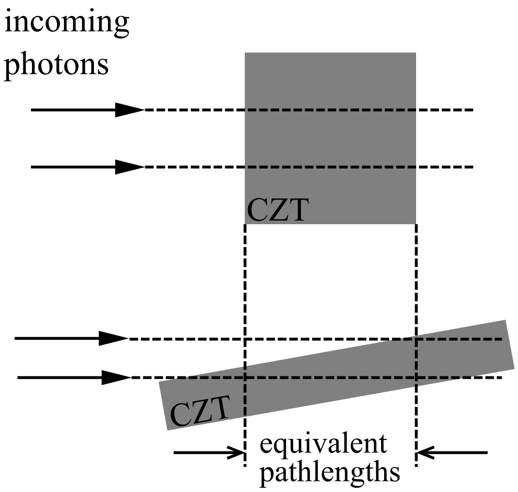

Figure 2.14 For tilted angle irradiation the thickness of the CZT crystal may be decreased without sacrificing detection efficiency.

The amount of lateral diffusion depends on the thickness and applied electric field in the detector [14, 17, 19]. According to [19], for a 1 mm thick detector and an applied field of 100 V/mm, typical of CZT detectors, the approximate spread of charge due to lateral diffusion is 23 μm root mean square (RMS).

The FWHM of the spread is related to the RMS as FWHM = 2.35xRMS. This means that for the 3 mm thick detector used in this study the FWHM of the lateral charge diffusion is approximately 162 μm. This spread is significant for many x-ray imaging modalities because the typical pixel size is less than 1 mm. However, a 1 mm thick detector used with a 10° tilted angle has sufficient thickness to maintain detection efficiency and results in lateral diffusion with FWHM of only 54 μm. This decrease in lateral diffusion should significantly improve spatial and energy resolution (full energy collection and no double counting) compared to a thicker detector.

2.4.2 Count Rate in Tilted Angle Geometry

Maximum count rate requirements depend on the number of photons needed per pixel to achieve sufficient SNR within the required scan time. It has been calculated that for breast CT the count rate of the detection system should be 2 million counts per pixel per second [2]. The count rate is limited by the CZT crystal itself due to charge build up. As holes are trapped in the detector volume they create local space charge and polarize the detector. Count rate is also limited by the collection time required for charge to drift through the detector and induce a signal. The detector needs time to stabilize between events which increases acquisition time and increases the possibility of image blurring due to patient motion.

The advantage of tilted angle geometry with respect to count rate is two-fold. First, charge is created throughout the detector volume instead of localized in a small region as it is for surface-on and edge-on irradiation. Second, it allows for the possibility of thinner crystals which decreases the collection time of charge drifting through the detector. This shortens the pulse width and reduces pulse pile-up.

2.4.3 Increased Characteristic X-ray Escape

As noted previously, increasing interactions near the detector surface using tilted angle geometry will also increase the likelihood of characteristic x-ray escape. This can cause significant problems for energy and spatial resolution, especially for a polychromatic x-ray beam. Low energy photons overlap with the escape peaks from higher energies and a low energy threshold cannot be set without decreasing detection efficiency. However, unlike hole trapping which depends on many variables, characteristic escape is statistically predictable. The next chapter describes simulations done to account for K x-ray escape in a CZT detector.

3 INVESTIGATION OF CHARACTERISTIC X-RAY ESCAPE

Energy discrimination in a CZT detector can be severely hampered by the escape of characteristic x-rays. X-rays may escape back from the detector surface, a phenomenon which is more pronounced for tilted angle irradiation where most interactions take place near the detector surface (Figure 3.1).

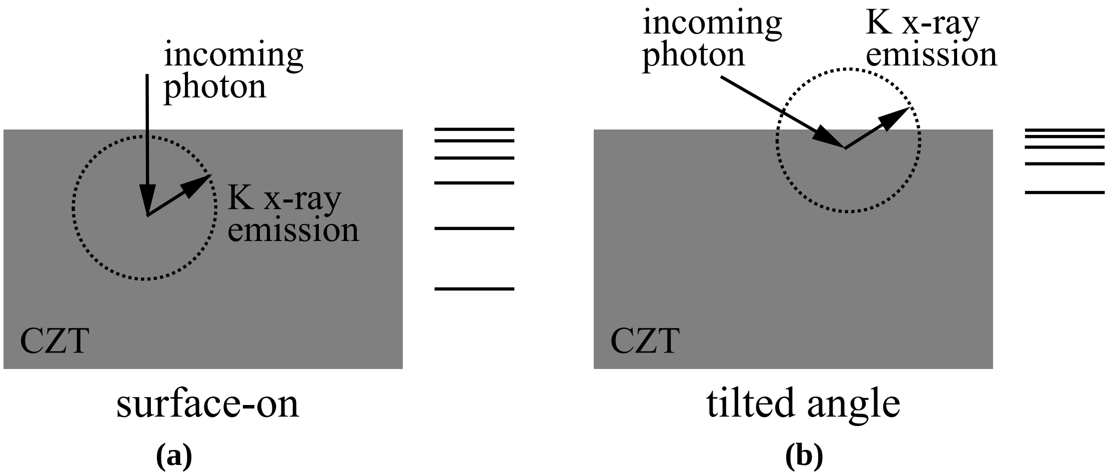

Figure 3.1 Comparison of likelihood of K x-ray escape for different irradiation geometries, with photon interaction profiles shown to the right of each geometry. For (a) surface-on irradiation photon attenuation occurs throughout the thickness of the detector while for (b) tilted angle irradiation interactions are more likely near the detector surface, increasing K x-ray escape.

The effect of characteristic escape on the energy spectrum is demonstrated in Figure 3.2. The position of the escape peaks correspond to the energy carried out of the pixel by the characteristic x-rays shifted from the full energy peak. For a multi-pixel imaging detector, the escape of characteristic x-rays from the sides of the pixel decreases spatial resolution when escape x-rays interact in neighboring pixels because multiple pixels record signal for a single interaction. Fortunately, the likelihood of characteristic x-ray escape is predictable, that is, the x-rays are monoenergetic and therefore the mean attenuation lengths are known. This enables the prediction of escape based on the depth at which the initial interaction takes place.

3.1 Charge Sharing in CZT and Other Materials

Both characteristic x-ray escape and diffusion of the charge cloud create what is known as charge sharing. Charge sharing has been extensively studied for semiconductor detectors. Edge-on irradiation of Si strip detectors has been investigated for mammography applications [31]. Charge sharing in Si and GaAs detectors for dental x-ray sources has also been studied [32-34]. CZT and CdTe detectors have been investigated as well [35-40]. We investigated characteristic x-ray escape for several pixel sizes in both square and strip pixel configuration [26]. Simulations were carried out using Monte Carlo methods and compared to experimental results with a square pixel CZT detector.

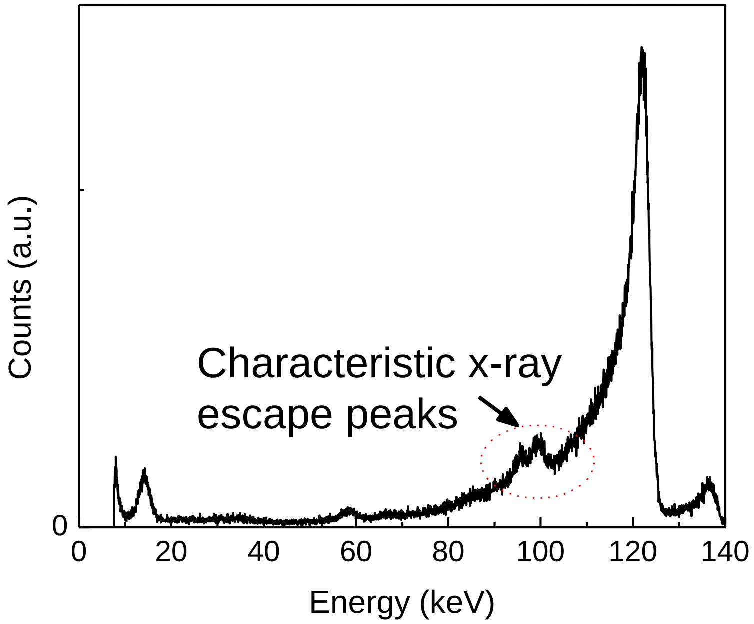

Figure 3.2 Representative energy spectrum with prominent characteristic x-ray escape peaks. For CZT, these peaks are due mainly to K escape from Cd and Te atoms.

3.2 Simulating Energy Escape from a CZT Detector Pixel

Pixel sizes chosen for simulation included those typically found in the clinic. Pixels of 1 mm size are usually used for applications such whole body CT [1], while a smaller pixel size of 0.4 mm is used in dedicated breast CT [19]. Projection radiography, such as that used for chest x-rays, has a typical pixel size of 0.1 mm [1].

Square and strip pixels were simulated for this study. Strip pixels have the advantage of tilted angle irradiation so simulations were done for 90°, 15°, and 10° incidence angles. The widths of the strips simulated match the dimensions of the square pixels.

The experimental CZT detector was capable of discriminating energy into five energy bins. Therefore, five different energies of primary photons were simulated corresponding to five energy bins. The bins ranged in energy from 20 to 120 keV with 20 keV widths and the average energy of each bin corresponded to values of 30, 50, 70, 90, and 110 keV.

3.2.1 X-ray Interaction in CZT Detectors

To simulate x-ray escape from interactions in the CZT detector, several assumptions were made. We assumed that the main interaction of the primary photon was by photoelectric effect and the major effect of energy resolution deterioration was due to the escape of K x-rays. This meant that we ignored effects such as Compton and Rayleigh scatter, as well as the possible escape of L x-rays and Auger, Compton, and photoelectrons. We also ignored charge cloud diffusion. The next several sections will justify the assumptions that were made to simulate charge loss from a detector pixel for imaging and spectroscopy applications. In the text, the term 'signaling pixel' will refer to the pixel in which the incident photon interacts.

- **Photon Interactions**

Diagnostic x-ray imaging typically uses x-rays within the energy range of 20 to 120 keV. Three types of x-ray interactions may occur at these energies: Rayleigh scatter, Compton scatter, and the photoelectric effect. We simulated only the photoelectric effect because it is the most probable interaction as illustrated in Figure 3.3 (a). For a 120 kVp x-ray beam the average energy is 60 keV and at this energy the relative photoelectric effect is 94 % compared to 2 % and 4 % for Compton and Rayleigh scatter, respectively. Therefore we considered only the photoelectric effect for our simulations. The photoelectric effect has the advantage of being the easiest interaction to simulate since the photon is completely absorbed and does not interact multiple times.

If an incident photon scatters out of a pixel due to Rayleigh scatter and interacts with a neighboring pixel, the spatial resolution is affected but not the energy resolution, because the photon does not lose energy in this type of interaction. When Compton scatter occurs, the incident photon may deposit some energy in one pixel with the scattered photon possibly interacting in another pixel, distorting both spatial and energy resolution. Compton scatter is very complicated to simulate because of the range of energies and angles that may be taken by the scattered photon. The photoelectric effect results in complete absorption of the incident photon, however, spatial and energy blurring between pixels occurs due to escape of characteristic x-rays from the signaling pixel. Unlike Compton scatter, these x-rays have discrete energies and are emitted isotropically from the atom and therefore have behavior that is easier to predict.

- **K and L x-rays and Auger electrons**

For the CZT detector that was simulated, the escape of characteristic x-rays from Cd and Te atoms are of concern, while escape x-rays from Zn represent less of an issue. This is because the weight fraction of Zn is relatively small, 5% compared to 45% and 50% for Cd and Te, respectively [27]. Photoelectric interactions with Cd and Te atoms will occur at the K-, L- and M-shells, however, the probability is highest at the K shell, 80%. L x-rays from Cd and Te have low energy, about 3 and 4 keV, respectively, so local reabsorption is highly likely. K x-rays on the other hand have sufficient energy to travel far enough to leave the signaling pixel; Cd K x-rays have an average energy of 23.4 keV (116 μm attenuation length) while those from Te have an average energy of 27.5 keV (64 μm attenuation length). Therefore we considered K x-rays while neglecting L x-ray escape. Properties of the K-edges of Cd and Te are listed in Figure 3.3 (b) which shows the attenuation coefficients of CZT with respect to energy in the diagnostic range.

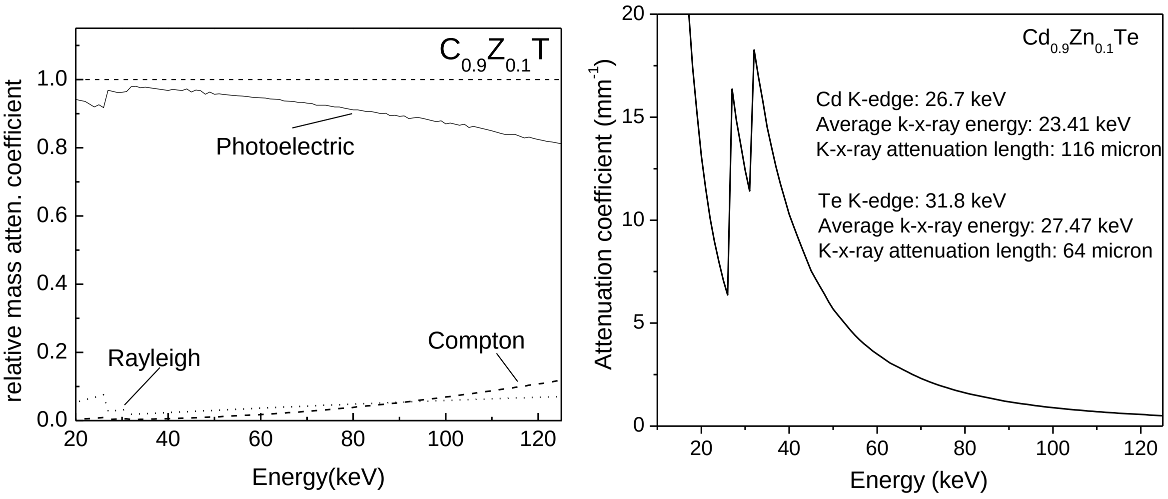

(a) **(b)**

Figure 3.3 (a) Photoelectric effect, Rayleigh and Compton scatter fractions of x-rays in CZT. Rayleigh and Compton scatter components are 7 % and 10 % , respectively, at the highest energy of 120 keV. At an average energy of 60 keV these components are decreased to 4 % and 2 %, respectively. (b) Linear attenuation coefficient of x-rays in CZT material. Data values taken from [41].

Of the interactions at the K shell, 87% result in the emission of K x-rays while the remaining emissions yield low energy Auger electrons [42]. In total, 70% of photoelectric interactions in CZT result in the emission of K x-rays from either Cd or Te. In addition, the probability of interaction with either atom can be determined with respect to the energy of the incident photon.

- **Photoelectrons from K x-ray interactions, CSDA**

For the purpose of our simulations we also assumed the photoelectrons resulting from the photoelectric interactions were absorbed locally, within the signaling pixel. When a photoelectric interaction takes place at the K shell of an atom, the photoelectron that is emitted has kinetic energy equal to the difference between the K-edge energy and the energy of the incident photon. If we consider the maximum energy of a photon from a 120 kVp beam the photoelectrons from the K shells of Cd and Te can have a range of energies between 0 and 93 keV. The range of photoelectrons in CZT with respect to their energy is shown in Figure 3.4 using data taken from the NIST ESTAR database [43]. The continuous slowing down approximation (CSDA) is determined as the integral of the inverse of the stopping power with respect to energy, where the stopping power is the energy lost per unit distance. The electron takes a tortuous path as it travels and therefore a better measure of the distance the electron traveled from its initial position is the projected range. The ratio of projected range to CSDA is called the detour factor and is approximately 0.67. Therefore the maximum range of the photoelectrons from incident photons in the diagnostic energy range is approximately 26 μm (corresponding to 93 keV), much shorter than the range of K x-rays from Cd or Te. The range at the average energy of 60 keV for a 120 kVp beam is even shorter, on the order of 13 μm. Thus the projected range of photoelectrons is small compared to the attenuation lengths of the K x-rays emitted; it follows that the range of Auger electrons will be small as well.

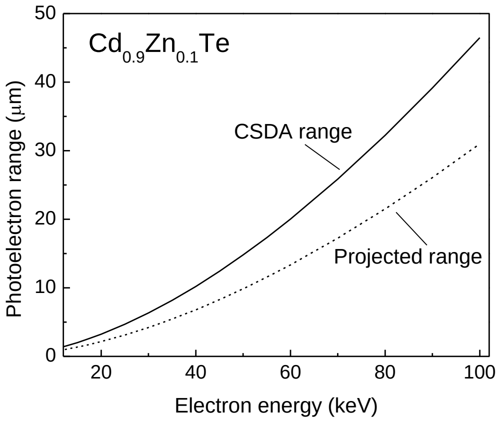

Figure 3.4 Continuous Slowing Down Approximation (CSDA) and projected range of electrons in CZT with respect to energy. Photoelectric interactions with the K shell of Cd and Te atoms can emit photoelectrons with energy in the range of 0 to 93 keV. Their projected range is small compared to the attenuation lengths of the K x-rays emitted.

- **Possibilities of K x-ray behavior**

We considered six possible types of K x-ray behavior, shown in Figure 3.5 (a). The only behavior which results in correct recording of the incident photon is complete absorption of both the incident photon and K x-ray in the same pixel. The second possibility is back escape of the K x-ray from the incident surface of the pixel. The third is forward escape from the back surface of the pixel. The fourth is side escape to a neighboring pixel, and similarly the fifth is reception of a K x-ray from a neighboring pixel in the pixel under consideration. The sixth is the escape of the K x-ray from the outside edge of the detector. The second through sixth behaviors result in deterioration of energy resolution while, in addition, the fourth and fifth behaviors distort spatial resolution.

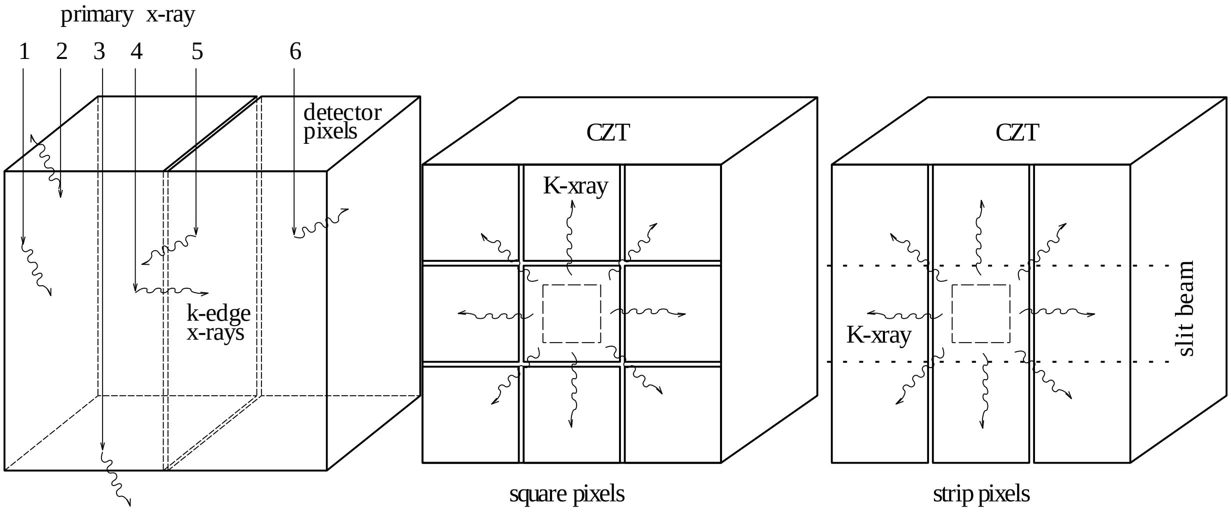

(a) (b) (c)

Figure 3.5 (a) Processes involved in x-ray interactions with detector material: 1 – complete absorption of the photoelectron and K x-ray, 2,3 – back and forward escapes of characteristic radiation, 4,5 – side escapes, 6 – side escape outside of the pixels. Schematics of characteristic x-ray crosstalk for (b) pixel, in which all escape corresponds to type-4 interaction and (c) strip detectors, in which reabsorption within the strip corresponds to type-1 behavior.

- **Comparison of energy and spatial resolution for square and strip pixels**

The behavior of K x-rays will affect energy and spatial resolution differently depending on the pixel configuration in the detector. We simulated both square and strip pixels and the different configurations are shown in Figure 3.5 (b) and (c). It is clear from Figure 3.5 (c) that for the strip pixel configuration, a greater percentage of escape x-rays will interact in a single neighboring pixel than for the square pixel configuration. This increases spatial blurring between pixels, however, the resolution in the other direction (along the pixel strip) is dependent on the width of the beam and can be varied. The advantage of strip pixels is that the detector can be irradiated at a small angle between the beam and detector. This increases back escape from the pixel, with a proportional decrease in escape to neighboring pixels. It is much easier to correct for escape that has left the detector than escape that is shared between pixels because there is no double counting of a single photon. The other advantage is that escape that would occur along the strip pixel length is absorbed in the strip pixel, whereas it would escape in square pixel configuration, so that energy resolution is not as degraded for strip pixel configuration.

3.2.2 Simulation Study

The simulation code was written using Interactive Data Language (IDL, ITT Visual Information Solutions, Boulder, CO) and can be found in Appendix B. The detector model and beam orientations are shown in Figure 3.6.

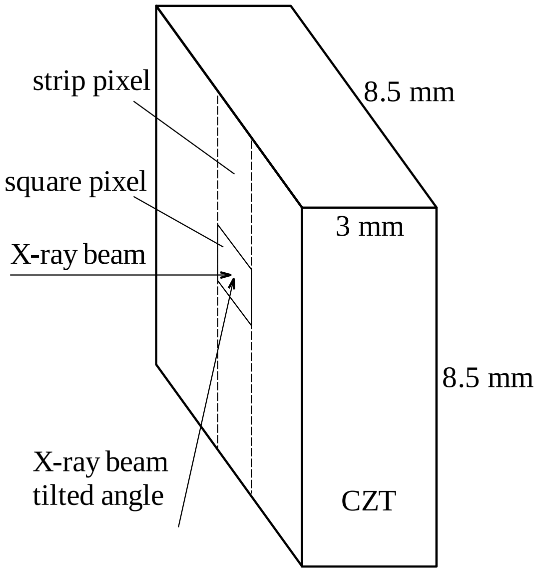

Figure 3.6 Schematic of the CZT detector model and beam orientation. Relative geometry of square and strip pixels are shown; the tilted angle x-ray beam was done only for strip pixels.

- **Detector setup**

The thickness of the CZT detector was 3 mm corresponding to the thickness used for experimental imaging detectors. The sides of the detector were 8.5 x 8.5 mm^2, a sufficient length so that escape in this direction was insignificant. Square pixels of side lengths 1, 0.4, 0.2, and 0.1 mm were simulated as well as strip pixels of length 8.5 mm and widths to match those simulated with square pixels. The sizes were chosen to correspond to pixel sizes found in the clinical setting as described previously.

- **Incident Beam**

The x-ray beam was simulated for three different cases. First, the beam was incident on a square pixel in the center of the detector while neighboring pixels were not irradiated. This was done to determine charge lost from the central pixel due to x-ray escape. Second, the beam was incident on all neighboring pixels while the central pixel was not irradiated to simulate charge received due only to x-ray escape from neighboring pixels. Third, the beam was incident on a central strip pixel while neighboring strips were not irradiated. This last configuration was done with the beam incident at 90°, 15°, and 10° with respect to the pixel surface.

The beam was allowed to have one of five energies chosen corresponding to the average energy in each energy bin for a 120 kVp beam that was split into five energy ranges. The simulated bins had a width of 20 keV and ranged from 20 to 120 keV: 20 – 40, 40 – 60, 60 – 80, 80 – 100, and 100 – 120 keV. These bins corresponded to those used in experimental measurements as will be discussed later. For each energy, 20 million incident photons were sampled.

- **Geometry and flow chart of simulation**

A detailed geometry of the simulation is shown in Figure 3.7, as well as the simulation flowchart in Figure 3.8. The primary photon was incident with energy E0 and traveled a distance

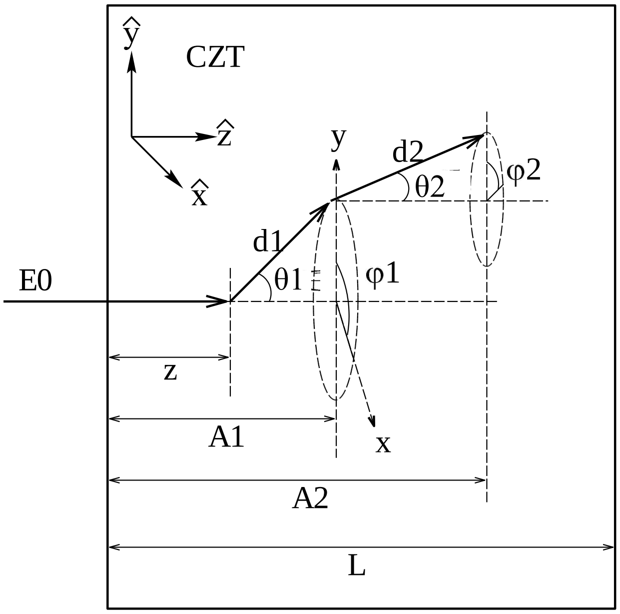

E0	primary photon energy
L	detector thickness
z	depth of interaction of primary photon
d1, d2	distance travelled by K x-ray from Te, Cd
θ1, θ2	polar angle of path taken by K x-ray from Te, Cd
A1, A2	depth of interaction of K x-ray from Te, Cd
φ1, φ2	azimuthal angle of path taken by K x-ray from Te, Cd

Figure 3.7 Geometry of primary photon (E0) and K x-rays from Te (d1) and Cd (d2) tracking simulation.

z before interacting via the photoelectric effect. The value of z was randomly sampled based on the exponential attenuation of photons through a material. The relationship between interaction depth, z, attenuation length, t, and the probability of transmission, I/I_0, was

$$\frac{I}{I_0} = e^{-z/t(E0)} \tag{3.1}$$

The attenuation length was the inverse of the linear attenuation coefficient. The attenuation length for each E0 was determined from NIST data [41]. The value of the ratio I/I_0 was randomly sampled between 0 and 1; z was calculated by

$$z = -t(E_0) \times \ln I/I_0 = -t(E_0) \times \ln R_z \tag{3.2}$$

where *R* was the random number. The relationship is shown schematically in Figure 3.9.

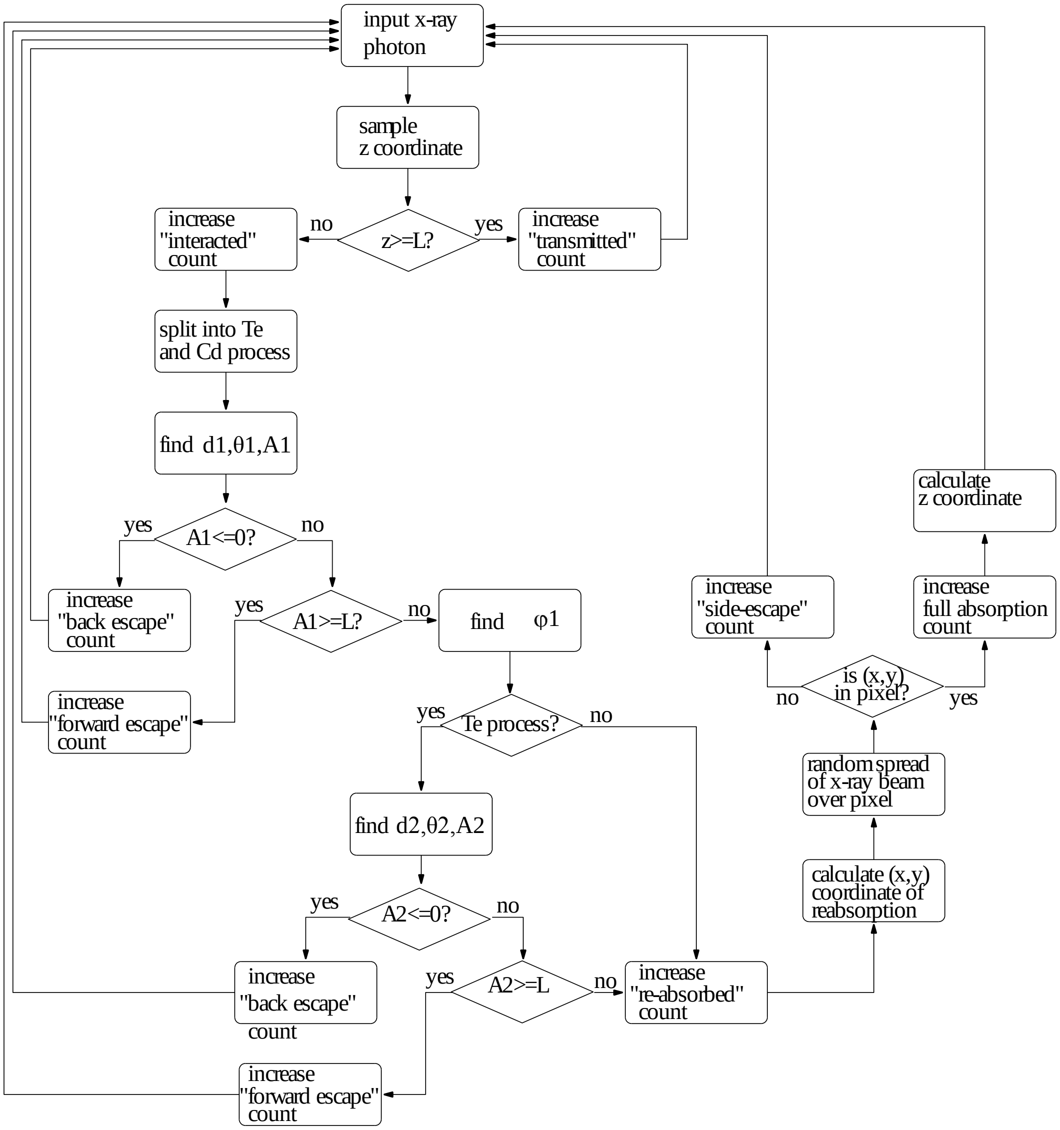

Figure 3.8 Flow chart of the Monte Carlo simulations for tracking characteristic x-rays in CZT detector.

If the value of z was greater than the detector thickness, L, the program increased a counter called “transmitted” by one and went to the next primary photon. Otherwise, the program recorded the interaction depth in a depth profile array. It then determined whether the interaction took place with Te or Cd by comparing a random number between 0 and 1 with the probability of interaction with Te. The probability was determined by the value of E0. If the random number is less than the probability, the interaction was considered to be with Te and a K x-ray from Te was tracked. If the Te K x-ray did not escape the detector, the subsequent Cd K x-ray was tracked. If the initial interaction was not with Te, the program immediately began tracking the K x-ray from Cd.

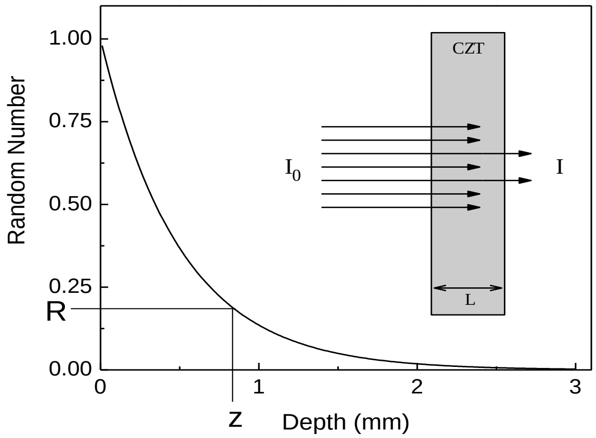

Figure 3.9 Generation of depth of interaction values, z, using a random number between 0 and 1 and the exponential relationship between depth and attenuation. Solving for z will give, $z = -t(E) \times \ln R$, where t(E) is the attenuation length of photons with energy E and $R = I/I_0$.

The tracking of the K x-ray consisted of determining three values: 1) the distance from the interaction that the K x-ray was re-absorbed, 2) the polar angle θ of its trajectory with respect to the z-axis, and 3) the azimuthal angle φ for the rotation of the trajectory in the x,y-plane. The distance of reabsorption from the interaction point was determined based on exponential attenuation in the same way that z was found for the primary photon. The emission of characteristic x-rays was isotropic from the point of initial interaction. The projection of the trajectory along the z-axis was needed to determine whether or not the K x-ray escaped the detector in the back or forward direction. Therefore, the cosine of the polar angle was found and was chosen randomly from

$$\cos\theta = 2 \times R_\theta - 1 \tag{3.3}$$

by sampling random numbers between -1 and 1. The projection along the z-axis was given by

$$d = z \times \cos\theta \tag{3.4}$$

where d was the distance from the initial photoelectric interaction to the final K x-ray interaction.

The azimuthal angle was found to determine displacement of the position of K x-ray interaction from the center of the detector. This indicated whether the K x-ray interacted in a neighboring pixel or escaped from the side of the detector. To do this, the trajectory of the K x-ray was projected onto the x,y-plane according to

$$r = d \times \sin\theta = d \times \sqrt{1 - \cos^2\theta} \tag{3.5}$$

This projection was rotated randomly about the z-axis according to

$$\begin{aligned} x &= r \times \cos\varphi = r \times \cos\left(360 \times R_\varphi\right) \\ y &= r \times \sin\varphi = r \times \sin\left(360 \times R_\varphi\right) \end{aligned} \tag{3.6}$$

where the azimuthal angle took any random number between 0 and 360. The geometry is shown in Figure 3.10.

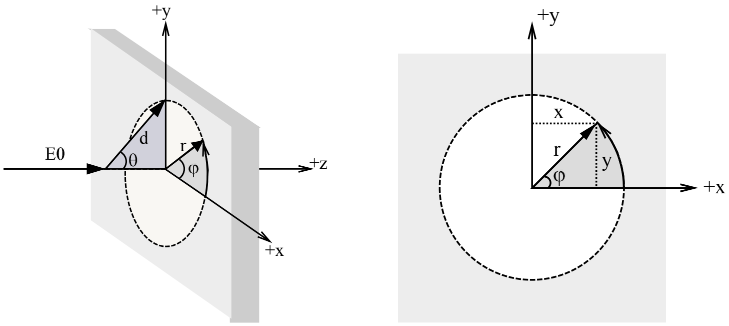

(a) **(b)**

Figure 3.10 Geometry of the method used to determine K x-ray reabsorption position in the x,y-plane. (a) The side view is shown to demonstrate the value of r as determined from θ and d; (b) the view of the x,y-plane is shown to demonstrate determining the x- and y-coordinates of the K x-ray reabsorption position.

Once the final reabsorption position was known, it was then determined whether the K x-ray has escaped the detector by back, forward, or lateral escape by comparing its reabsorption position to the dimensions of the detector. If the K x-ray was reabsorbed, the program then considered the geometry of the initial beam. The distance of the final interaction from the center of the detector (u, v) is determined in the x,y-plane from

$$u = x_0 + x$$
$$v = y_0 + y \tag{3.7}$$

where (x_0, y_0) is the center of the detector in the x,y-plane. This creates a pencil beam incident on the center of the detector. To spread the beam across a pixel of dimensions $(M \times N)$, random values about the center of the pixel are chosen as expressed in

$$dx = -\frac{M}{2} + M \times R_{dx}$$
$$dy = -\frac{N}{2} + N \times R_{dy} \tag{3.8}$$

where uniform random numbers between 0 and 1 were chosen for dx and dy. These values were then added to the coordinates of reabsorption for a pencil beam, (u, v), and this simulated an incident beam spread over the entire pixel instead of just a pencil beam. The corresponding schematic is shown in Figure 3.11.

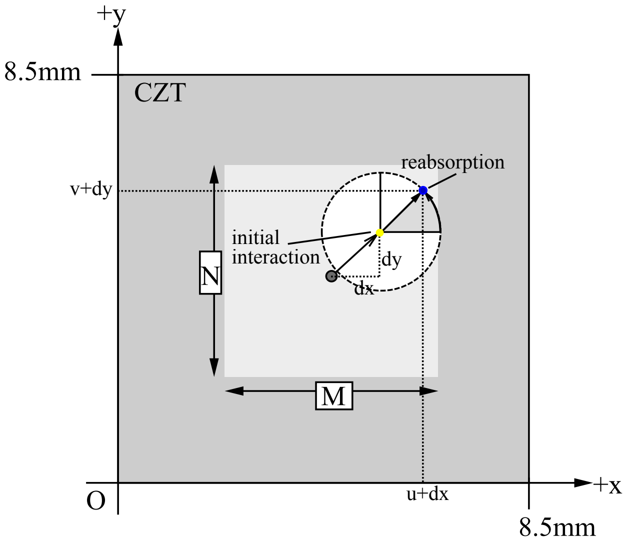

Figure 3.11 Schematic of mapping the primary photon to the center of the detector and then randomly spreading over the pixel area MxN. The distance of the reabsorption of the K x-ray from the origin was (u,v) which was then shifted randomly by dx and dy.

If the mapping and spreading process shifted the reabsorption position outside of the detector, a side escape is recorded. Otherwise the absorbed counter increased by one and the position of reabsorption was recorded in the x,y-plane as well as along the z-axis to create a depth profile. Then the entire process began again for the next primary photon.

The output of the code consisted of the counters that track the transmission of the primary photon and the complete escape of the K x-ray from the detector: back, forward, and side as well as the reabsorption of the K x-ray in the detector. The depth profile of primary photon interaction position as well as the interaction position of the K x-ray was also recorded and output as a data file with 10 μm increments over the detector depth. The 10 μm size was chosen as a compromise between precision of detector position and the size of the resulting data files. A two-dimensional matrix in which each element represented a 10 μm segment of the detector in the x,y-plane was also created to count K x-ray reabsorption position. The matrix enabled determination of whether the K x-ray was reabsorbed in the signaling pixel or in a neighboring pixel. The 2-D matrix was saved as a TIFF image. It was imported into the program ImageJ [44] to count K x-rays reabsorbed within the signaling pixel and in neighboring pixels.

- **Generating x-ray energy spectrum deteriorated due to characteristic x-ray escape**

The results of the simulation were used to deteriorate an ideal, theoretical 120 kVp x-ray spectrum split into five energy bins and to compare to experimental results with a CZT imaging detector. In this case, tilted angle experiments could not be compared since, at present, a strip pixel imaging detector does not exist. Therefore, only normal irradiation of square pixels could be compared to experiment.

For loss of K x-rays from the signaling pixel, counts were shifted from the energy bin corresponding to E0 to the next lowest energy bin. K x-rays received from neighboring pixels contributed to Bin 1 of the signaling pixel, since the average energy of K x-rays from Cd and Te falls within the energy range 20 – 40 keV. These calculations were done for each pixel size and configuration, and square pixels of 1 mm size were compared to experiment.

- **Spatial resolution**

Spatial blurring due to K x-ray escape was determined from the 2-D image of K x-ray reabsorption generated by the simulation. The image was opened in ImageJ and a plot profile was taken across the central region of the pixel. This profile was plotted and compared to the ideal case for all reabsorption occurring in the signaling pixel. Blurring along the width of the strip pixels will be the same as that for square pixels, but only for normal irradiation. Under tilted angle irradiation a greater fraction of K x-rays escape back from the detector surface, thus reducing escape to neighboring pixels. Along the length of the strip spatial resolution is determined by the collimation of the beam.

3.2.3 Experimental Study

Experimental measurement of a 120 kVp x-ray spectrum was done with a square pixel CZT detector. The monolithic CZT crystal was fabricated by eV-Products (Saxonburg, PA) with 3 mm thickness, 4.7 mm width and 16 mm length. The pixels are 0.93 x 0.93 mm^2 with 0.07 mm gap between pixels. The readout channel for each pixel allowed for separating the x-ray spectrum into five energy bins. The resulting x-ray spectrum was taken from one pixel. Further details about the imaging CZT detector are given in Chapter 5.

3.3 Results of Simulations

Results of simulations of a square pixel at 90° incidence as well as strip pixels at 90° and 10° incidences are given below. Although 15° simulations were also done with strip pixels, the results did not differ from 10° incidence substantially and therefore are not shown.

3.3.1 Depth Attenuation Profiles for Normal and Tilted Angle

The depth attenuation profiles of K x-ray reabsorption are shown in Figure 3.12 for 90° and 10° incidence. The depth profiles do not depend on pixel size.

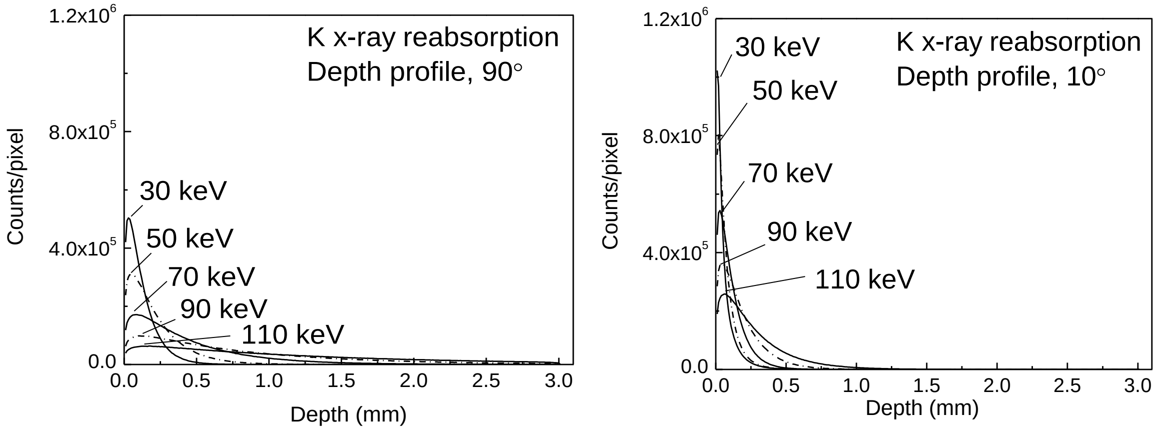

(a) **(b)**

Figure 3.12 Depth attenuation profiles of K x-rays for primary photons with different energies, for (a) 90° and (b) 10° irradiations of CZT.

By comparing the results from normal irradiation to tilted angle irradiation, it was clear that for tilted angle irradiation more interactions occur near the surface of the CZT detector. As a result of this shift of interactions toward the surface, there is more escape at the detector surface for tilted angle irradiation, the counts at zero depth are much lower for 90º irradiation relative to the peak counts for tilted angle irradiation. This increase in back escape can be an advantage because it decreases escape to neighboring pixels which is difficult to correct.

3.3.2 Back and Side Escape Fractions

Escape fractions with respect to energy for each pixel size are shown in Figure 3.13.

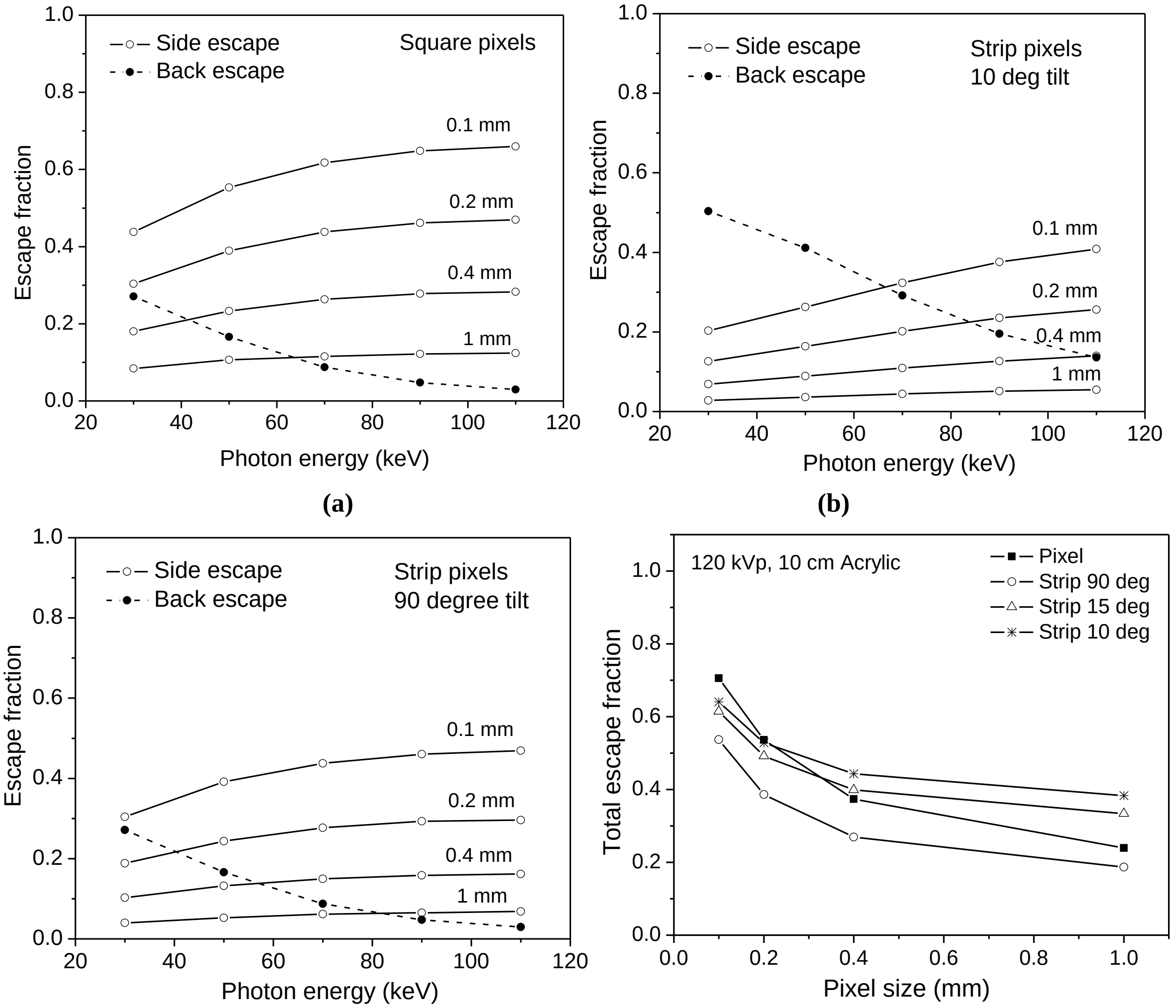

(a)

(b)

(c)

(d)

Figure 3.13 Fractions of the side escaped and back escaped characteristic x-rays versus x-ray energy for (a) square pixels and strip pixels with (b) 10 degree and (c) 90 degree tilt angles; (d) total escape fractions versus pixel size for 120 keV spectrum.

Side escape is shown for each pixel size for square pixels at normal irradiation and strip pixels at normal and tilted angle irradiation. In each case side escape fractions increase with decreasing pixel size. Back escape does not depend on pixel size or geometry, but is heavily dependent on the angle of irradiation. The fraction of side escape is smaller for strip pixels compared to square pixels, and smaller still for tilted angle irradiation compared to normal irradiation. Back escape is highest for tilted angle irradiation, especially for low energies, approaching 50% of all primary interactions at 30 keV. The increase in back escape is an advantage of tilted angle irradiation, since back escape does not create crosstalk between pixels so there is no double counting of initial photon interactions.

Total escape fractions with respect to pixel size are shown in Figure 3.13 (d) for square and strip pixels normally irradiated, as well as for strips irradiated at 15º and 10º incidences. Note that there is little difference between 15º and 10º incidences and that for small pixel sizes, 0.1 and 0.2 mm, square pixel escape is greater than or comparable to tilted angle irradiation of pixel strips. Side and back escape fractions for each energy are shown in table 3.1 for square pixels of all sizes. Table 3.2 gives escape fractions for strip pixels under normal irradiation while escape fractions for strip pixels at 10º irradiation angle are given in Table 3.3.

Table 3.1 Characteristic x-ray escape fractions for square pixels

Energy (keV)	Side escape 0.1 mm	Side escape 0.2 mm	Side escape 0.4 mm	Side escape 1 mm	Back escape Any size
30	0.44	0.31	0.18	0.085	0.270
50	0.55	0.39	0.24	0.110	0.165
70	0.62	0.44	0.265	0.117	0.088
90	0.65	0.46	0.28	0.123	0.048
110	0.66	0.47	0.283	0.125	0.032

Table 3.2 Characteristic x-ray escape fractions for strip pixels, 90º irradiation

Energy (keV)	Side escape 0.1 mm	Side escape 0.2 mm	Side escape 0.4 mm	Side escape 1 mm	Back escape Any size
30	0.31	0.19	0.10	0.042	0.270
50	0.39	0.24	0.13	0.053	0.165
70	0.44	0.28	0.15	0.063	0.088
90	0.46	0.29	0.16	0.066	0.048
110	0.47	0.30	0.163	0.069	0.032

Table 3.3 Characteristic x-ray escape fractions for strip pixels, 10º tilted angle					
Energy (keV)	Side escape 0.1 mm	Side escape 0.2 mm	Side escape 0.4 mm	Side escape 1 mm	Back escape Any size
30	0.21	0.13	0.07	0.030	0.51
50	0.27	0.16	0.09	0.038	0.41
70	0.33	0.20	0.11	0.047	0.29
90	0.38	0.24	0.125	0.053	0.20
110	0.41	0.26	0.14	0.056	0.14

3.3.3 Building X-ray Spectra Considering Escape

The building components of simulated energy spectra deteriorated due to K x-ray escape are shown in Figure 3.14.

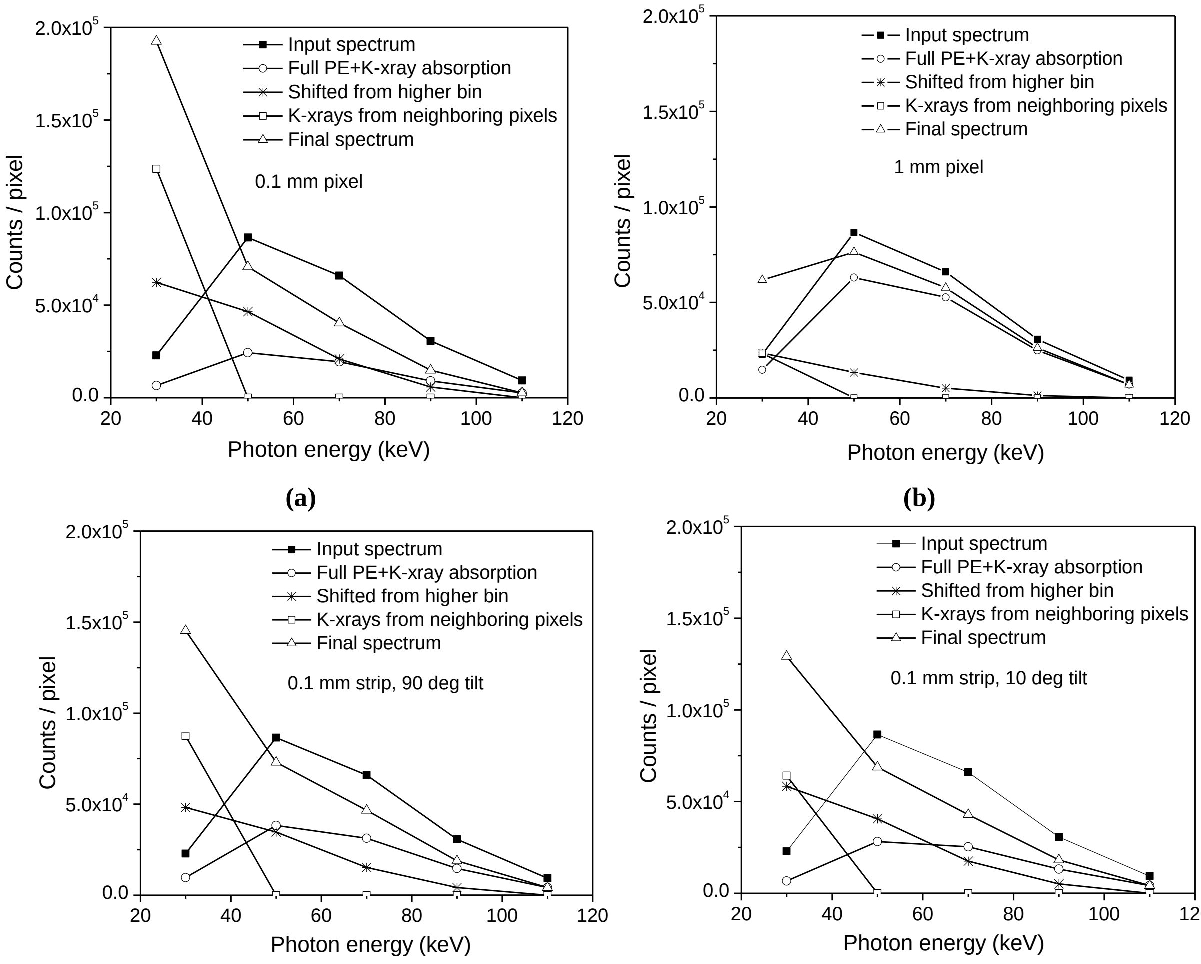

(a) (b)

(c) (d)

Figure 3.14 Energy spectrum of primary x-rays (input spectrum), final x-ray spectrum deteriorated due to characteristic x-ray escapes, and components of the final spectrum resulting from different processes. Examples are shown for square pixels with (a) 0.1 mm and (b) 1 mm sizes, and for strip pixels with 0.1 mm width and (c) 90º and (d) 10º tilt angles.

Square pixels of size 0.1 and 1 mm are shown in Figure 3.14 (a) and (b), respectively, while strip pixels of 0.1 mm width and 90° and 10° tilt angles are shown in Figure 3.14 (c) and (d). In each case the input spectrum is shown which would also be the detected spectrum for an ideal detector. The actual spectrum consists of three main events, 1) full absorption counts of both the photoelectron (PE) and the K x-ray, 2) counts shifted from higher energies due to K x-ray escape, and 3) counts received in energy bin 1 from K x-ray escape from neighboring pixels.

The final spectrum shown is the combination of all these events. It is clear that for small pixel sizes the deterioration is severe and the worst case is for a square pixel of 0.1x0.1 mm^2 size.

3.3.4 X-ray Spectra with Full Absorption Only

Full absorption spectra are shown in Figure 3.15 for (a) square pixels, (b) strip pixels normally irradiated, and (c) strip pixels irradiated at 10^o tilt angle.

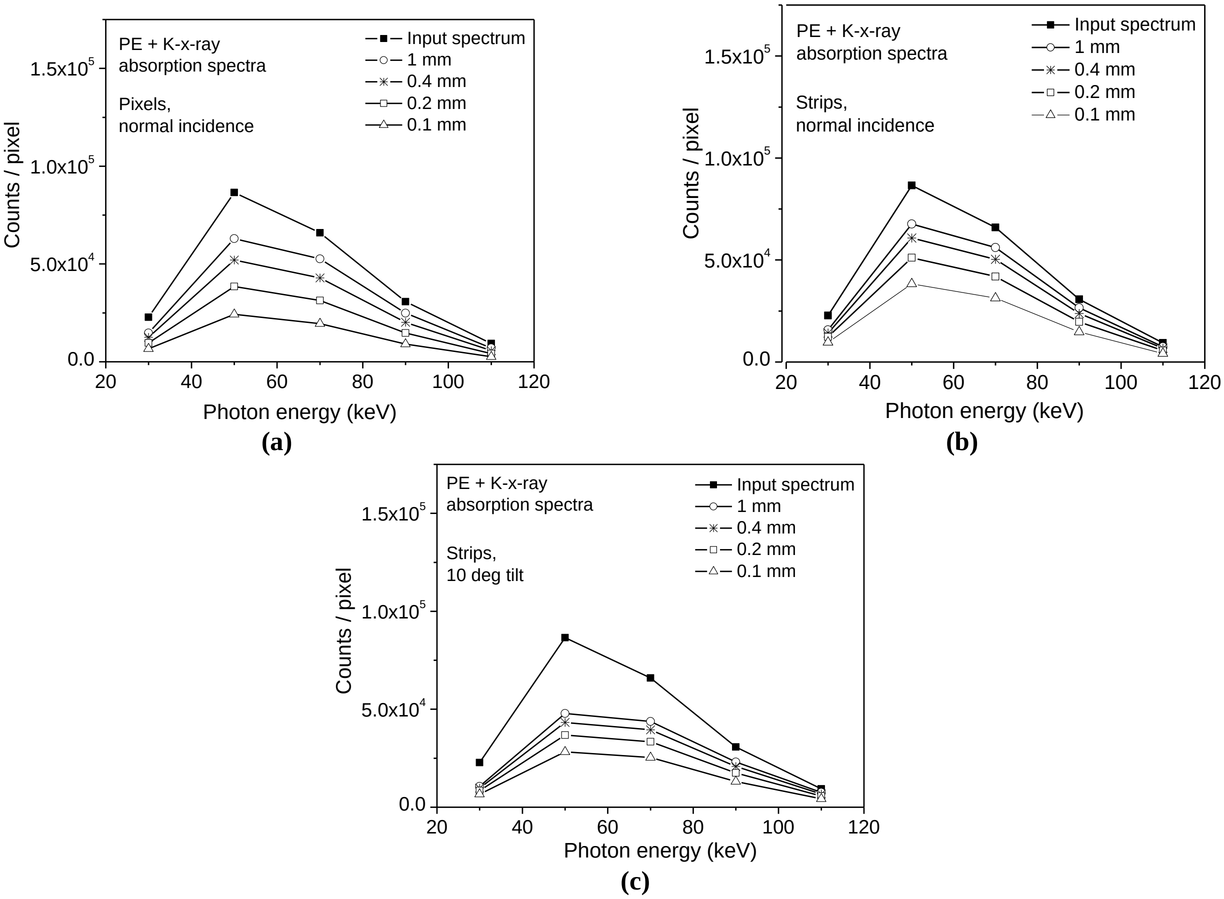

(a)

(b)

(c)

Figure 3.15 Full absorption spectra of primary x-rays compared to input spectrum for all pixel sizes and configurations: (a) square pixels, (b) strip pixels with normal irradiation, and (c) strip pixels with 10° tilted angle irradiation.

As pixel size decreases, full absorption counts decrease significantly. The effect is less severe for strip pixels normally irradiated than square pixels or tilted angle strip pixels. Square pixels suffer more from side escape while tilted angle increases back escape.

3.3.5 Final X-ray Spectrum

Final x-ray spectra deteriorated due to K x-ray escape along with input spectra are shown in Figure 3.16 for (a) square pixels, (b) strip pixels normally irradiated, and (c) strip pixels irradiated at 10º tilt angle. These results show how pixel size and geometry affect the detected x-ray spectrum. Deterioration is most severe for square pixels and for small pixel size for all pixel geometries.

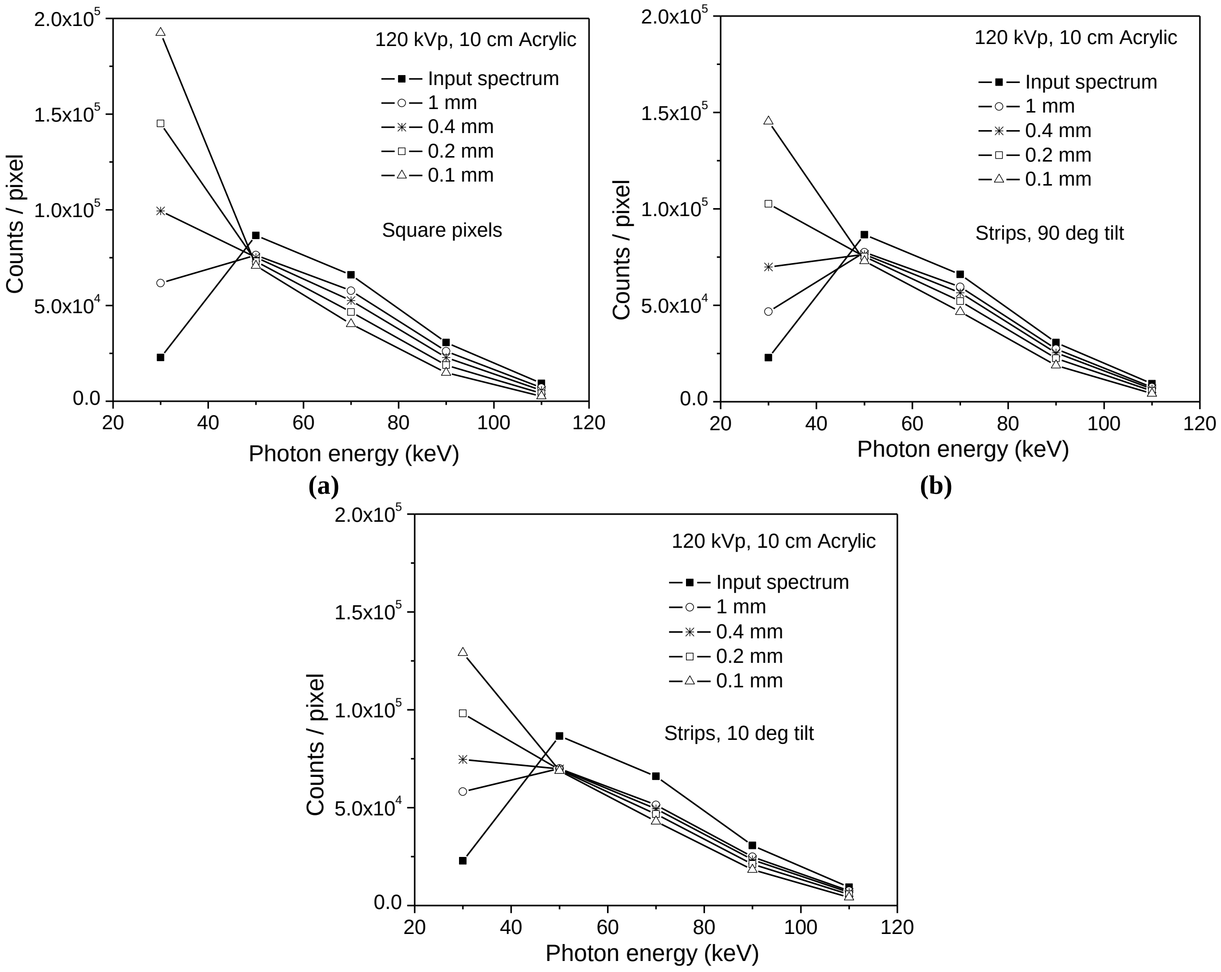

(a) (b)

(c)

Figure 3.16 X-ray spectra deteriorated due to K x-ray escape with (a) square pixels, (b) strip pixels with normal irradiation, and (c) strip pixels with 10° tilted angle irradiation.

3.3.6 2-D Mapping of K x-ray Reabsorption

The 2-D maps of K x-ray reabsorption position for a central pixel irradiated while surrounding pixels are not are shown for square pixels of different sizes in Figure 3.17.

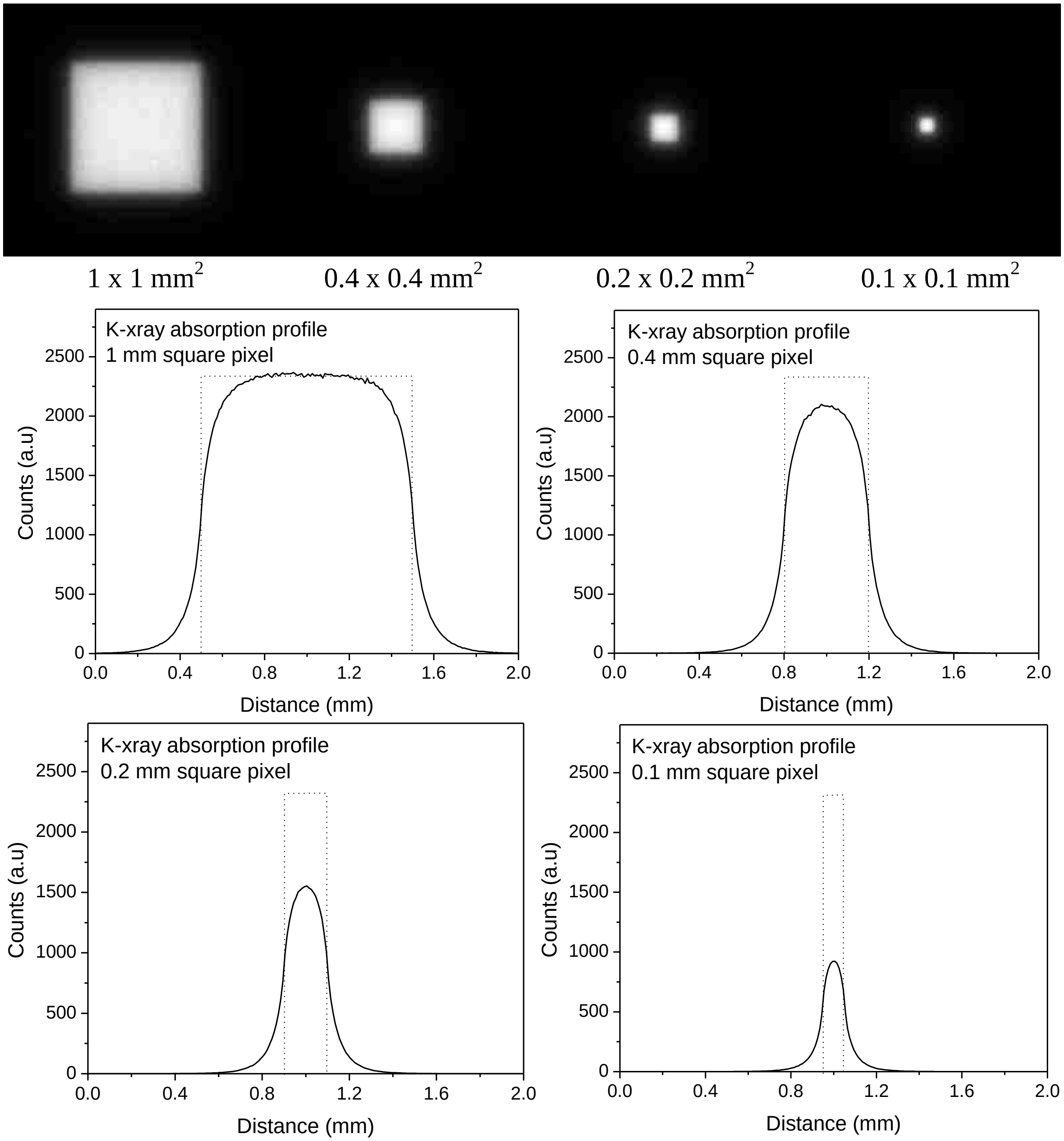

Figure 3.17 2D maps of characteristic x-ray absorption and central profiles. The primary x-ray beam was shaped to a square beam normally incident on the CZT surface. The dotted rectangles indicate size and intensity of the primary x-ray beam.

Corresponding plot profiles are also shown. These results show the effect of K x-ray escape on spatial resolution. As pixel size decreases a greater fraction of counts contribute to counts in neighboring pixels, resulting in double counting and destroying both energy and spatial resolution. Figure 3.18 shows results of simulations of a central pixel not irradiated while surrounding pixels are irradiated. These results show counts received due to K x-ray escape from neighboring pixels.

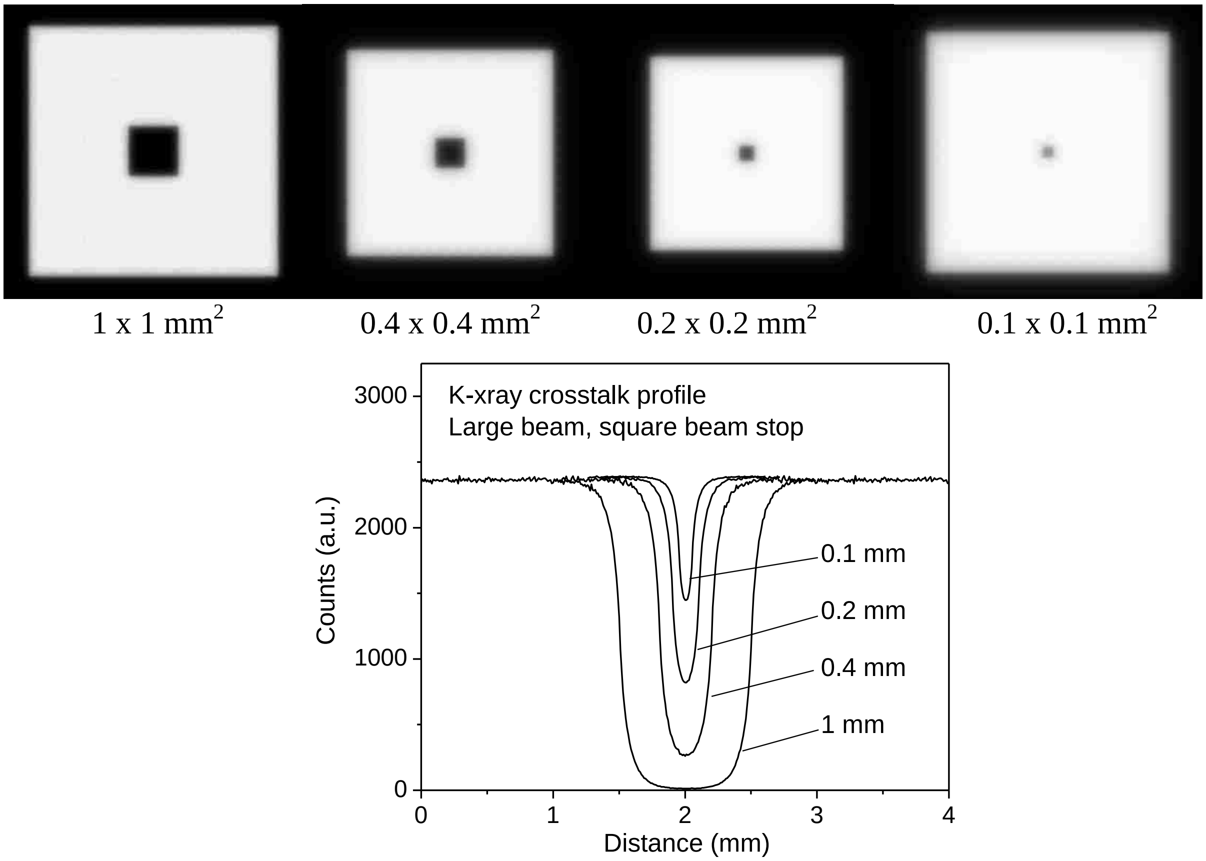

Figure 3.18 2D maps of K x-ray absorption are shown. A large beam irradiated the CZT surface except for the square pixel areas at the center. The image profiles show contamination of the unexposed pixel by characteristic x-rays from surrounding areas. Pixel sizes were in the 0.1-1 mm range.

3.3.7 Spatial Resolution

Spatial blurring for a central pixel irradiated while neighboring pixels are not irradiated is quantified in Figure 3.19. The central pixel is designated as pixel position ‘0’ and counts are shown for this pixel as well as neighboring pixels. Square pixels of different sizes are shown in Figure 3.19 (a) while Figure 3.19 (b) shows results for 0.1 mm width pixels for strips at 90° and 10° as well as 0.1 mm square pixel.

Also shown is spatial resolution for strip pixels in the direction of the strip collimator for width 0.1 mm. In this direction there is no spatial blurring. The best spatial resolution along the pixel width direction for 0.1 mm pixels is for 10° tilt angle irradiation of a strip pixel.

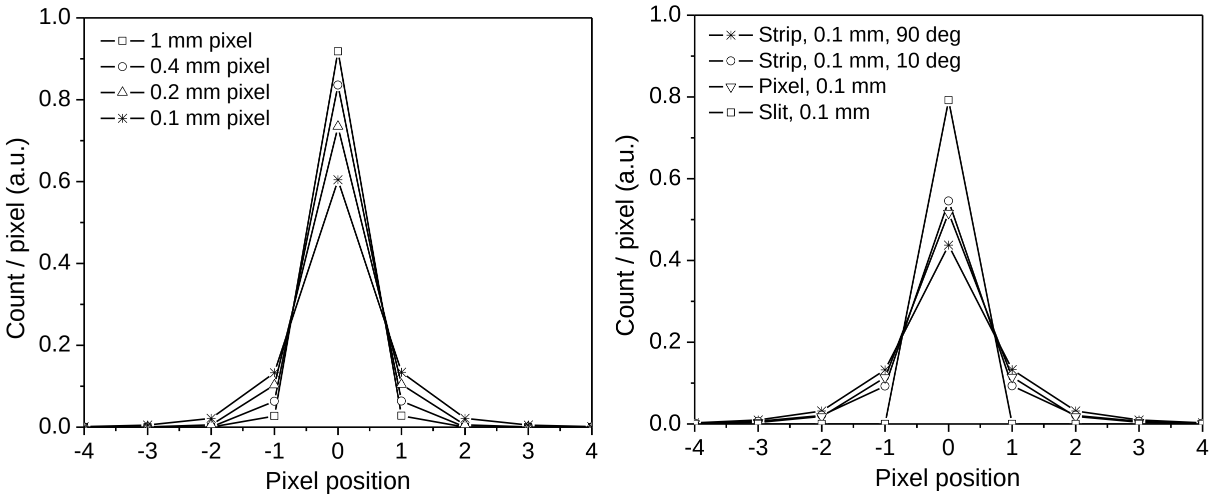

(a) (b)

Figure 3.19 Loss of spatial resolution due to K x-ray escape for (a) a 2D array of square pixels and (b) scanning slit imaging with a 1D array of strip pixels. Counts versus pixel positions are plotted. Spatial resolution is compared in (b) for four cases including square pixels, strip pixels at two irradiation angles, and a strip pixel in the scanning slit direction determined by slit width (chosen same as strip width).

3.3.8 Experimental Results with Square Pixel Compared to Simulation

Experimental results are shown in Figure 3.20 along with the simulated spectrum for a square pixel of 1 mm width.

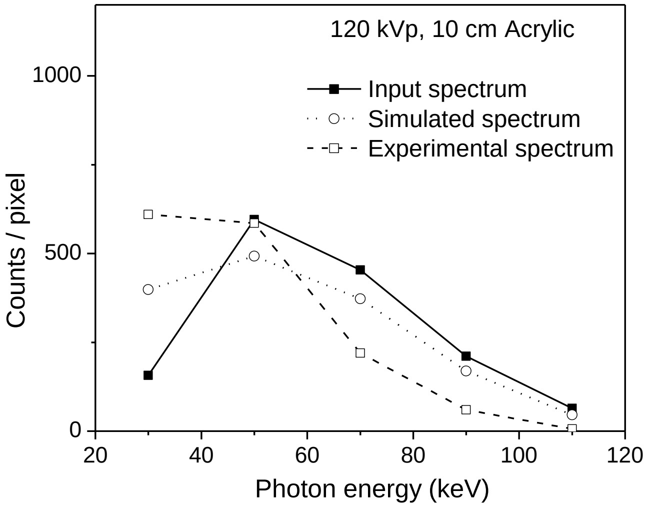

Figure 3.20 Measured x-ray spectrum as compared to simulated and input spectra. The experimental spectrum was deteriorated more than predicted due to K x-ray escape. Other factors affecting the spectrum might be due to hole trapping, and charge sharing due to charge diffusion.

The beam measured was 120 kVp with 10 cm acrylic filter. The input spectrum is also plotted to show the severity of deterioration of the measured and simulated spectrum. The experiment is more severely deteriorated than the simulated spectrum. This may be due to hole trapping effects which were not accounted for in the simulation. Hole trapping can be accounted for by physical modifications, such as tilted angle irradiation shown in the previous chapter.

3.4 Conclusions and Advantages of Tilted Angle Irradiation of Strip Pixels

Simulation results indicate that strip pixels suffer less overall from K x-ray escape than square pixels. Along the length of the strip pixel, spatial resolution is governed by the width of the collimation slit of the x-ray beam. Strip pixels have the advantage of operation in tilted angle mode. Tilted angle configuration reduces hole trapping effects, as shown in the previous chapter. It also allows for a thinner CZT crystal to be used without decreasing detection efficiency. A thinner crystal reduces lateral spread of charge due to diffusion as charge drifts to its electrode. The diffusion reduces spatial and energy resolutions similar to K x-ray escape and should be limited.

The additional advantage of tilted angle irradiation of strip pixels is the increase in back escape, resulting in less K x-ray escape to neighboring pixels. Since the energy of the K x-rays is discrete and known, correction methods can be developed relatively easily to account for K x-ray loss due to back escape.

4 IMAGING CZT DETECTOR

The hole trapping in CZT material and charge sharing between detector pixels will negatively affect the performance of future x-ray and CT imaging systems with energy resolving CZT detectors. Currently no such system is available for clinical application. The hardware and software based methods described in previous chapters can help to resolve these problems. In this chapter an experimental imaging system is described based on a pixelated CZT detector. Details of the imaging system, results of spectroscopic measurements, as well as spectral CT images of a clinically relevant phantom will be presented. Limitations of the system due to presence of the hole trapping and charge sharing will be discussed, along with possible methods of improvements in future research.

The multi-pixel CZT imaging detector was presented briefly in Chapter 3. The purpose there was to compare the experimental measurement of a 120 kVp x-ray spectrum to the simulated spectrum deteriorated due to characteristic x-ray escape for a 1x1mm^2 square pixel. In this chapter a detailed description of the CZT detection system is given. Each pixel in the detector is capable of separating a counted photon into one of five energy bins. It has been shown that for most medical imaging applications, increasing the number of bins beyond five does not significantly improve SNR [17]. Blurring at the borders of the energy bins due to hole trapping and charge sharing has inhibited the detector from reaching its theoretical potential.

4.1 Description of the NEXIS Detector

The detector system used in this study was purchased from NOVA R&D, Inc. (Riverside, CA). The system, known as NEXIS^{TM} (**N-E**nergy **X**-ray **I**maging **S**canning), consists of a linear CZT pixel array and integrated circuit (IC) readout electronics [45].

The monolithic CZT has 3 mm thickness, 4.7 mm width and 16 mm length. The entrance surface is covered with a continuous Pt electrode of submicron thickness. The pixel array also consists of thin Pt electrodes and is on the other side of the crystal. The pixels are 0.93 x 0.93 mm^{2}with a 0.07 mm gap in between pixels. There are sixteen CZT crystal modules, each with two rows of 16 pixels for a total of two rows of 256 pixels. A schematic of the crystal and pixel array is shown in Figure 4.1.

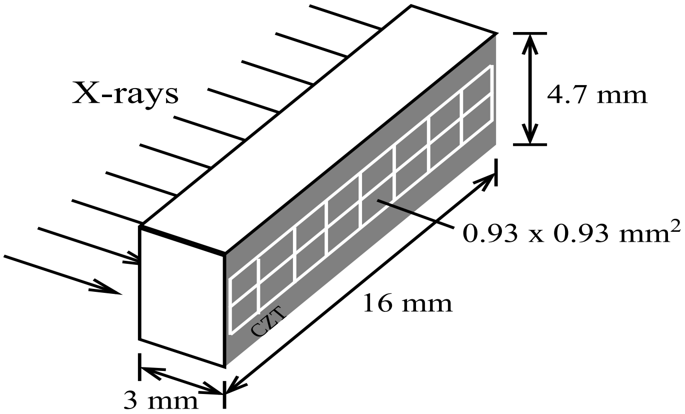

Figure 4.1 Pixel configuration of the CZT detector used for experiments.

- **Readout electronics**

The IC electronics are called XENA^{TM} (**X**-ray **EN**ergy-binning **A**pplicaitons). The XENA IC has 32 readout channels. Each pixel is connected to its own readout channel as shown in the schematic in Figure 4.2 (a). Each channel has five independent compensators that could be set to different threshold levels. Each compensator is connected to a counter with 16-bit capacity. An example of threshold settings is shown for a 120kVp x-ray beam in Figure 4.2 (b) where the five thresholds levels are 20, 40, 60, 80, and 100 keV. This creates 5 energy bins with 20 keV widths. The result is that five different images with five different energies can be acquired from one image acquisition by subtracting data in D_{i+1} from data in D_i.

4.2 Importance of Energy Resolution

Photon counting alone offers improvements in SNR compared to charge-integrating detectors, however, the main advantage lies in energy resolution. The ability to separate a single image into multiple energy bins allows for task-dependent energy-weighting. Energy-weighting applies a weighting factor, $\omega(E)$, to an image to increase contrast between the background and the object of interest. This weighting factor depends on the attenuation coefficients of the background and object. Consider the background object in Figure 4.3 with embedded contrast object. A beam of energy E with photon intensity N_0 is incident on a background material with thickness L. Part of the beam passes through contrast material of thickness d. Photon intensity detected without and with the contrast material are designated as N_b and N_c, respectively. If a weighting factor is applied to these detected photons, the SNR is optimized and contrast is enhanced [15].

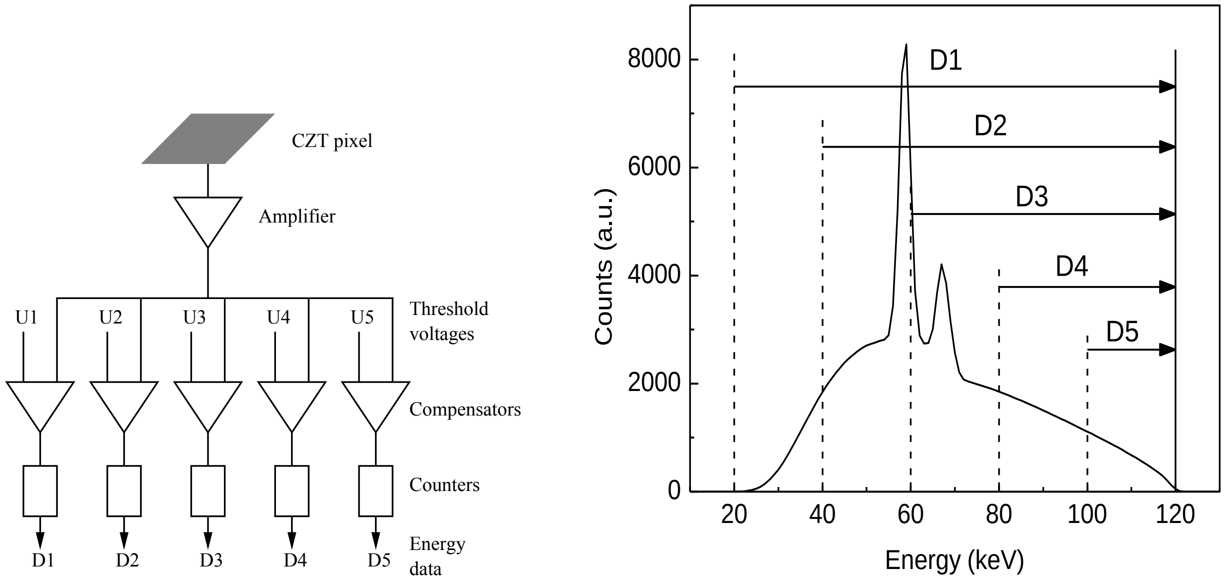

(a) **(b)**

Figure 4.2 (a) Readout electronics for each pixel are able to separate measurements in to energy bins. (b) X-ray energy spectrum of 120 kVp tube voltage split into 5 energy bins. Simulations were performed for the average energies in these energy bins.

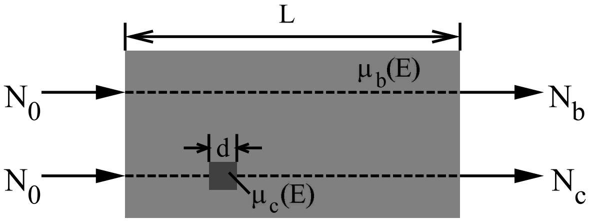

Figure 4.3 Background object with embedded contrast object. The attenuation coefficients of each material for incoming photons, N_0, with energy E are $\mu_b(E)$ and $\mu_c(E)$, respectively. The number of photons transmitted through the background without and with contrast are given by N_b and N_c, respectively.

The weighting factor is derived from the values of N_b and N_c, given by

$$\begin{aligned} N_b(E) &= N_0(E)e^{-\mu_b(E)L} \\ N_c(E) &= N_0(E)e^{-\mu_b(E)(L-d)-\mu_c(E)d} \end{aligned} \tag{4.1}$$

The quotient of the sum and difference of N_b and N_c is the weighting factor, the result of which to depends on the attenuation coefficients of the background and contrast material and the thickness of the contrast material [17], as shown by

$$\omega(E) = \frac{N_b(E) - N_c(E)}{N_b(E) + N_c(E)} = \frac{1 - e^{-[\mu_c(E)-\mu_b(E)]d}}{1 + e^{-[\mu_c(E)-\mu_b(E)]d}} \tag{4.2}$$

Therefore, this weighting factor is task-dependent in that it takes into account the type of contrast object of interest. If energy resolution is deteriorated, weighting images is less effective.

In addition to energy-weighting, material decomposition in a single scan is possible with an energy-resolving detector. The basic decomposition process achieved by dual-energy subtraction is shown in Figure 4.4 (a).The linear attenuation coefficients of some materials vary a great deal over the diagnostic x-ray spectrum while some vary only a little. This fact is shown in Figure 4.4 (b) for the linear attenuation coefficients of breast tissue and calcifications in the breast that may indicate breast cancer. Dual-energy subtraction exploits this difference using two images, one low energy and one high energy. A factor is applied to one of the images to cancel a material, either tissue or calcification, for example, so that only the material of interest is visible when the two images are subtracted. The process can be done with a single image if energy resolution is possible and the image can be divided into high and low energy images. If energy resolution is deteriorated, the process is less effective, as is the case with energy-weighting.

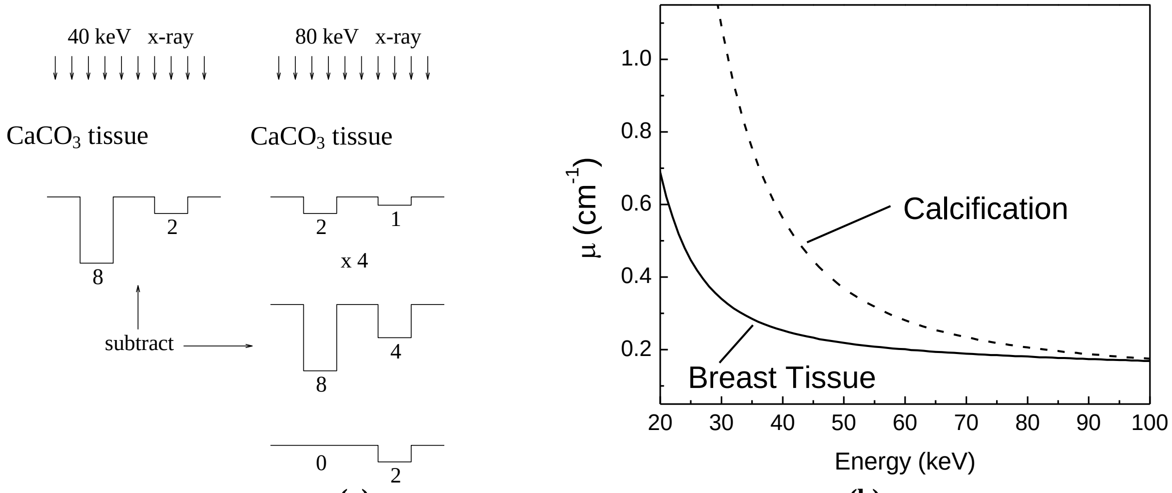

(a) (b)

Figure 4.4 (a) Basic process of material decomposition by dual-energy subtraction. (b) Difference in attenuation coefficients between breast tissue and calcifications that might indicate breast cancer.

The CZT imaging detector suffers from charge sharing between pixels which causes significant deterioration of energy resolution. Although resolution of each individual photon is not necessary, blurring at the borders of energy bins, shown in figure 4.5 (a) hinders the detector from practical capabilities. Figure 4.5 (a) shows examples of energy resolution for an ideal detector with no blurring, as well as a practical detector with inherent blurring due to statistical fluctuations. The actual pixel detector has significant blurring, mainly due to charge sharing.

This creates overlap at the energy bin borders; an example is shown in Figure 4.5 (b).We investigated blurring in the detector by measuring isotope sources.

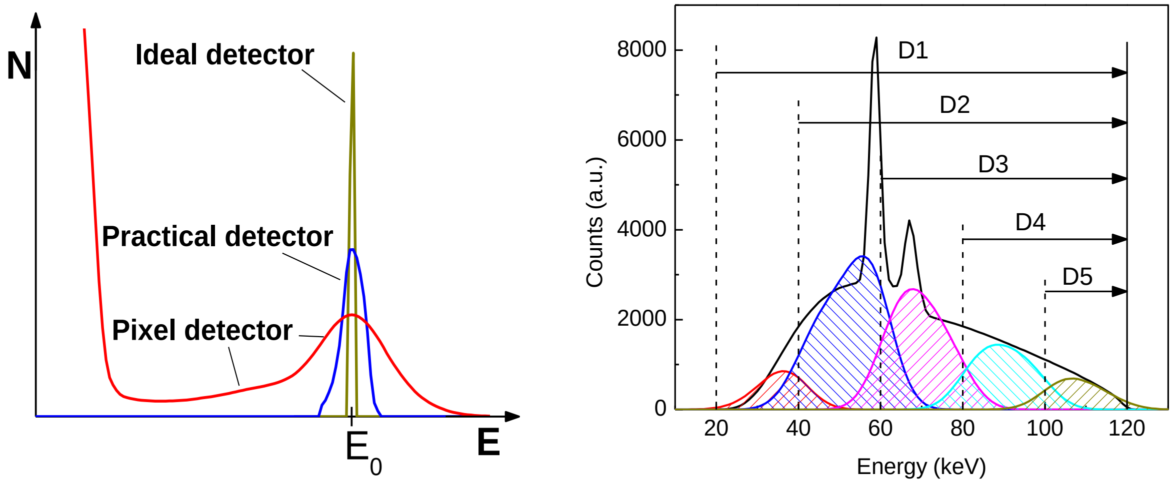

(a) **(b)**

Figure 4.5 (a) Example of ideal energy spectrum compared to a practical detector and an available pixel detector. (b) Blurring across the borders of the energy bins for a polychromatic x-ray spectrum decreases energy-resolving advantages of the detector.

4.3 Isotope Measurements with the NEXIS Detector

Energy spectra for isotope sources were acquired by changing voltage threshold settings with step size for 0.1 V for ^{241}Am and 0.2 V for ^{57}Co. Once the set of pixel images were acquired, the image set was duplicated and one set shifted so that the two could be subtracted. In this way the number of counts per energy bin could be determined. The energy spectra are shown in Figure 4.6.

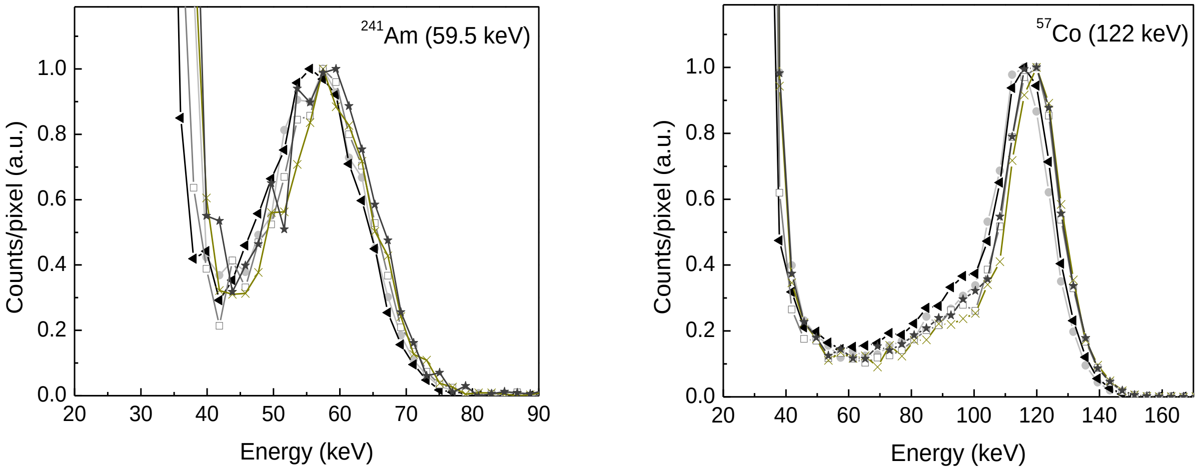

(a) **(b)**

Figure 4.6 Measured spectra for several adjacent pixels for (a) ^{241}Am and (b) ^{57}Co.

Data were normalized to peak number of counts. The threshold voltages were calibrated so that the average peak position across all pixels corresponds to the energy of the particular isotope. The broadening of the peaks in each case indicates the degree of spectral blurring in the detector.

4.4 Imaging Experiments with NEXIS Detector

In spite of the high degree of energy blurring, preliminary spectral CT images have been obtained of an acrylic phantom with embedded contrast of $CaCO_3$, water, and aluminum wires. Details of the phantom are shown in Figure 4.7. The 14 cm diameter size of the phantom corresponds to the average breast size of women in the United States [2, 46]. $CaCO_3$ represents calcifications in the breast that may indicate the presence of breast cancer.

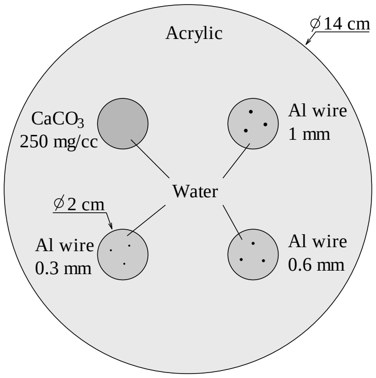

Figure 4.7 Schematic of phantom including aluminum wires and $CaCO_3$ contrast.

The spectral CT images are shown in Figure 4.8 where a single image has been divided into five energy bins Figure 4.8 (a–e) and the final composite image of all energies in Figure 4.8 (f). The separation of the composite image into separate energy bins allowed for decomposing the images for a material of interest, however, overlap at the border of the low and high energy bins reduced the overall effectiveness of the dual-energy subtraction technique. An example of the energy spectrum overlap at the energy bin border is shown in Figure 4.9. Figure 4.10 shows results from material decomposition by dual-energy subtraction. The original image is shown in Figure 4.10 (a) while Figure 4.10 (b) shows the decomposition of tissue when CaCO3 is the material of interest and Figure 4.10 (c) shows the image of decomposed $CaCO_3$.

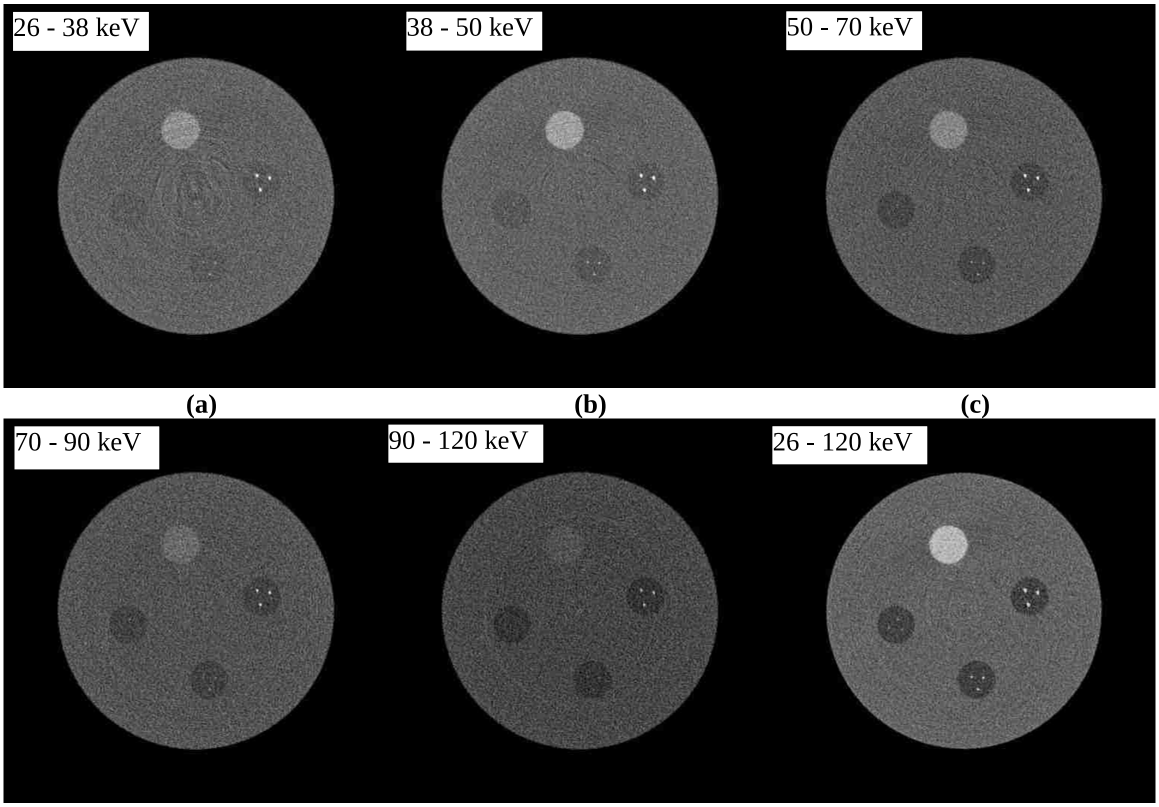

(a) (b) (c)

(d) (e) (f)

Figure 4.8 (a-e) Spectral CT images of resolution phantom acquired in 5 energy bins and (f) the final CT image composed from 5 bin data.

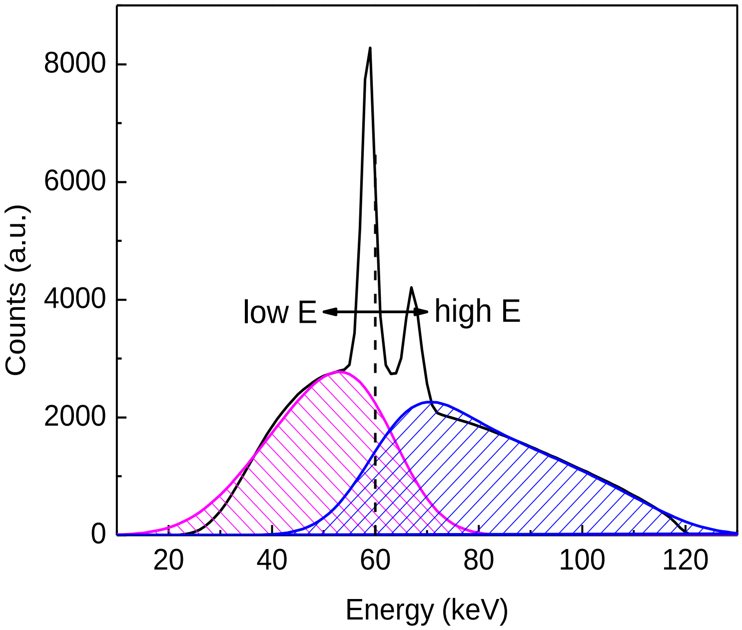

Figure 4.9 Overlapping at the border between low and high energy bins for dual-energy subtraction limits the effectiveness of this technique.

4.5 Conclusions and Modification of Imaging CZT Detector

The spectral CT images presented here demonstrate the capabilities of the CZT detector. Material decomposition in a single scan reduces patient dose compared to multiple scans and also eliminates blurring artifacts due to patient motion between scans. However, due to the energy blurring at bin border discussed previously, the CZT detector does not yet reach its full potential.

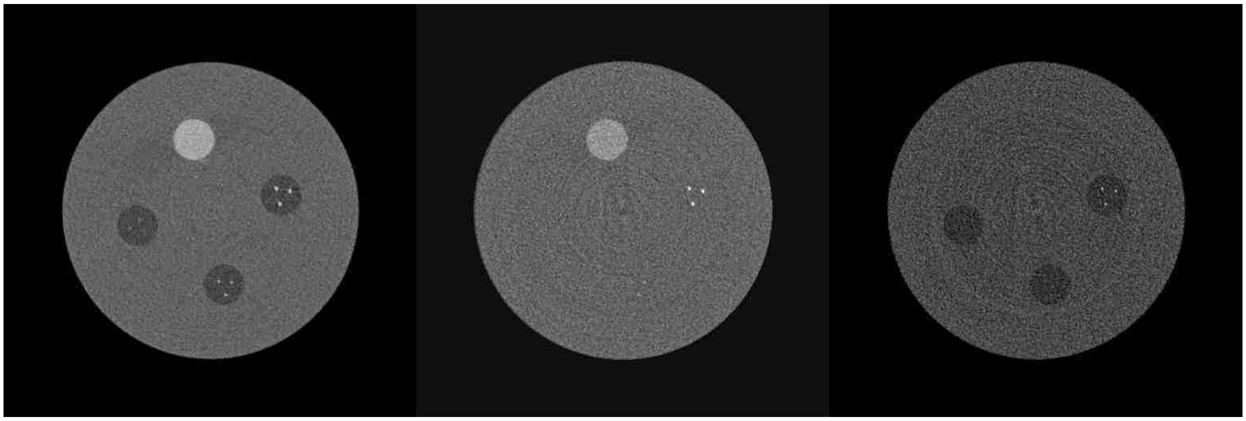
(a) (b) (c)

Figure 4.10 Material decomposition with Spectral CT: (a) image of the resolution phantom, (b) tissue-cancelled image, and (c) $CaCO_3$ cancelled image.

The characterization of the CZT detector done for this dissertation explored low energy tailing of energy spectra in the detector. We showed that hole trapping effects can be reduced by manipulation of detector configuration. We also showed that it is possible to correct for characteristic x-ray escape by applying results from simulations that were done. The results point to a detector configuration of strip pixels operated in tilted angle mode with respect to the beam offers the most promising means of reducing spectral tailing in the detector. This configuration reduces hole trapping and crosstalk between detector pixels. It also allows the use of a thinner CZT crystal without loss of detection efficiency. A thinner crystal can decrease charge sharing effects by reducing charge diffusion, which would also improve energy resolution.

Future research should include the fabrication a thin strip pixel CZT detector for operation in tilted angle mode. Images from this detector should be compared to the square pixel detector presented here to determine improvements in energy resolution and SNR. These results should also be compared to conventional x-ray imaging detectors to verify that a photon counting, energy-resolving CZT detector is viable for clinical implementation. The benefits of the detector for patient dose reduction and diagnostic value should be evaluated against cost of implementation of this new technology. However, the next chapter demonstrates that a CZT detector for diagnostic spectroscopy requires only slight modifications to be clinically applicable.

5 X-RAY SPECTROSCOPY WITH A CZT DETECTOR

The previous chapters showed that through tilted angle geometry spectral tailing can be sufficiently reduced. It was also shown that through characteristic x-ray escape simulations K-x-ray escape effects can be predicted. We can now apply tilted angle irradiation and K-escape correction methods for x-ray spectroscopy in the diagnostic energy range.

X-ray spectroscopy itself is an important area of study to characterize diagnostic x-ray beams. Radiation protection and dosimetry calculations rely on accurate information about the x-ray beam. Proper characterization is also needed for image quality assessment in x-ray and CT imaging to determine the detection efficiency of the detector. Complete knowledge of the x-ray beam is also required for spectral x-ray and CT imaging. Currently there is not a spectroscopy method available for easy, in-house measurements.

Measurements of diagnostic x-ray spectra have traditionally been done using high-purity germanium detectors (HPGe) [14, 47]. These detectors offer high energy resolution and sufficient x-ray absorption. The disadvantage is that, because of the low atomic number of Ge, the volume of the detector must be quite large and Compton scatter in the detector is significant. Also, HPGe detectors require cooling with liquid nitrogen to achieve high energy resolution. The overall effect is that HPGe detectors are bulky and unwieldy, making them unsuitable for clinical use where space between the x-ray source and detector is often limited. The use of liquid nitrogen also makes the detector relatively expensive, another drawback for widespread use.

Recently, attention has been given to CdTe and CZT detectors as attractive alternatives to the large and expensive HPGe detectors. Table 5.1 shows properties of CdTe and CZT detectors compared to HPGe detectors. Both CdTe and CZT have higher effective atomic number and higher density than germanium so a much smaller volume can be used to achieve the same detection efficiency. CZT has the additional advantage over CdTe that it can operate at room temperature.

Table 5.1 Properties of detectors for x-ray spectroscopy

	Effective atomic number	Density (g/cc)	Cooling requirements
HPGe	32	5.33	LN_2, -200 ºC
CdTe	49	6.06	Peltier cooler, -40 to -20ºC
$Cd_{0.9}Zn_{0.1}T$	49	5.78	None required

CdTe detectors have been studied for spectroscopy of diagnostic x-rays with corrections for hole trapping and K x-ray escape as well as Compton scatter [48]. Thin detectors were used in the study to reduce hole trapping issues, however, this also decreases detection efficiency. CdZnTe detectors have also been investigated for mammography [49] and diagnostic [50] x-ray spectroscopy, however, in each case it has been necessary to apply corrections for hole trapping. These corrections may not apply broadly to CZT detectors as hole trapping varies with crystal purity and may change with each detector.

It was shown in Chapter 2 that tilted angle irradiation can be used as a physical method to reduce the effects of hole trapping which does not depend on crystal purity. In Chapter 3 characteristic escape fractions were calculated which can be applied to deteriorated spectra to account for loss of energy resolution. Here, we combine these results to show that CZT detectors are viable for in-house spectroscopy of diagnostic x-rays.

In addition, we use a detector geometry that differs from the planar geometry previously presented. The alternate detector is what is known as a capacitive grid detector [51, 52]. This type of detector operates with a gradient electric field, as opposed to the uniform electric field found in the planar detector. The field is distorted by extension of the cathode by 1 or 2 mm around the edges of the detector. The objective is to create an electron-only device, unlike the planar detector which operates as an electron-hole collection device.

We combined the capacitive grid detector with tilted angle irradiation geometry to effectively eliminate hole trapping effects. We then applied correction techniques to the measured spectra to account for K x-ray escape. We measured both monoenergetic isotope sources and x-ray spectra typically used in diagnostic applications. We compared the results to normal irradiation of both a planar and capacitive grid detector to quantify improvement. The result indicate that normal irradiation of the capacitive grid detector provides similar improvement to the planar detector in tilted angle mode, however, the combination of tilted angle irradiation and the capacitive grid detector offer the best results.

5.1 Evaluating a CZT Detector for X-ray Spectroscopy

5.1.1 Modifying Interaction Depth and Electric Field

Recall from Chapter 2 that signal amplitude depends on the depth of interaction and this depth dependence is due to the large difference between the mean free path lengths of electrons and holes. More precisely, it is the small mean free path length of the holes that creates this depth depends because holes become trapped and cannot contribute to the signal. The mean free path length was said to be directly dependent on the applied electric field in the detector. Therefore, by decreasing the electric field the mean free path length is also reduced. This becomes a useful phenomenon in creating an electron-only collection device. By decreasing the electric field in a small region of the detector where charge is created, holes are even more likely to become trapped. Since electrons have a larger mean free path length they are still able to drift out of the low field region of the detector. Once in the high field region they contribute to signal as usual. Schematics of the electric field lines for a planar and capacitive grid detector are shown in Figure 5.1.

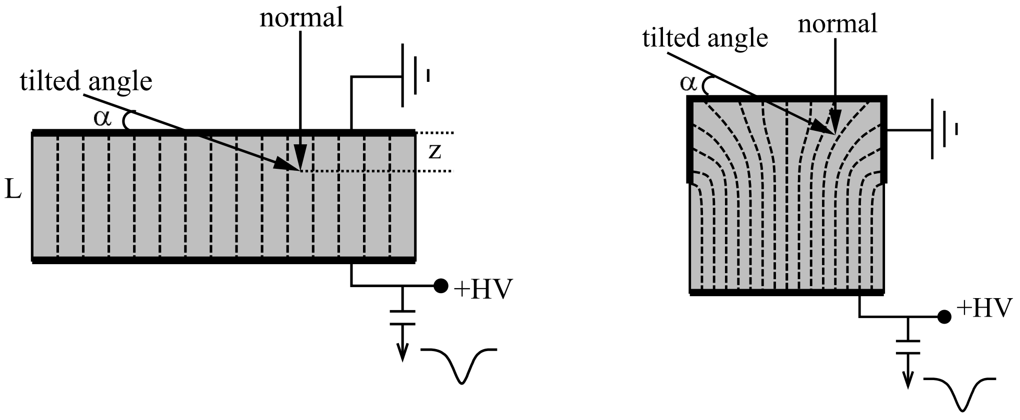

(a) (b)

Figure 5.1 Schematics of electric field lines and x-ray incidence in (a) a planar detector and (b) a capacitive grid detector. The interaction depth of the primary photon is given by z and the angle of incidence between the beam and the detector surface is given by α.

The use of tilted angle irradiation with the capacitive grid detector ensures that most interactions occur in the low field region. Interactions that occur in the high field region can contribute to low energy tailing because holes are not trapped as easily. Also, electrons may travel different distances to generate signal for the same primary photon energy and recall that signal is generated for the charge in motion.

5.1.2 Measurements with Planar and Capacitive Grid Detectors

Both the planar and capacitive grid detectors used in this study were purchased from eV-Products (Saxonburg, PA). Schematics of the detectors are shown in Figure 5.2. The planar detector is the same detector used in Chapter 2 for tilted angle irradiation studies. The capacitive grid detector is a Single Point Extended Area Radiation (SPEAR) detector with CAPture^{TM} technology. The CZT crystal in the capacitive grid detector is 5x5x5 mm^3 and the cathode extends 2 mm around the sides of the crystal. The CZT is enclosed in a brass casing.

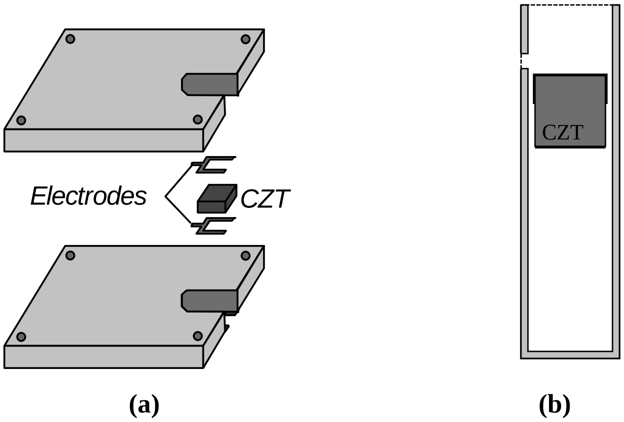

Figure 5.2 Schematic of (a) planar detector and (b) capacitive grid detector with housing and electrodes.

It was necessary to create a hole in this housing, as shown in the schematic, to perform tilted angle irradiation measurements to reduce scatter and attenuation of low energy photons. The hole was covered with a 0.1 mm thick Al foil. A photo of the detectors is shown in Figure 5.3 to demonstrate the small size of the detectors. The electronics used were the same as those used in Chapter 2 for the planar detector. The exception for the capacitive grid detector is that the preamplifier is contained in the detector housing. A bias voltage of 800V was applied to the capacitive grid detector while the planar detector was again operated at 300V.

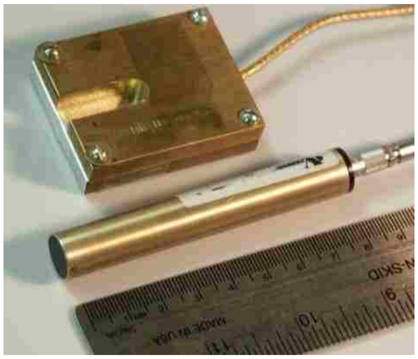

Figure 5.3 Planar detector (top) and capacitive grid detector (bottom). The small size and ability to operate at room temperature make CZT detectors ideal for clinical use.

- **Isotope sources measurements**

Radioisotope sources were measured to compare low energy tailing for each detector at different angles of incidence between the source and detector surface. The measurements were also used to calibrate the x-ray spectra from the ADC. Two isotopes were chosen based on their prominent energy peaks within the diagnostic energy range. The maximum energy from a 120 kVp beam corresponds well to the 122 keV peak from ^{57}Co while the average energy of a 120 kVp beam corresponds closely to the 59.5 keV peak from ^{241}Am. Each was measured at 90° and 30° angles of incidence. A tungsten collimator with 1 mm diameter opening was used to collimate the ^{57}Co source. The low activity of the ^{241}Am source required a wider collimation of 3 mm, which was done with lead. Peak-to-total ratios were determined to quantify low energy tailing of the spectra, with the peak energy window set to 10% of the peak maximum.

- **X-ray measurements/simulations**

The x-ray source used in this study was a model A-142 x-ray tube with rotating W-anode and 10° target angle powered by a high-frequency generator (Varian Medical Systems). The tube was capable of voltages between 40 and 120 kVp and tube currents between 0.5 and 2.5 mA. Figure 5.4 shows a schematic of the x-ray set-up. The inherent filtration of the system was 2 mm Al and an additional Al plate was permanently mounted to the output of the source. Acrylic was also added between the beam and detector. The half value layer (HVL) at 120 kVp was 6.75 mm Al. The beam was collimated near the detector with Pb having a hole with diameter of 0.5 mm. The detectors were mounted to a stage which could be moved by submillimeter steps in the plane perpendicular to the x-ray beam. This helped ensure that the beam was incident on the center of the detector.

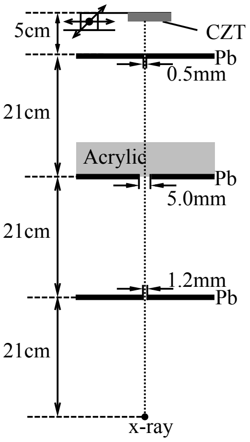

Figure 5.4 Schematic of the x-ray system with acrylic filter and lead collimators used for x-ray spectroscopy.

Although the lowest current setting of 0.5 mA was used for the 120 kVp beam, the count rate was still too high, creating a large dead time, so that further filtration was required. Acrylic sheets were used to reduce counts, with thicknesses 5, 5, and 10 cm for 60, 80, and 120 kVp beams, respectively. Each detector measured 60, 80, and 120 kVp beams at normal incidence and at a tilt angle of 30º between beam and detector surface.

Simulations were performed using a program called SpekCalc [5]. An unfiltered beam with 10º anode angle and appropriate kVp was obtained from the program for each beam energy measured. The appropriate acrylic and aluminum filtration was then added to the simulated beam, corresponding to experimental parameters. Under tilted angle irradiation the beam passes through a greater thickness of the Al present at the detector surface and this increased thickness was taken into account in the simulations.

After filtering, the simulated beam was then convolved with a Gaussian kernel to include statistical and electronic noise. The FWHM of the full energy peak of ^{241}Am isotope measurement with the capacitive grid detector in tilted angle mode was used to determine the width of the kernel. The low energy (59.5 keV) with the capacitive grid detector at 30º results in very little tailing and therefore this width can be assumed to be approximately due only to statistical and electronic noise.

5.1.3 Correcting for K x-ray Escape

Monte Carlo simulations were performed to determine characteristic escape fractions from the incident surface of the detector. These escape fractions were then applied to measured x-ray spectra to correct for K x-ray escape. Both codes were written in IDL and can be found in Appendix C.

- **K x-ray back escape fractions**

The process to determine K x-ray escape fractions is similar to previous code written for a pixelated CZT detector, described in Chapter 3. The exceptions are that 1) instead of choosing five energy bins, energy was sampled in 1 keV intervals from 20 to 120 keV and 2) only back escape was considered. Back escape from Cd and Te were tracked independently so that the proper escape energy would be known, since the K x-rays from Cd and Te each have different energies. The code was also run where the average K x-ray energy of Cd and Te was used, 25 keV, and this proved to give similar results when correcting x-ray spectra as tracking them independently. However, since independent tracking is not difficult this method was chosen to correct spectra to be as accurate as possible.

It was assumed that forward and lateral escapes are negligible based on findings from the previous code. As a result, the azimuthal angles of the K x-rays from Cd and Te were not calculated, and the coordinates of reabsorption were not recorded. The simplified flowchart for the back escape code is shown in Figure 5.5. At each primary energy value, E_0, 10^5 primary photons were simulated. Once the K escape fractions were known they could be applied to make corrections to the measured spectra.

- **Correcting x-ray spectra**

The true number of photons that interact with energy E_0 include those which are fully absorbed and those which are lost due to K escape (neglecting scatter as we do here). The K escape fractions can be used to determine the number of lost counts. A separate code was written in which the measured spectra could be uploaded, after having been interpolated to an energy step size of 1 keV. The corrections for K-x-ray escape were made beginning with the highest energy value, E_{max}, e.g., 120 keV for 120 kVp x-ray spectra. At E_{max}, the number of counts measured is assumed to be only due to the full absorption of primary photons with energy E_{max}. The true number of counts, however, is the measured counts plus counts lost due to K escape. These counts are shifted to lower energies, specifically $E_{max} - E_k$, where E_k is the energy of the K x-ray.

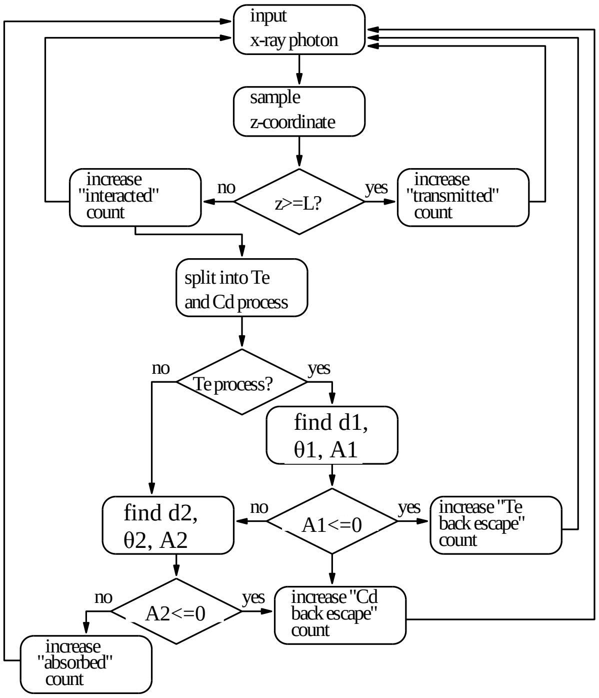

Figure 5.5 Flowchart of the Monte Carlo simulations for tracking back escape of K x-rays from the front surface of the CZT detector.

Using the escape fraction values generated previously, we were able to determine the number of counts lost. The measured counts were then increased by this amount. The general expression for true counts is given by

$$N_t(E_0) = N_d(E_0) + N_s(E_0) - N_s(E) \tag{5.1}$$

Here, $N_t(E_0)$ is the true number of photons with energy E_0 that interact by photoelectric effect in the detector, $N_d(E_0)$ is the number of detected photons with energy E_0, $N_s(E_0)$ is the number of photons with energy E_0 shifted to energy $E_0 - E_k$ due to characteristic K x-ray escape, $N_s(E)$ is the number of photons incorrectly detected with energy E_0shifted from the true number of photons $N_t(E)$ with energies $E = E_0 + E_k$. For $E_0 = E_{max}$, $N_s(E) = 0$, since no counts are shifted from higher energies. In that case, the number of true counts is given by

$$N_t(E_0) = \frac{N_d(E_0)}{1 - f(E_0)} \tag{5.2}$$

Here, $f(E_0) = \frac{N_s(E_0)}{N_t(E_0)}$ is the fraction of true photon interactions with energy E_0 that result in K x-ray escape and is determined from the Monte Carlo simulation discussed previously.

To properly use the above expressions, the correction process must begin with counts at the peak voltage, E_{max}, to ensure that $N_t(E_0)$ is determined correctly. Values for $E_0 + E_k$ greater than E_{max} do not include counts that have been shifted from higher energies. Once N_t is determined at higher energies, we know N_s, the correct amount to reduce counts at lower energies where $E_0 + E_k$ is less than E_{max}. The number of true counts with full absorption, N_d, can then be calculated. Treating each energy bin, in 1 keV steps, from E_{max} down to the lowest measured energies, allows us to properly use this correction technique. The measured spectrum is corrected using

$$N_t(E_0) = [N_d(E_0) - N_s^{Te}(E_{Te}) - N_s^{Cd}(E_{Cd})] \times [1 - f_{Cd}(E_0) - f_{Te}(E_0)]^{-1} \tag{5.3}$$

In this case, E_{Te} and E_{Cd} are given by

$$\begin{gathered} E_{Te} = E_0 + 27keV \\ E_{Cd} = E_0 + 23keV \end{gathered} \tag{5.4}$$

and are the energies shifted from E_0 by the average K x-ray energies for Cd and Te, respectively.

The value of $N_s^{Te,Cd}\left(E_{Te,Cd}\right)$ represents counts from higher energies shifted energies from E_0 by the K x-ray energies for Cd and Te, respectively. This value is dependent on whether $E_{Te,Cd}$ is greater than or less than E_{max}, as expressed by

$$\begin{aligned} N_s^{Te,Cd}\left(E_{Te,Cd}\right) &= 0 && \text{for } E_{Te,Cd} > E_{max} \\ N_s^{Te,Cd}\left(E_{Te,Cd}\right) &= f_{Te,Cd}\left(E_{Te,Cd}\right)N_t && \text{for } E_{Te,Cd} < E_{max} \end{aligned} \tag{5.5}$$

5.1.4 Evaluating Corrected Spectra

Differential and integral deviations between corrected x-ray spectra and simulated spectra were used as quantitative criteria to characterize the accuracy of the spectroscopy method with escape corrections. The differential deviation represents point-by-point deviation of the measured and simulated spectra, while the integral deviation represents a single number specific to a pair of measured and simulated spectra and takes into account deviations that occur at all energy points.

The differential deviation, D(E),between two spectra was determined at a given energy value, E, between the measured spectrum corrected for K x-ray escape and the simulated spectrum and was calculated using

$$D(E) = \frac{N_{corr}(E) - N_{sim}(E)}{[N_{corr}(E) + N_{sim}(E)]/2} \tag{5.6}$$

The term $N_{corr}(E)$ is the number of counts measured with energy E after correcting for K escape and $N_{sim}(E)$ is the number of counts simulated with energy E. Values of D(E) at or near zero indicate that the corrected measurement and simulation agree well with one another.

The integral deviation, I, was determined according to

$$I = \frac{\sqrt{\sum_{E_{min}}^{E_{max}}[N_{corr}(E) - N_{sim}(E)]^2/N_{energies}}}{\langle N_{counts}\rangle} \tag{5.7}$$

The term $N_{energies}$ is the number of points in the energy range from E_{min} to E_{max}. The value in the denominator is the average number of counts and is given by

$$\langle N_{counts} \rangle = \frac{\sum_{E_{min}}^{E_{max}} [N_{corr}(E) + N_{sim}(E)]/2}{N_{energies}} \tag{5.8}$$

5.2 Results of Measurements and Corrections

- **Isotope sources**

Results of isotope measurements are shown in Figure 5.6 and Figure 5.7. Measurements with both the planar detector and capacitive grid detector are shown for normal and tilted angle irradiation. Results from the ^{57}Co source are shown in Figure 5.6 for (a) 90° and (b) 30° irradiation angles. It is clear from Figure 5.6 (a) that the planar detector at normal irradiation results in significant tailing of the energy spectrum. This tailing is reduced with the capacitive grid detector under normal irradiation. In Figure 5.6 (b) it is clear that the energy spectrum for the planar detector is improved for tilted angle irradiation, however, there is virtually no tailing using the capacitive grid detector at 30° tilt angle.

Results from the ^{241}Am source are shown in Figure 5.7. The improvement in low energy tailing for the planar detector from (a) 90° to (b) 30° angles of irradiation is not as evident for this source. This is because the lower energy of the source means that most interactions take place near the surface even under normal irradiation. However, the improvement from planar to capacitive grid detector is seen for both irradiation angles.

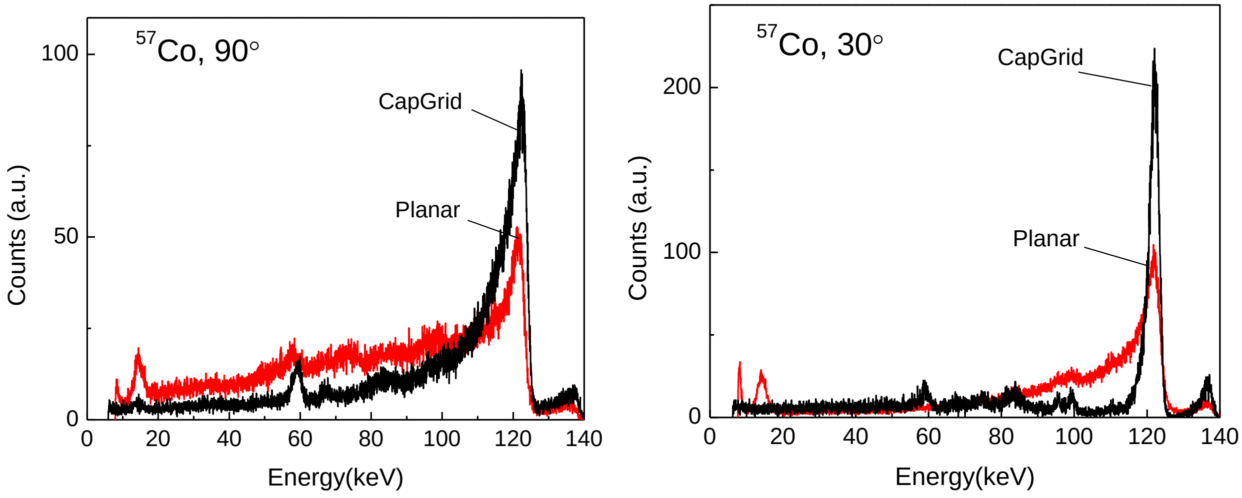

(a) **(b)**

Figure 5.6 Spectra measured with planar and capacitive grid detectors for ^{57}Co (122 keV) at incident angles of (a) 90° and (b) 30°. At 90° incidence heavy tailing is observed, especially for the planar detector. At 30° angle tailing is reduced for the planar detector and nearly eliminated for the capacitive grid detector.

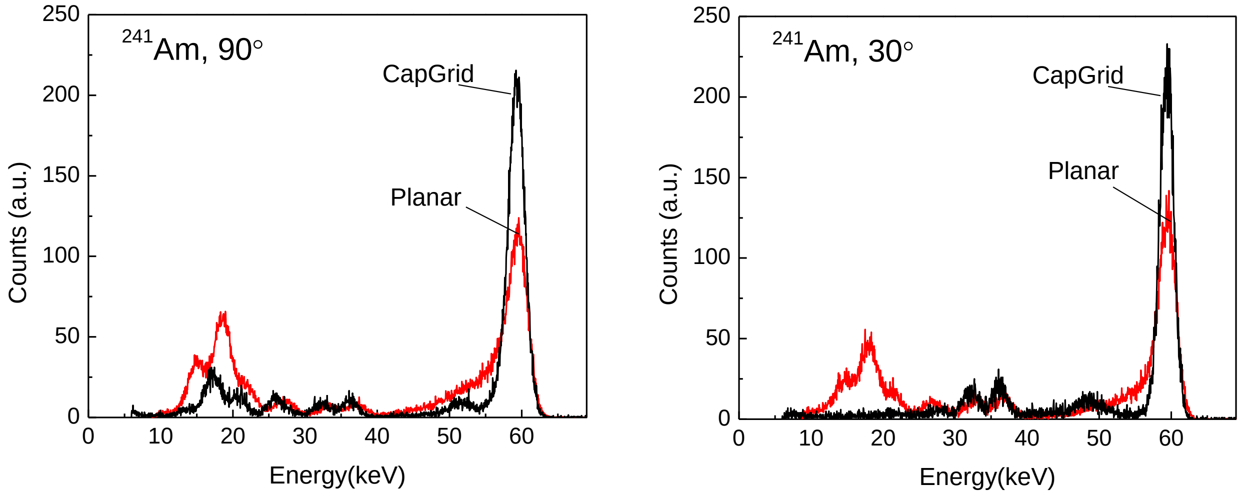

(a) **(b)**

Figure 5.7 Spectra with planar and capacitive grid detectors for ^{241}Am (59.5 keV) at incident angles of (a) 90° and (b) 30°. At 90° incidence some tailing is observed for the planar detector while minimal tailing is seen for the capacitive grid detector. At 30° tilt angle tailing is reduced for the planar detector and eliminated for the capacitive grid detector.

Peak-to-total ratios are given in Table 5.2 and help quantify improvements in tailing using the capacitive grid detector in tilted angle mode. For an ideal detector the peak-to-total ratio is 100%.

Table 5.2 Peak-to-total ratios for isotope measurements (%)

	Planar 90^{o}	CapGrid 90^{o}	Planar 30^{o}	CapGrid 30^{o}
Co-57 (122 keV)	18	32	31	77
Am-241 (59.6 keV)	52	82	62	83

- **X-ray spectra**

Results from x-ray spectra measurements are shown in Figure 5.8 through Figure 5.10. Figure 5.8 shows results for a 120 kVp beam with the planar detector in normal (a) and tilted angle (b) irradiation modes. For energies above ~60 keV the measured counts are much lower than the simulated counts for normal irradiation. These high energy counts are shifted to lower energies, especially evident in the blurring of the shoulder around 60 keV. The tailing effect decreases for tilted angle irradiation, but is still visible.

The capacitive grid detector measurements are shown in (c) and (d) of Figure 5.8. The normal irradiation of the capacitive grid detector in Figure 5.8 (c) shows a tailing effect similar to the tilted angle irradiation effect of the planar detector. The best improvement, however, is seen in Figure 5.8 (d) where almost no tailing can be observed for tilted angle irradiation of the capacitive grid detector. The presence of counts in the energy range below ~30 keV is accounted for using the K x-ray escape corrections.

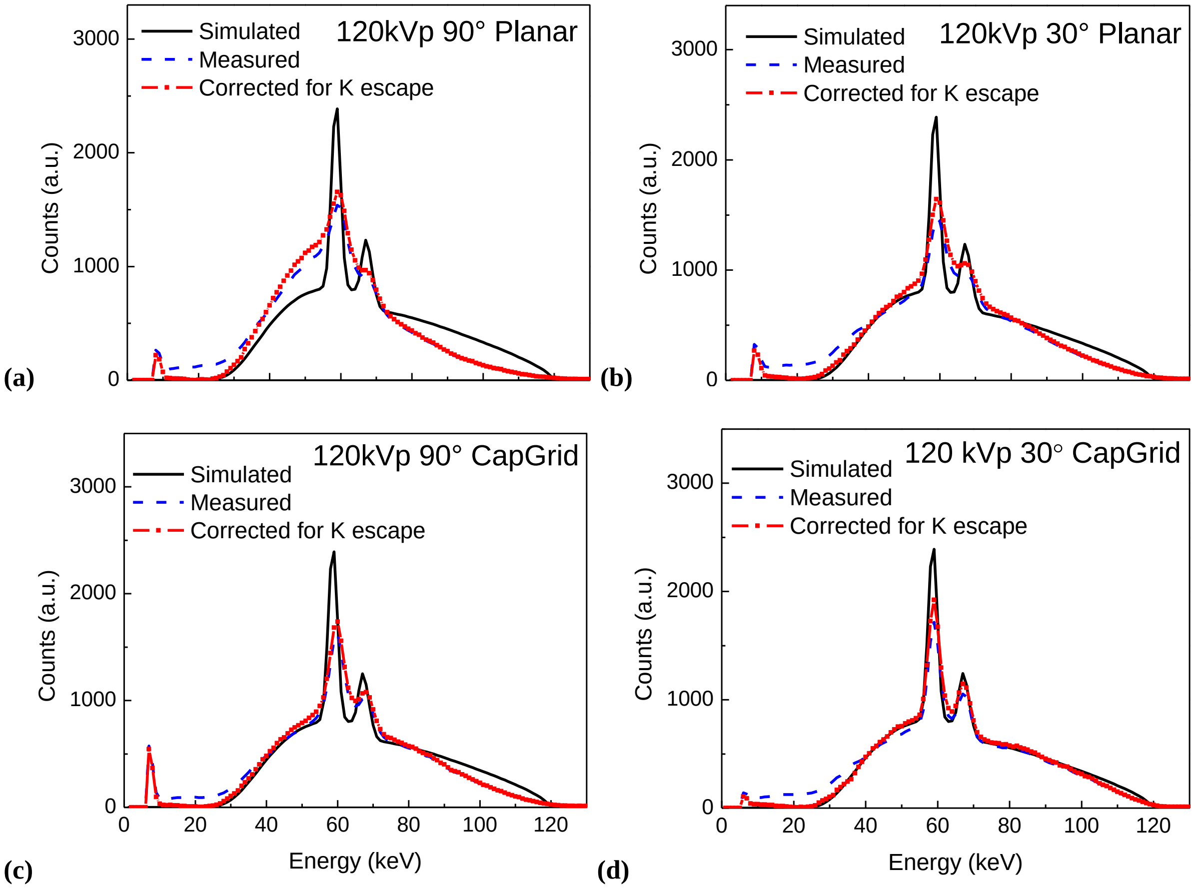

Figure 5.8 Measured, corrected, and simulated 120 kVp spectra. Results with (a, b) planar and (c, d) capacitive grid CZT detectors are presented for (a, c) 90º and (b, d) 30º irradiation angles.

Results for 80 kVp x-ray measurements are shown in Figure 5.9. Again, measured counts in the region above 60 keV are suppressed compared to simulation for the planar detector under normal irradiation Figure 5.9 (a). Results for the planar detector at 30º tilt angle in Figure 5.9 (b) and the capacitive grid detector under normal irradiation in Figure 5.9 (c) are similar. There is tailing due to hole trapping compared to the planar detector under normal irradiation. The best result is for the capacitive grid detector at 30º tilt angle, shown in Figure 5.9 (d). The correction for K x-ray escape effectively removes low energy counts and restores them to the higher region.

The 60 kVp results shown in Figure 5.10 suffer less severely from hole trapping effects, even for the planar detector under normal irradiation shown in Figure 5.10 (a). Slight improvements are evident using the planar detector at 30º tilt angle in Figure 5.10 (b) and the capacitive grid detector under both normal, Figure 5.10 (c), and tilted angle, Figure 5.10(d), irradiation incidences. The major effect seen for the 60 kVp beams is that most interactions take place near the surface, regardless of incident angle, and therefore a greater amount of K x-ray escape occurs. This escape is sufficiently accounted for using our correction method.

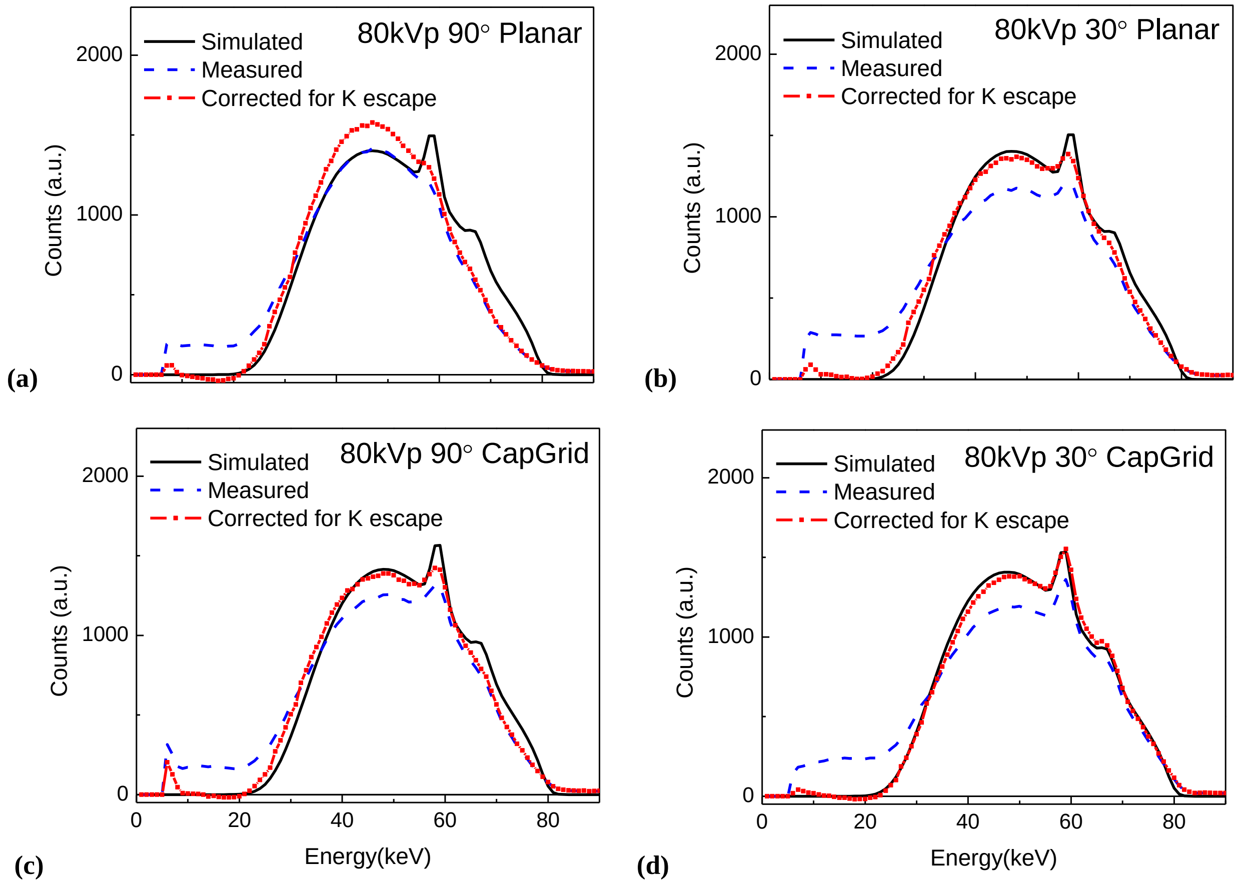

Figure 5.9 Measured, corrected, and simulated 80kVp spectra. Results with (a, b) planar and (c, d) capacitive grid CZT detectors are presented for (a, c) 90° and (b, d) 30° irradiation angles.

The overall results of the x-ray measurements are shown in the differential deviations in Figure 5.11 and the integral deviations in Table 5.3. The differential deviations for 60 kVp results, Figure 5.11 (a), all fall near zero, indicating good agreement with simulation in each case. This conclusion is further justified in the small integral deviation values in Table 5.3. The 80 kVp results, Figure 5.11 (b), show that the least deviation from simulation occurs for the capacitive grid detector in tilted angle mode. The same is true for the 120 kVp results, Figure 5.11 (c).

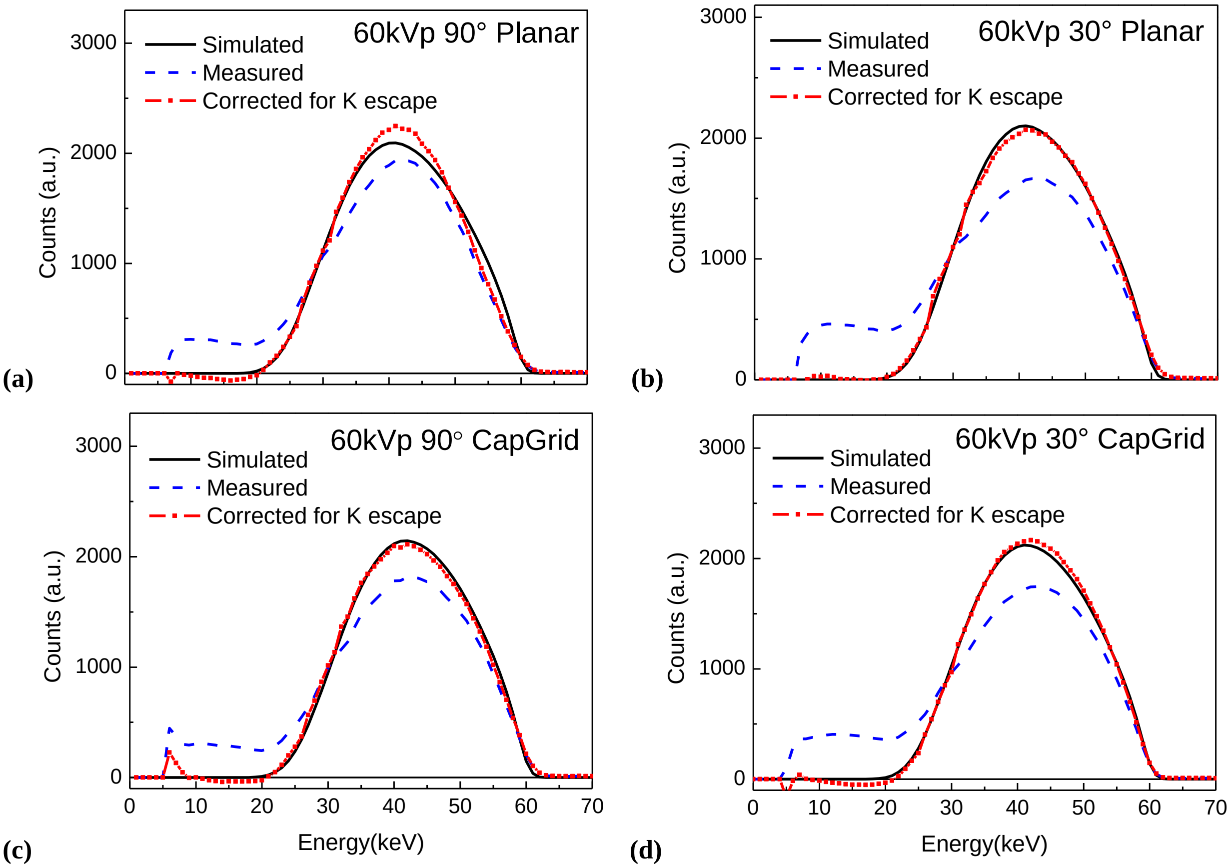

Figure 5.10 Measured, corrected, and simulated 60 kVp spectra. Results with (a, b) planar and (c, d) capacitive grid CZT detectors are presented for (a, c) 90º and (b, d) 30º irradiation angles.

5.3 Conclusions and Advantages of Tilted Angle Irradiation with a Capacitive Grid Detector

The benefits of a CZT detector for diagnostic x-ray spectroscopy have been inhibited due to low energy tailing as a result of hole trapping. We showed that modifying the interaction depth using tilted angle irradiation offers similar improvements to modifying the electric field with the capacitive grid detector. We combined these two physical methods of improving spectral tailing by using the capacitive grid detector in tilted angle irradiation. We showed that this combination effectively eliminates hole trapping effects for energies up to 120 kVp if corrections are done form K x-ray escape.

Our x-ray system was not capable of beam energies larger than 120 kVp, although some diagnostic applications such as chest x-ray use energies up to 140 kVp. At this higher energy Compton scatter increases and may become significant. Further study is needed to determine whether it is necessary to account for Compton scatter at energies above 120 kVp. For our purposes a tilt angle of 30 sufficiently modified the depth of interaction to decrease low energy tailing. However, higher energies may require further decrease in tilt angle as interaction depth increase.

The capacitive grid detector used here was designed for normal irradiation of high energy gamma rays. To optimize the detector for tilted angle operation of low energy diagnostic x-rays it may be necessary to adjust certain parameters including geometry of the CZT crystal, length of cathode extension, and operating voltage. The x-ray beam should also be optimized by proper collimation to decrease dead time when x-ray flux is high.

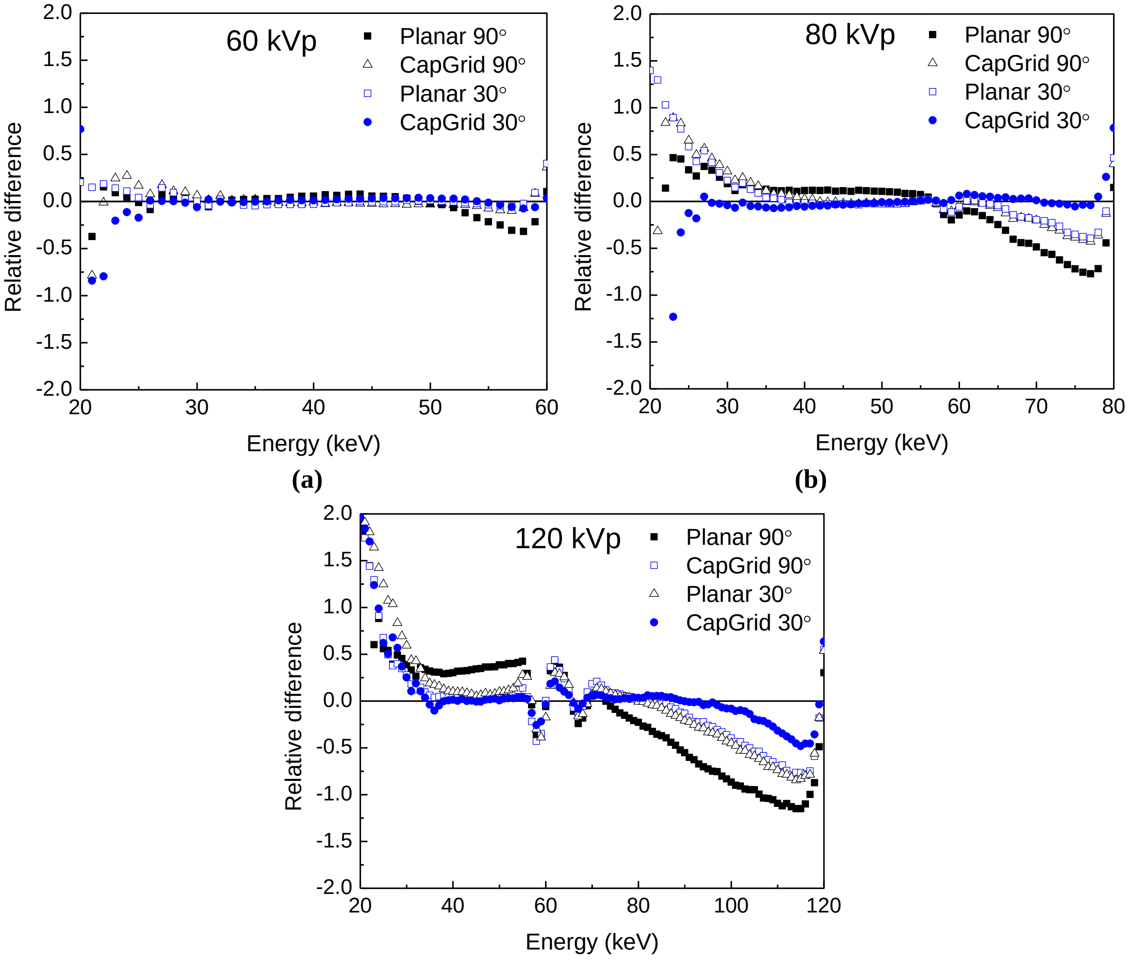

(a)

(b)

(c)

Figure 5.11 Differential deviations between measured spectra after K escape corrections and simulated spectra at (a) 60 kVp, (b) 80 kVp, and (c) 120 kVp tube voltages.

Table 5.3 Integral deviation of x-ray spectra (%)

	Planar 90°	CapGrid 90°	Planar 30°	CapGrid 30°
60 kVp	10	6.6	4.2	5.0
80 kVp	22	13	11	5.5
120 kVp	47	36	32	19

LITERATURE CITED

1. J.T. Bushberg , J. A. Seibert, E. M. Leidholdt, Jr., J. M. Boone, *The Essential Physics of Medical Imaging*. 2nd ed. (Lippincott Williams & Wilkins, Philadelphia, 2002)

2. P.M. Shikhaliev, "Computed Tomography with Energy-resolved Detection: a Feasibility Study," Phys. Med. Biol. **53**(5) 1475-95, 2008.

3. P.M. Shikhaliev, "Energy-resolved Computed Tomography: First Experimental Results," Phys. Med. Biol. **53**(20), 5595-613, 2008.

4. M. Overdick, *et al*. "Towards Direct Conversion Detectors for Medical Imaging with X-rays," in *IEEE Nuc. Sci. Symp. Conf. Rec.*, Dresden, Germany 2008.

5. G. Poludniowski, *et al*., "SpekCalc: A Program to Calculate Photon Spectra from Tungsten Anode X-ray Tubes," Phys. Med. Biol. **54**(19) N433-N438, 2009.

6. S. Webb, *The Physics of Medical Imaging*. (Medical science series., Bristol ; Philadelphia, 1988).

7. Z.H. Cho, J.P. Jones, M. Singh, *Foundations of Medical Imaging*. (Wiley, New York, 1993).

8. J. Beutel, *Handbook of Medical Imaging*. (SPIE Press Bellingham, Wash., 2000).

9. P.C. Johns and M.J. Yaffe, "X-ray Characterisation of Normal and Neoplastic Breast Ttissues," Phys. Med. Biol. **32**(6) 675-95, 1987.

10. M.J. Horner, *et al*. (eds). *SEER Cancer Statistics Review, 1975-2006* (National Cancer Institute, Bethesda, MD, 2009).

11. S.J. Glick, "Breast CT," Annual Review of Biomedical Engineering **9** 501-26, 2007.

12. J.S. Michaelson, *et al*., "Predicting the Survival of Patients with Breast Carcinoma Using Tumor Size," Cancer **95**(4) 713-23, 2002.

13. Smith, R.A., *et al*., "Cancer Screening in the United States, 2010 A Review of Current American Cancer Society Guidelines and Issues in Cancer Screening," CA: A Cancer Journal for Clinicians **60**(2) 99-119, 2010.

14. G.F. Knoll, *Radiation Detection and Measurement*. 3rd ed. (Wiley, New York, 2000).

15. M.J. Tapiovaara R.F. Wagner, "SNR and DQE Analysis of Broad-Spectrum X-Ray-Imaging," Phys. Med. Biol. **30**(6) 519-29, 1985.

16. K. Iniewski, *Medical Imaging: Principles, Detectors, and Electronics*. (Wiley, Hoboken, N.J., 2009).

17. P.M. Shikhaliev, "Tilted Angle CZT Detector for Photon Counting/Energy Weighting X-ray and CT Imaging," Phys. Med. Biol. **51**(17) 4267-87, 2006.

18. S.J. Thunberg, *et al*., "Dose Reduction in Mammography with Photon Counting Imaging," Proceedings SPIE **5368**(457), 2004.

19. H.H. Barrett, J.D. Eskin, H.B. Barber, "Charge Transport in Arrays of Semiconductor Gamma-ray Detectors," Phys. Rev. Lett. **75**(1) 156-59, 1995.

20. J.D. Eskin, H.H. Barrett, H.B. Barber, "Signals Induced in Semiconductor Gamma-ray Imaging Detectors," J. App. Phys. **85**(2) 647-59, 1999.

21. W. Shockley, "Currents to Conductors Induced by a Moving Point Charge," J. App. Phys. **9** 635-36, 1938.

22. S. Ramo, "Currents Induced by Electron Motion," in *Proceedings of the Institute of Radio Engineers*, 1939.

23. P.R. Bennett, *et al*., "Evaluation of CdTe for Use in a Prototype Emission/Transmission CT Imaging System," IEEE Trans. Nuc.Sci. **43**(4) 2225-29, 1996.

24. M. Aslund, *et al*., "Scatter Rejection in Multislit Digital Mammography," Med. Phys. **33**(4) 933-40, 2006.

25. P.M. Shikhaliev, *et al*., "Scanning-slit Photon Counting X-ray Imaging System Using a Microchannel Plate Detector," Med. Phys. **31**(5) 1061-71, 2004.

26. P.M. Shikhaliev, S.G. Fritz, J.W. Chapman,"Photon Counting Multienergy X-ray Imaging: Effect of the Characteristic X-rays on Detector Performance," Med. Phys. **36**(11) 5107-19, 2009.

27. *Semiconductor Detector Material Properties*. 2009; Available from: http://www.evmicroelectronics.com/pdf/material_prop.pdf.

28. K. Hecht, "Zum Mechanismus des lichtelektrischen Primärstromes in isolierenden Kristallen," Zeitschrift für Physik A Hadrons and Nuclei **77**(3-4) 235-45, 1932.

29. W. Akutagaw and K. Zanio, "Gamma Response of Semi-Insulating Material in Presence of Trapping and Detrapping," J. App. Phys. **40**(9) 3838, 1969.

30. S.G. Fritz and P.M. Shikhaliev, "CZT Detectors Used in Different Irradiation Geometries: Simulations and Experimental Results," Med.Phys. **36**(4) 1098-108, 2009.

31. M. Lundqvist, *et al*. "Computer Simulations and Performance Measurements on a Silicon Strip Detector for Edge-on Imaging," in *IEEE Nucl. Sci. Symp. Conf. Rec.*, Seattle, WA, 1999.

32. H.-E. Nilsson, C. Fröjdh, E. Dubaric, "Monte Carlo Simulation of Charge Sharing Effects in Silicon and GaAs Photon-Counting X-Ray Imaging Detectors," IEEE Trans. Nuc. Sci. **51**(4) 1636-40, 2004.

33. H.-E. Nilsson, *et al.*, "Charge Sharing Suppression Using Pixel-to-Pixel Communication in Photon Counting X-ray Imaging Systems," Nuc. Inst. Met. Phys. Res. A **576** 243-47, 2007.

34. B. Norlin, C. Fröjdh, H.-E. Nilsson, "Spectral Performance of a Pixellated X-ray Imaging Detector with Suppressed Charge Sharing," Nuc. Inst. Met. Phys. Res. A **576** 248-50, 2007.

35. C.M.H. Chen, *et al.*, "Numerical Modeling of Charge Sharing in CdZnTe Pixel Detectors," IEEE Trans. Nuc. Sci. **49**(1) 270-76, 2002.

36. G. Pellegrini, *et al.*, "Performance Limits of a 55-μm Pixel CdTe Detector," IEEE Trans. Nuc.Sci. **53**(1) 361-66, 2006.

37. E.G. d'Aillon, *et al.*, "Charge Sharing on Monolithic CdZnTe Gamma-ray Detectors: A Simulation Study," Nuc. Inst. Met. Phys. Res. A **563** 124-127, 2006.

38. K. Iniewski, *et al*. "Modeling Charge-Sharing Effects in Pixellated CZT Detectors," in *IEEE Nuc. Symp. Conf. Rec.*, Honolulu, HI, 2007.

39. I. Kuvvetli and C. Budtz-Jørgensen. "Measurements of Charge Sharing Effects in Pixilated CZT/CdTe Detectors," in *IEEE Nucl. Sci. Symp. Conf. Rec.*, Honolulu, HI, 2007.

40. E. Kalemci and J.L. Matteson, "Investigation of charge sharing among electrode strips for a CdZnTe detector," Nuc. Inst. Met. Phys. Res. A **478** 527-37, 2002.

41. M.J. Berger, *et al*., *XCOM: Photon Cross Sections Database*, NIST, Gaithersburg, MD, 2005.

42. M.O. Krause, "Atomic Radiative and Rationless Yields for K and L Shells," J. Phys. Chem. Ref. Data **8**(2), 1979.

43. M.J. Berger, *et al*., *ESTAR, PSTAR, and ASTAR: Computer Programs for Calculating Stopping-Power and Range Tables for Electrons, Protons, and Helium Ions*, NIST, Gaithersburg, MD, 2005.

44. W.S. Rasband, *ImageJ*, NIH, Bethesda, Maryland 1997-2009.

45. V.B. Cajipe, *et al*. "Multi-energy X-ray Imaging with Linear CZT Pixel Arrays and Integrated Electronics," in *IEEE Nuc. Sci. Symp. Conf. Rec.*, 2004.

46. J.M. Boone, *et al*., "Dedicated breast CT: Radiation Dose and Image Quality Evaluation," Radiology **221**(3) 657-67, 2001.

47. T.R. Fewell, *Handbook of Computed Tomography X-Ray Spectra*, DHHS, Bureau of Radiologic Health, Rockville, Maryland, 1981.

48. S. Miyajima, "Thin CdTe Detector in Diagnostic X-ray Spectroscopy," Med. Phys. **30**(5) 771-77, 2003.

49. M. Matsumoto, *et al.*, "Direct Measurement of Mammographic X-ray Spectra Using a CdZnTe Detector," Med. Phys. **27**(7) 1490-502, 2000.

50. S. Miyajima, K. Imagawa, M. Matsumoto, "CdZnTe Detector in Diagnostic X-ray Spectroscopy," Med. Phys. **29**(7) 1421-29, 2002.

51. G. Montemont, *et al.*, "A Capacitive Frisch Grid Structure for CdZnTe Detectors," IEEE Trans. Nuc. Sci. **48**(3) 278-81, 2001.

52. K. Parnham, *et al*. "Performance Improvement of CdZnTe Detectors Using Modified Two-Terminal Electrode Geometry," in *SPIE Conference on Hard X-Ray, Gamma-Ray and Neutron Detector Physics*, Denver, CO, 1999.

APPENDIX A SIMULATING CZT DETECTOR USING THE HECHT FORMALISM

- **Hecht Theory**

The signal amplitude resulting from an interaction at some depth in a semiconductor detector is related to depth by the Hecht relation:

$$E(z) = \frac{E_0}{L}\left\{\lambda_e\left[1 - exp\left(-\frac{(L-z)}{\lambda_e}\right)\right] + \lambda_h\left[1 - exp\left(-\frac{z}{\lambda_h}\right)\right]\right\} \tag{A.1}$$

where:

E_0= energy of the incident photon

L = thickness of the detector

z = distance from incident surface where interaction takes place, and

λ_e, λ_h = mean free drift lengths of electrons and holes, respectively.

Figure A.1 shows the basic process of photon interaction in a semiconductor crystal. An electric field is applied in the detector. The photon is incident at some angle α with respect to the detector surface, usually the cathode side of the detector.

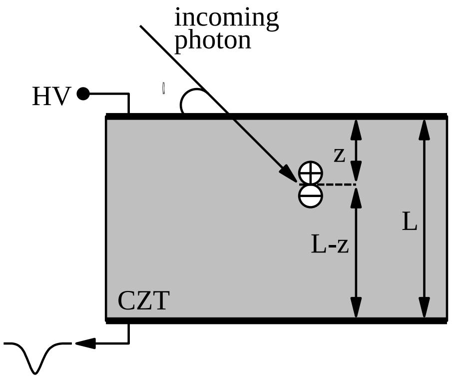

Figure A.1 Schematic of electron-hole pair generation due to photon incident at angle α with respect to CZT surface. The thickness of the CZT is *L* and holes and electrons travel a distance of *z* and *L-z*, respectively, as they drift toward their respective electrodes.

- **Simulating the energy spectrum**

Simulation of the energy spectrum was done using Origin 7.0 graphing software. The differential number of pulses, dN, within an energy increment, dE, was determined for various energies of incident photons under different irradiation geometries. The following steps were taken to simulate the spectrum:

1. Numerically solve for the inverse of equation (A.1) to find z(E).
   a. Because z(E) is a multi-valued expression, E(z) was first split into two curves, a long curve labeled ‘A’ and a short curve labeled ‘B’, shown in Figure A.2.
2. The inverse of each curve was then plotted and the derivative of was determined, dz/dE.
3. The product of the derivative and the differential of the photon intensity was calculated, $\frac{dN}{dE} = \frac{dN}{dz}\frac{dz}{dE}$. Values $\frac{dN}{dz}$ were determined using the appropriate geometry of the simulation and μ(E) for the simulated energy, E_0.
4. The resulting product was plotted and interpolated to achieve a step size for E/E_0 of 1×10^{-6}.
5. The two curves were then summed for corresponding values of E/E_0. The result is the final theoretical spectrum without noise.
6. The final spectrum was convolved with a Gaussian kernel. The sigma of the kernel accounted for statistical and electronic noise.
7. Values of E/E_0 were then scaled for the appropriate simulated energy, E_0, by $E_i = \left(\frac{E}{E_0}\right)_i \times E_0 \Big/ \left(\frac{E}{E_0}\right)_{dN/dE_{max}}$.

- **Hecht Inverse**

A dataset of z and E/E_0 values with $\Delta z = 0.001$ mm was created using equation (A.1). Two values of z in the range 0 to z_k may correspond to the same E/E_0 value, see Figure A.2. The maximum of E/E_0 was determined and here the dataset was split into sets A and B.

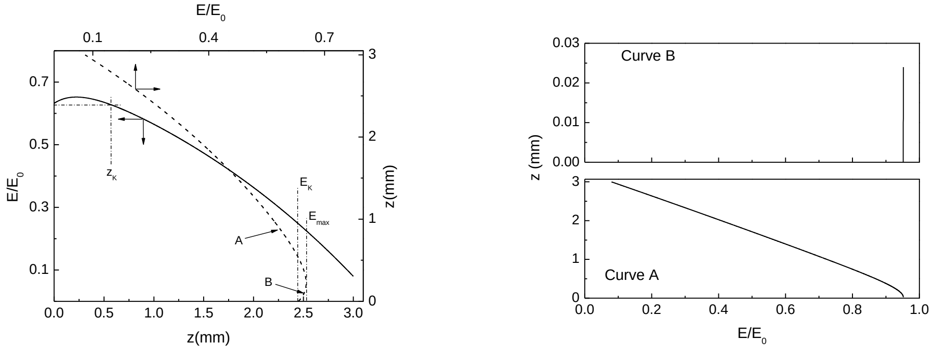

Figure A.2 Plot of the Hecht relation E(z) and its inverse z(E), left. It was necessary to split z(E) into two separate curves, labeled A and B, since it is a multi-valued expression, right.

- **Hecht Inverse differentiation**

Each curve was then differentiated using Origin software. A screen shot of this step is shown in Figure A.3, left. The resulting differentiated curves are shown in Figure A.3, right.

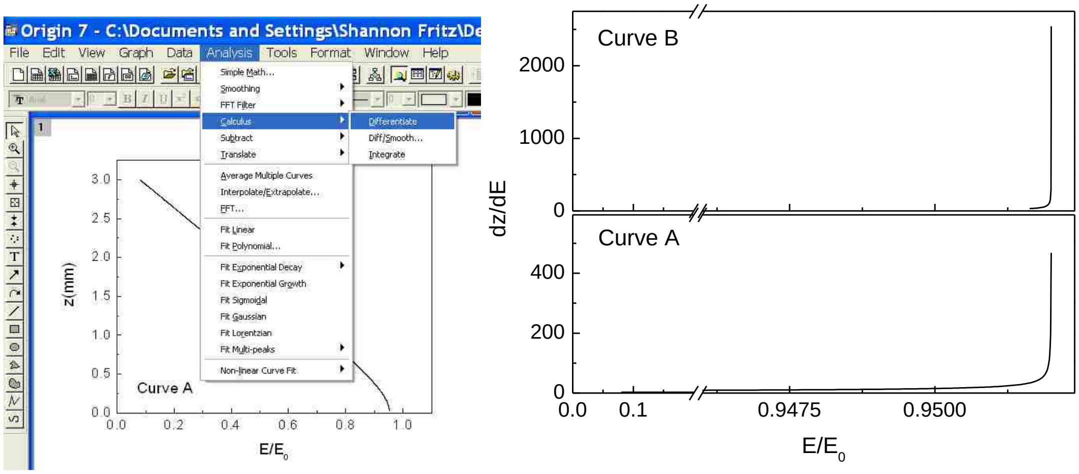

Figure A.3 Screen shot of the differentiation of a curve in Origin 7, left, and the result of differentiating curves A and B.

- **Product of dN/dz and dz/dE**

A dataset of dN/dz was generated using appropriate the appropriate μ(E) and expression for the energy and geometry to be simulated, respectively. The product of this dataset and the dz/dE dataset was taken. These curves were interpolated to achieve a step size for E/E_0 of 1×10^{-6}, shown in Figure A.4, left. The resulting dN/dE datasets for curves A and B were then summed and the result is shown in Figure A.4, right.

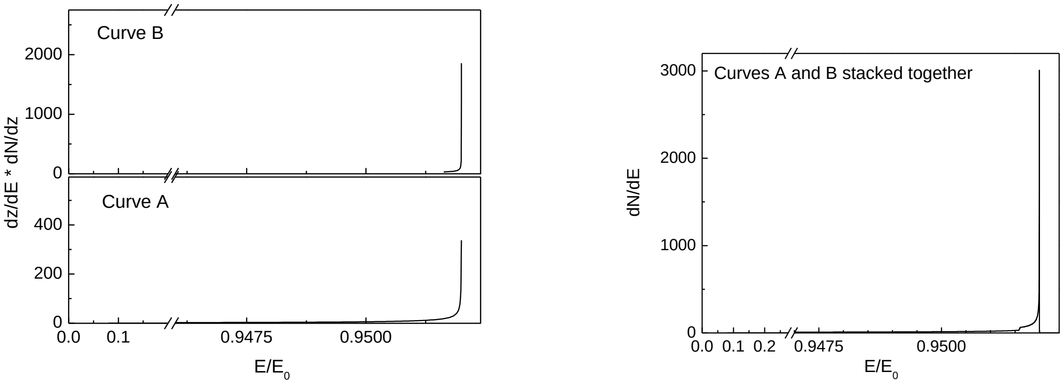

Figure A.4 Plot of the product of dz/dE and dN/dz for each curve, A and B, left. Result of summing curves A and B at each value of E/E_0, right.

- **Convolution of dN/dE**

The following Gaussian expression was used to convolve the theoretical spectrum:

$$G(x) = (2\pi\sigma^2)^{-1/2} exp\left[\frac{-(x-x_0)^2}{2\sigma^2}\right]/\sqrt{2\pi\sigma^2} \tag{A.2}$$

where the parameter x was given the same step size as E/E_0 and centered at zero, $x_0 = 0$. To convolve using the Origin software, the number of values in the dataset G(x), called the response dataset, must be an odd number and result in a symmetrical function. A representative curve is shown in Figure A.5.

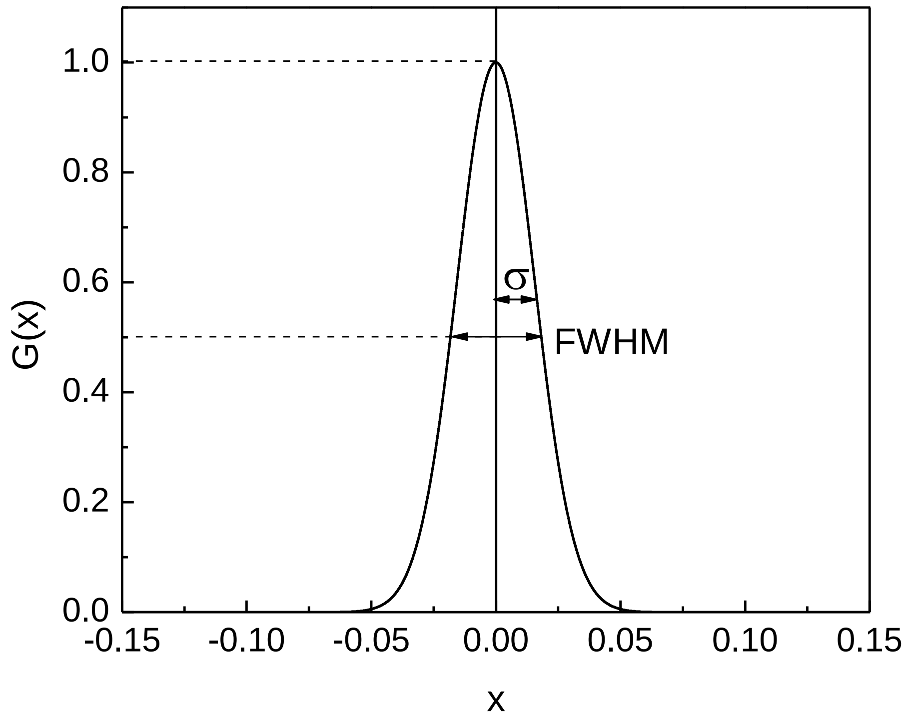

Figure A.5 Representative curve of the convolution kernel used in simulations. To convolve in origin the response curve must be symmetrical with an odd number of data points. The number of points must be less than half that of the signal dataset and it is recommended that the total counts be normalized to one to maintain total counts of the signal dataset.

The response data set must also have fewer than have the number of data points than the signal dataset. It is recommended that the total of the response dataset be normalized to one so that the resulting convolved dataset has the same amplitude as the signal dataset. Figure A.6 shows a screen shot of the convolution step, where the signal and response data set are highlighted when the ‘Convolute’ option is chosen. Note that the signal dataset must be left of the response dataset in the worksheet.

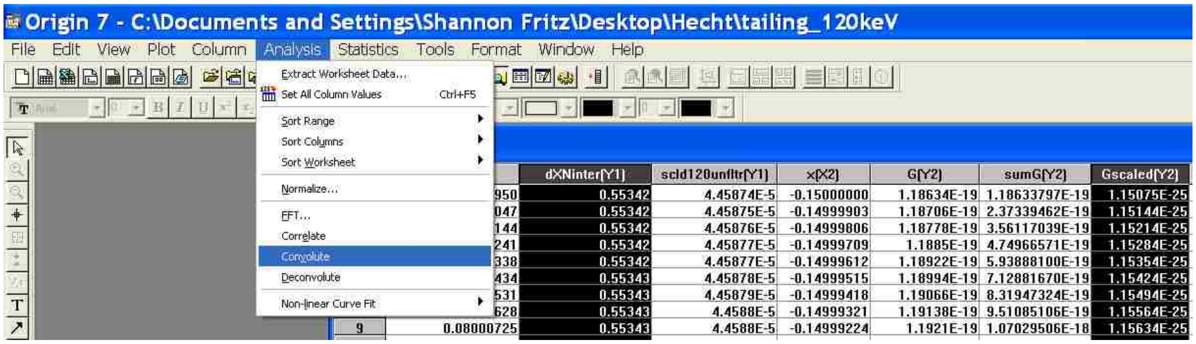

		dXNinter(Y1)	scld120unfltr(Y1)	x(X2)	G(Y2)	sumG(Y2)	Gscaled(Y2)
	950	0.55342	4.45874E-5	-0.15000000	1.18634E-19	1.18633797E-19	1.15075E-25
	047	0.55342	4.45875E-5	-0.14999903	1.18706E-19	2.37339462E-19	1.15144E-25
	144	0.55342	4.45876E-5	-0.14999806	1.18778E-19	3.56117039E-19	1.15214E-25
	241	0.55342	4.45877E-5	-0.14999709	1.1885E-19	4.74966571E-19	1.15284E-25
	338	0.55342	4.45877E-5	-0.14999612	1.18922E-19	5.93888100E-19	1.15354E-25
	434	0.55343	4.45878E-5	-0.14999515	1.18994E-19	7.12881670E-19	1.15424E-25
	531	0.55343	4.45879E-5	-0.14999418	1.19066E-19	8.31947324E-19	1.15494E-25
	628	0.55343	4.4588E-5	-0.14999321	1.19138E-19	9.51085106E-19	1.15564E-25
9	0.08000725	0.55343	4.4588E-5	-0.14999224	1.1921E-19	1.07029506E-18	1.15634E-25

Figure A.6 Screen shot of convolution using Origin software. The signal dataset is to the left of the response dataset in the worksheet and both are highlighted when the 'Convolute' option is chosen.

The final step is to scale the E/E$_0$ dataset for the appropriate energy simulated when $\mu(E)$ values were chosen. The resulting curve is shown in Figure A.7.

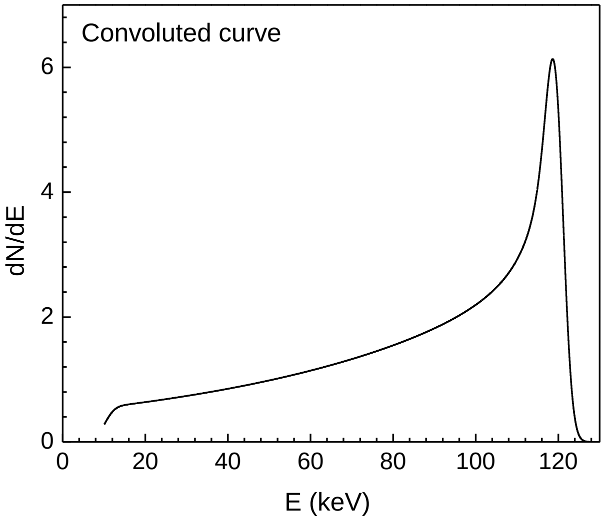

Figure A.7 The final result of the theoretical spectrum convolved for noise, with the energy scaled to simulate the appropriate value of E0, in this case 120 keV.

APPENDIX B MONTE CARLO SIMULATIONS OF K X-RAY ESCAPE FRACTIONS

The following code was written using Interactive Data Language (IDL) to simulate escape of characteristic x-rays from the K shells of Cd and Te of a CZT detector. This example simulates monoenergetic photons incident on a 1 mm square pixel. Chapter 3 gives details about the equations used for calculations used in the code.

The input energy is chosen by the user in the form of the appropriate attenuation length of photons for the desired energy in CZT. These values were found taken from NIST. A separate code was written for each pixel size and orientation, whether square or strip. The pixel size is taken into account in lines 109 and 111, where dx and dy can be varied according to the desired size of the pixel. For strip pixels, dy was allowed to vary across the entire length of the detector in the y-direction. However, the pixel dimensions could easily be incorporated into a single code and prompt the user for desired pixel shape and size.

The output of the code consists of three data files and one image file. The first data file contains results of the counters for transmitted and full absorption incident photons as well as back escape, forward escape, and side escape of characteristic x-rays. These values are also printed in the program console at the conclusion of the run for immediate confirmation that the code is running properly. The other two files are the depth profiles for initial interaction of the incident photon, labeled G, and complete absorption of the incident photon with x-ray escape, labeled K. These profiles are also plotted by the program and appear immediately upon completion of the run. The image file is a TIFF file of the position of final x-ray absorption and also appears in a window once the code is done running. The code simulates 20 million incident photons and takes only a few minutes to run.

```
1     PROSqrPxl_1mm
2
3     N = 20E6
4     Eo = ''
5     read, 'Enter energy (keV) of incident photon:  ', Eo
6     t1 = ''
7     read, 'Enter the attenuation length (um) of incident photon:  ', t1
8     angle = ''
```

```
read, 'Enter the angle (degrees) between the incoming photon beam and the detector surface:  ',angle
theta = angle * !PI / 180

;create sets of random numbers
R1 = RANDOMU(seed,N)       ;sample interaction length of incoming photon
RTeCd = RANDOMU(seed,N)
R2 = RANDOMU(seed,N)       ;sample interaction length of Te K x-ray
R3 = RANDOMU(seed,N)       ;sample cosine of Te K x-ray
R4 = RANDOMU(seed,N)       ;sample azimuthal angle of Te K x-ray
R5 = RANDOMU(seed,N)       ;sample interaction length of Cd K x-ray
R6 = RANDOMU(seed,N)       ;sample cosine of Cd K x-ray
R7 = RANDOMU(seed,N)       ;sample spread in x-direction
R8 = RANDOMU(seed,N)       ;sample spread in y-direction
R9 = RANDOMU(seed,N)

tTe = 64;attenuation length(um) of Te x-ray in CZT
tCd = 116;attenuation length(um) of Cd x-ray in CZT
L = 3000;detector length(um)
b = 0.1;scaling factor...pixels per micron

S = DBLARR(850,850);array of full absorption position
G = FLTARR(b*L+1)  ;position of incident photon initial interaction along
        ;z-axis
K = FLTARR(b*L+1)  ;position of char x-ray absorption along z-axis for
        ;full absorption

;define counters
transmitted = 0.
kback = 0.
kforward = 0.
kside = 0.
kabsorbed = 0.

;call up table of relative values for initial interaction
;with Cd or Te with respect to energy
file = 'C:\Documents and Settings\Shannon Fritz\Desktop\MonteCarlo_IDL\IDL\Cd and CdTe ratios.txt'
OPENR, lun, file, /GET_LUN
   energy = 0.0
   Cd = 0.0
Te = 0.0
   rows = file_lines(file)
   data = FLTARR(rows,3)
FOR i = 0, rows-1DOBEGIN
```

```
READF, lun, energy, Cd, Te
     data[i,0] = energy
     data[i,1] = Cd
     data[i,2] = Te
ENDFOR
FREE_LUN,lun
   data = TRANSPOSE(data)
   i = 0
WHILEEoGT data[0,i] DOBEGIN
      i += 1
ENDWHILE
Te = data[2,i];probability of initial Te interaction

p = 0.;begin with first incident photon, where 'p' counts photons
WHILE (p LT N) DOBEGIN
  z = -t1*SIN(theta)*ALOG(R1[p]) ;interaction position of incident photon
IF (z GE L) THEN transmitted += 1 $
ELSEBEGIN
Lg = b*ROUND(z)
        G(Lg) +=  1;pixel of primary interaction along z-axis
yTe = 0.
M = 0.
Xcoord1 = 0.
Ycoord1 = 0.
A1 = 0.
IFRTeCd[p] LETeTHENBEGIN
yTe = -tTe*ALOG(R2[p])  ;distance traveled by Te x-ray
  M = 2*R3[p] - 1;cosine of angle of Te x-ray
  A1 = z + yTe*M          ;attenuation depth of Te x-ray along z-axis
IF (A1 LE0) THENkback += 1ELSE $
IF (A1 GE L) THENkforward += 1 $
ELSEBEGIN
             Rcoord1 = yTe * SQRT(1-M^2) ;distance Te x-ray traveled
                                         ;perpendicular to z-axis
              Xcoord1 = b * Rcoord1 * COS(360*R4[p])
              Ycoord1 = b * Rcoord1 * SIN(360*R4[p])
ENDELSE
ENDIF
;end of CdTe process

IF (A1 GE0) AND (A1 LT L) THENBEGIN
yCd = -tCd*ALOG(R5[p])   ;distance traveled by Cd x-ray
 M2 = 2*R6[p] - 1;cosine of angle of Cd x-ray
 A2 = z + yTe*M + yCd*M2  ;attenuation depth of Cd x-ray along z-axis
```

```
IF (A2 LE0) THENkback += 1ELSE $
IF (A2 GE L) THENkforward += 1 $
ELSEBEGIN
kabsorbed += 1
Lk = b*ROUND(A2)
       K[Lk] = K[Lk] + 1;pixel of full absorption along z-axis
       Rcoord2 = yCd * SQRT(1-M2^2)  ;distance Cd x-ray traveled
                                     ;perpendicular to z-axis
          Xcoord2 = Xcoord1 + b * Rcoord2 * COS(360*R7[p])
          Ycoord2 = Ycoord1 + b * Rcoord2 * SIN(360*R7[p])
          u = 425 + ROUND(Xcoord2) ;center incident beam in x-direction
          v = 425 + ROUND(Ycoord2) ;center incident beam in y-direction
          dx = -50 + 100*R8[p]     ;spread incident beam across pixel in
                                   ;x-direction
dy = -50 + 100*R9[p]     ;spread incident beam across pixel in
                                   ;y-direction
             u = u + dx
             v = v + dy
IF (u LT850) AND (v LT850) AND $
               (u GE0) AND (v GE0) THEN $
                  S[u,v] += 1ELSE $
kside += 1;side escape
ENDELSE
ENDIF
ENDELSE
    p += 1
ENDWHILE
counters = [transmitted, kback, kforward, kabsorbed, kside]
print, '    transmitted    kbackkforwardkabsorbedkside'
print,counters
print,total(S)

openw,unit,'C:\Documents and Settings\Shannon Fritz\Desktop\MonteCarlo_IDL\counters1mm.txt',/GET_LUN
printf,unit,'transmitted','kback','kforward','kabsorbed','kside', counters,FORMAT = '(5A15/,5I8)'
openw,unit,'C:\Documents and Settings\Shannon Fritz\Desktop\MonteCarlo_IDL\G1mm.txt',/GET_LUN
printf,unit,G, FORMAT = '(I)'
openw,unit,'C:\Documents and Settings\ShannonFritz\Desktop\MonteCarlo_IDL\K1mm.txt',/GET_LUN
printf,unit,K, FORMAT = '(I)'
close,/all

;check to make sure all incident photons and char x-rays have been counted
```

```
IF (kabsorbed-kside) EQtotal(S) AND (N EQtransmitted+kabsorbed+kback+kforward)$
THENprint, 'All photons accounted for' $
ELSEprint, 'Some photons are missing!!!'

;dispaly depth profile of interactions
!P.MULTI = [0,1,2]
Plot, G
Plot, K
WINDOW,1, xpos=0,ypos=0, XSIZE=850, YSIZE=850, TITLE='pixel'
tvscl, S,0
WRITE_TIFF,'C:\Documents and Settings\Shannon Fritz\Desktop\MonteCarlo_IDL\S1mm.tif', S,/LONG

END
```

Output images:

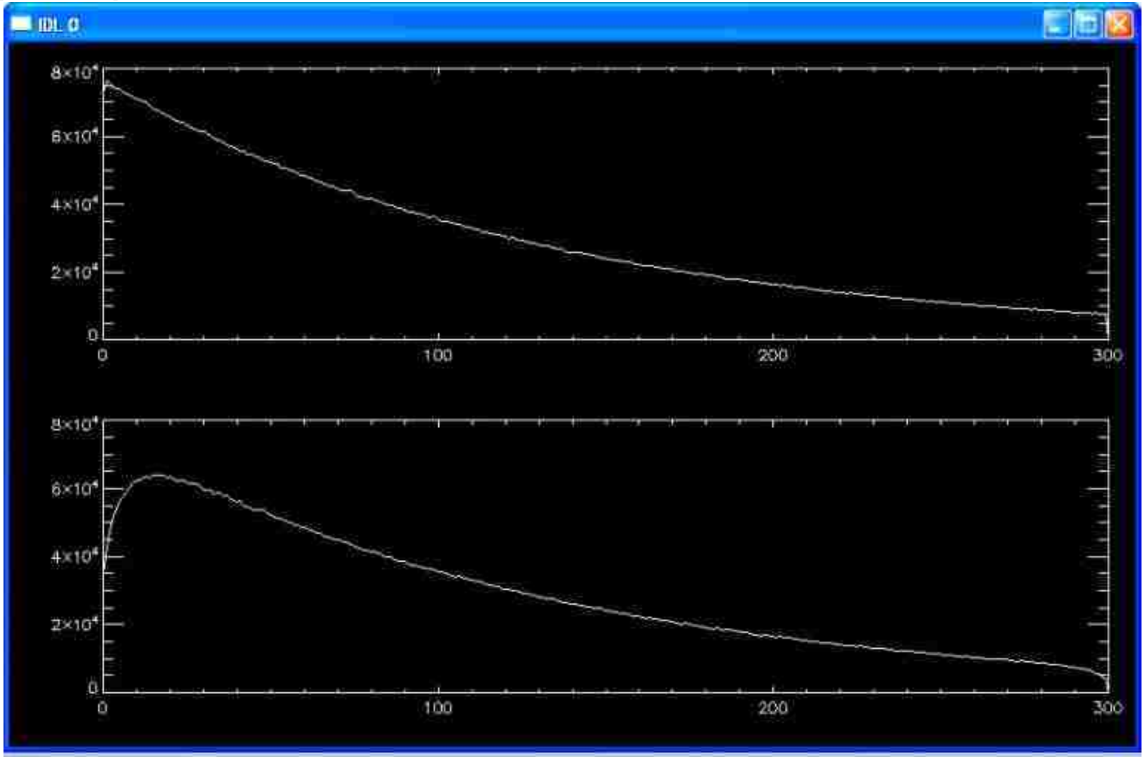

Figure B.1 Depth attenuation profiles for initial interaction of incident photon (G), top, and final interaction depth of characteristic x-ray (K), bottom. Note that due to back escape, counts at shallow depth in profile K are decreased compared to G.

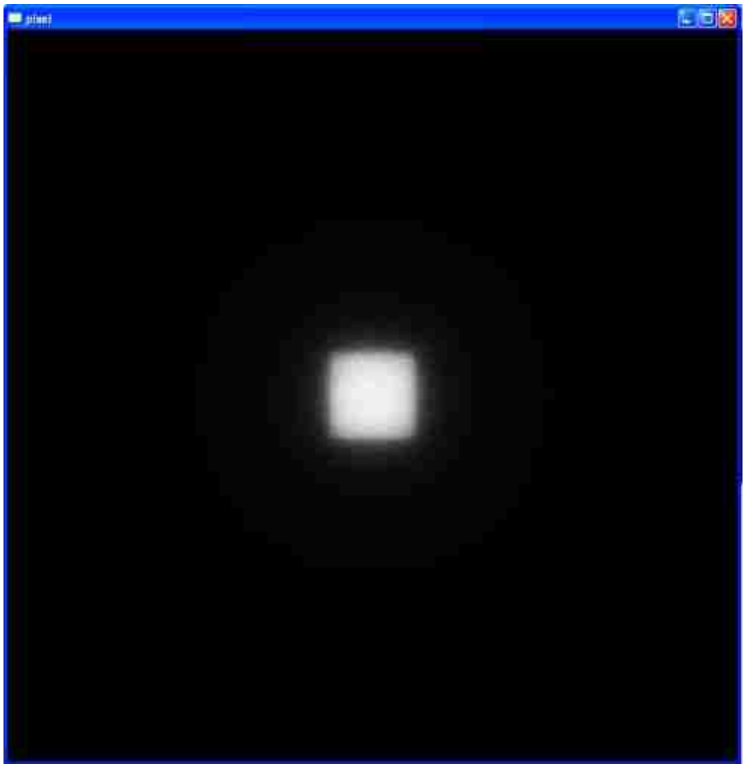

Figure B.2 Image of intensity of final characteristic x-ray absorption position when beam is uniform over a square pixel.

APPENDIX C K BACK ESCAPE FRACTIONS AND CORRECTION OF X-RAY SPECTRUM

The following codes were written using Interactive Data Language (IDL). There are four codes total. The first creates tables of back escape fractions for Cd and Te separately. Following this are two codes that call up 1) attenuation lengths and 2) relative interaction probabilities for Cd and Te that are retrieved by the first code. The last code corrects input x-ray spectra for characteristic x-ray escape.

```
PROPhotoElectricBackscatter, Eo
N = 10E5
start = SYSTIME(1)
AngArray = [90,30]
stepsize = 1.0
Nenergy = (120-27)/stepsize + 1
EnergyArray = DBLARR(Nenergy)
primary = DBLARR(Nenergy)
primary[*] = N
L = 3000.

FOR i=0,Nenergy-1DOBEGIN
Eo = 27 + i*stepsize
EnergyArray[i] = Eo
ENDFOR

FOR b = 0,1DOBEGIN
angle = AngArray[b]
  alpha = angle * !PI / 180
transmitted = DBLARR(Nenergy)
KBackCd = DBLARR(Nenergy)
KBackTe = DBLARR(Nenergy)
KAbsorbed = DBLARR(Nenergy)

FOR j = 0,Nenergy-1DOBEGIN
Eo = EnergyArray[j]
CZTatttablebackscatter, data, Eo, t1 ;retrieve linear attenuation
                                     ;coefficient in CZT for  Eo
CdandCdTeRatios, Te, Eo;retrieve probability of intitialTe interactions
                         ;vs. initial Cd interaction for Eo
tTe = 64.
tCd = 116.

R1 = RANDOMU(seed,N)   ;sample interaction length of incoming photon
```

```
RTeCd = RANDOMU(seed,N);sample probability of inititial interaction with Te
R2 = RANDOMU(seed,N)   ;sample interaction length of Te K x-ray
R3 = RANDOMU(seed,N)   ;sample cosine of Te K x-ray
R4 = RANDOMU(seed,N)       ;sample azimuthal angle of Te K x-ray
R5 = RANDOMU(seed,N)       ;sample interaction length of Cd K x-ray
R6 = RANDOMU(seed,N)       ;sample cosine of Cd K x-ray
R7 = RANDOMU(seed,N)       ;sample aziumthal angle of Cd K x-ray

p = 0.
WHILE p LT N DOBEGIN
z = -t1*sin(alpha)*ALOG(R1[p])  ;interaction position of incident photon
IF z GE L THEN transmitted[j] += 1 $
ELSEBEGIN
yTe = 0.
        M = 0.
        A1 = 0.
IFRTeCd[p] LETeTHENBEGIN
yTe = -tTe*ALOG(R2[p]);distance traveled by Te x-ray
           M = 2*R3[p] - 1;cosine of angle of Te x-ray
           A1 = z + yTe*M      ;attenuation depth of Te x-ray along z-axis
IF A1 LT0THENKBackTe[j] += 1
ENDIF
IF A1 GE0THENBEGIN
yCd = -tCd*ALOG(R5[p])     ;distance traveled by Cd x-ray
        M2 = 2*R6[p] - 1;cosine of angle of Cd x-ray
        A2 = z + yTe*M + yCd*M2;attenuation depth of Cd x-ray along z-axis
IF A2 LE0THENKBackCd[j] += 1ELSEKAbsorbed[j] += 1
ENDIF
ENDELSE;end z condition - transmission
  p += 1
ENDWHILE
ENDFOR
;save escape fractions
angstring = string(angle,FORMAT='(I4)')
stepstring = string(stepsize,FORMAT='(4F0/)')
stepstring = STRMID(stepstring, 0, 4)
openw,unit,'C:\Documents and Settings\Shannon Fritz\Desktop\MonteCarlo_IDL\backscatter\'+angstring+'deg '+stepstring+'keV steps.txt',/GET_LUN
printf, unit,'Energy', 'Primary', 'Trans', 'KBackCd', 'KBackTe', 'KAbsorbed', $
TRANSPOSE([[EnergyArray], [primary], [transmitted], [KBackCd], [KBackTe], [KAbsorbed]]), FORMAT = '(6A18/,6F/,6F/,6F/,6F/,6F/,6F)'
close,/all
print,'done with angle',angle
```

```

ENDFOR
  stop = SYSTIME(1)
print, 'Time for computation is ', (stop - start)/60, ' minutes.'
END
```

The next code retrieves a text file of linear attenuation lengths (µm) of photons for CZT obtained from the inverse of linear attenuation coefficients taken from NIST data. The text file has two columns; the first column is energy values in 1 keV steps and the second is the corresponding attenuation length.

```
PROCZTattTablebackscatter, data, Eo, t1

 file = 'C:\Documents and Settings\Shannon Fritz\Desktop\MonteCarlo_IDL\backscatter\CZT attcoeff backscatter.txt'
OPENR, lun, file, /GET_LUN
   e = 0.0;photon energy (keV)
   t = 0.0;total attenuation length (um)
   rows = file_lines(file)
   data = FLTARR(rows,2)
FOR i = 0, rows-1DOBEGIN
READF, lun, e,t
   data[i,0] = e
   data[i,1] = t
ENDFOR
FREE_LUN,lun
   data = TRANSPOSE(data)
     i = 0
WHILEEoGT data[0,i] DOBEGIN
      i += 1
ENDWHILE
Eo = data[0,i]
t1 = data[1,i]

END
```

The next code retrieves a text file of relative probabilities of initial interaction of the primary photon with Cd or Te. The text file has three columns; the first column is energy values with step size 1 keV and the second and third are the corresponding probabilities of Cd and Te interactions, respectively. For a given row the sum of the second and third columns is one.

```
PROCdandCdTeRatios, Te, Eo

```

```
file = 'C:\Documents and Settings\Shannon
Fritz\Desktop\MonteCarlo_IDL\backscatter\ratio Cd and CdTe for
backscatter.txt'
OPENR, lun, file, /GET_LUN
   energy = 0.0
   Cd = 0.0
Te = 0.0
   rows = file_lines(file)
   data = FLTARR(rows,3)
FOR i = 0, rows-1DOBEGIN
READF, lun, energy, Cd, Te
   data[i,0] = energy
   data[i,1] = Cd
   data[i,2] = Te
ENDFOR
FREE_LUN,lun
   data = TRANSPOSE(data)
   i = 0
WHILEEoGT data[0,i] DOBEGIN
      i += 1
ENDWHILE
Te = data[2,i]  ;probability of initial Te interaction

END
```

The following code was written to correct measured x-ray spectra for back escape of characteristic x-rays from the front surface of a CZT detector. If the detector dimensions are such that other escapes types are negligible, i.e. forward and side escape, this code can be used to accurately correct for characteristic x-ray escape.

```
PROKescapeCorrections2

angle = ''
read, 'Enter angle:', angle

detector = ''
read, 'Enter detector (capgrid or planar):', detector

filter = ''
read, 'Enter filter', filter ;filter used in x-ray measurement (acrylic)

stepsize = '1.0'
;retrieve measured x-ray spectrum
measuredresults = 'C:\Documents and Settings\Shannon
Fritz\Desktop\MonteCarlo_IDL\backscatter\corrections\x-ray\'+detector+'
```

```
CZT '+angle+' deg '+stepsize+'keV steps '+filter+' filter.txt'
OPENR, lun, measuredresults, /GET_LUN
   energy = 0.0;photon  energy (keV)
   counts = 0.0;measured counts for ___kVp,
   rows = file_lines(measuredresults)
   data = FLTARR(rows,6)
FOR i = 0, rows-1DOBEGIN
READF, lun, energy, one, two, three, four, five
   data[i,0] = energy
   data[i,1] = one
   data[i,2] = two
   data[i,3] = three
   data[i,4] = four
   data[i,5] = five
ENDFOR
FREE_LUN,lun
   data = TRANSPOSE(data)
;retrieve back escape fractions for correct incidence angle
escapefractions = 'C:\Documents and Settings\Shannon Fritz\Desktop\MonteCarlo_IDL\backscatter\corrections\x-ray\escape fractions '+angle+' deg '+stepsize+'keV steps A.txt'
OPENR, lun, escapefractions, /GET_LUN
   energy = 0.0
   Cd = 0.0
Te = 0.0
   rows = file_lines(escapefractions)
frData = FLTARR(rows,3)
FOR i = 0, rows-1DOBEGIN
READF, lun, energy, Cd, Te
frData[i,0] = energy
frData[i,1] = Cd
frData[i,2] = Te
ENDFOR
FREE_LUN,lun
frData = TRANSPOSE(frData)

Emax = 120
p = 1.
WHILE p LT6DOBEGIN
kVp = p

ARRAY = FLTARR(8,rows)
ARRAY = [data[0,*],data[kVp,*],data[kVp,*],frData[1,*],frData[2,*],frData[1,*],frData[2,*]]
```

```
j = rows-1
E = ARRAY(0,j)

WHILE j GT0DOBEGIN

ARRAY(2,j) = ARRAY(2,j)/(1 - ARRAY(5,j) - ARRAY(6,j)) ;This is Ntrue(Eo) = Nmeas(Eo) / (1 - fCd(Eo) - fTe(Eo))
ARRAY(5,j) = ARRAY(2,j)*ARRAY(3,j) ;This is NCd(Eo) = fCd(Eo) * Ntrue(Eo)
ARRAY(6,j) = ARRAY(2,j)*ARRAY(4,j) ;This is NTe(Eo) = fTe(Eo) * Ntrue(Eo)


k = j - 23/stepsize;ECd = Eo - 23
l = j - 27/stepsize;ETe = Eo - 27

IF l GE0THEN ARRAY(2,l) = ARRAY(2,l) - ARRAY(6,j) ;This is Nadj(El) = Nmeas(El) - NTe(Eo), now this value will be used to find Ntrue
IF k GE0THEN ARRAY(2,k) = ARRAY(2,k) - ARRAY(5,j) ;This is Nadj(El) = Nmeas(El) - NCd(Eo), now this value will be used to find Ntrue

j = j - 1
E = ARRAY(0,j)
ENDWHILE
Energy = string(Emax,FORMAT='(I4)')
openw,unit,'C:\Documents and Settings\Shannon Fritz\Desktop\MonteCarlo_IDL\backscatter\corrections\'+detector+' CZT '+Energy+'kVp '+angle+' deg '+stepsize+'keV steps '+filter+' filter.txt',/GET_LUN
printf, unit,'Energy', 'Nmeasured', 'Ncorrected', 'frCd', 'frTe','NCd', 'NTe', ARRAY, FORMAT = '((7A18/,7F/,7F/,7F/,7F/,7F/,7F))'
close,/all

Emax = Emax - 20
p += 1
ENDWHILE
print,'done!'
END
```

VITA

Shannon Gail Fritz was born in San Antonio, Texas, the eldest of three girls. She graduated from East Central High School, in the school district that includes the community of China Grove, the subject of the great song of the same name recorded by the Doobie Brothers. She began her undergraduate career at Texas Lutheran University in Seguin, Texas, as an elementary education major, then subsequently changed majors to English, then Spanish and history, and was undecided for a semester until she finally settled on physics.

After earning her bachelor of arts in physics, Shannon went on to get a master's degree at Texas State University in San Marcos, Texas. She then moved to Lincoln, Nebraska, and began graduate research at the University of Nebraska. While there she became interested in medical physics and applied to the program at Louisiana State University so that she could earn her doctorate, specializing in medical physics. She married her climbing partner, Mark Stigge, and they left their winter coats behind and moved down South.

Shannon believes that she now has enough physics degrees and after graduation would like to begin a residency or junior physicist position.